

ABSTRACT

Title of dissertation: MEASUREMENT OF Z BOSON TRANSVERSE MOMENTUM
IN PROTON-ANTIPROTON
COLLISIONS AT $\sqrt{s}=1.96$ TeV

Lei Wang, Doctor of Philosophy, 2007

Dissertation directed by: Professor Sarah C. Eno
Department of Physics

This dissertation describes a measurement of the shape of the boson transverse momentum distribution in $p\bar{p} \rightarrow Z/\gamma^* \rightarrow e^+e^- + X$ events at a center-of-mass energy of 1.96 TeV. The measurement is made for events with electron-positron mass between $70 < M_{ee} < 110$ GeV/ c^2 and uses 976 pb^{-1} of data collected at the Fermilab Tevatron collider with the DØ detector. The shape is measured both for the inclusive sample and for the subset of events containing a boson with large rapidity. The large-rapidity distribution shows better agreement with theory when the calculation is done using traditional Collins-Soper-Sterman resummation than when using a recent resummed form factor with modifications in the small- x region.

Measurement of Z Boson Transverse Momentum
in Proton-Antiproton Collisions at $\sqrt{s}=1.96$ TeV

by

Lei Wang

Dissertation submitted to the Faculty of the Graduate School of the
University of Maryland, College Park in partial fulfillment
of the requirements for the degree of
Doctor of Philosophy
2007

Advisory Committee:

Professor Sarah C. Eno, Chair/Advisor
Professor Nicholas J. Hadley
Professor Xiangdong Ji
Associate Professor Douglas A. Roberts
Professor Alice C. Mignerey

© Copyright by
Lei Wang
2007

To my parents, sister and Zheng

ACKNOWLEDGMENTS

Finally the journey is about to come to an end. Looking back through the past five years, I am thankful to all the people helped me along the journey. Without their help, to complete the PhD study is a mission impossible.

First of all, I want to thank my thesis advisor Sarah Eno. I am very fortunate to be her student. Her bright insight of problems, vast knowledge on experimental physics always impressed me. She is a very considerate advisor and always cares about me. She is always willing to spend time to discuss with me about my research progress although various responsibilities have taken a lot of her time. I also can not forget all her support and encouragement that give me strength and confidence. How can I ask for a better advisor!

I had a such good experience with all the people in the Maryland DØ group. Professor Nick Hadley is always willing to explain complicated ideas in simple and understandable words to me. To talk with him is always a pleasure. Professor Drew Baden taught me how to drive a manual transmission car at CERN. Marco Verzocchi helped me a lot by providing data samples and example codes when I got started at DØ . I also learned a lot from discussion with him. Terry Toole is very helpful when I had computer related questions. I also benefited a lot from discussion with him to clarify my questions about event generators. Junjie Zhu was from the same college as mine in China and we had a lot of conversation topics together. But he helped me so much on my research and I always enjoy discussing with him. Michiel Sanders shared an office together with me for one year, I learned a lot from him. Ming Yan was my roommate for one year. How can I forget him picking me up on the road when my 1995 Ford Taurus broke down in the snowy Chicago winter and fixing the car for me the same day! There are also Matt Wetstein and Chad Jarvis, the two nice guys I always like to talk with.

I also want to thank all the WZ group people, EMID group people and simulation group people.

Especial thanks to Dmitri Denisov, Ia Iashvili, Tim Bolton, Jan Stark, Thomas Nunnemann, Heidi Schellman, Jon Hays, Christian Schwanenberger, Ashish Kumar, Laurent Duflot, Ursula Bassler, Michael Hildreth for their constant help and great collaboration.

During the five years in Maryland, I also met many good friends. With their friendship, I can enjoy the life at a place far away from my home country. There are too many of them and I can only name a few: Su Li, Fangzhen Teng, Ji Luo, Luyan Sun, Hui Wang, Liu Yang, Limin Fu, Yue Wang, Yingkai Liu, Juchen Guo, Zhong Jin, Zhe Lin, Yun Liu, Jianlin Wu, Sheng Li, Jin Qin, Yingchuan Li, Yao Wu, Hua Xu. However I left Maryland, we will be friends forever.

My parents Yutian Wang and Fenglan Sun are the source of spirit for my pursuit of a career in fundamental science. They are now retired and enjoying their life in my hometown. I have always regretted not being able to visit them much during the past five years due to visa concerns. My elder sister Chen Wang is so considerate and she is the best sister I can ask for. I am so grateful for their unconditional love and support.

I am so fortunate to meet my wife Zheng in Maryland. Her love, support and care carried me along this journey. No words can express my thanks to her. I am the luckiest man in the world!

TABLE OF CONTENTS

List of Tables	viii
List of Figures	ix
1 Introduction	1
1.1 Introduction	1
1.2 The Standard Model	2
1.3 Z Boson production in $p\bar{p}$ collisions	4
1.4 Motivation for the Measurement of the Z Boson Transverse Momentum	9
2 Fermilab Accelerator and DØ Detector	11
2.1 The Accelerator	11
2.2 DØ Detector	13
2.2.1 The DØ Coordinate System	14
2.2.2 Tracking System	15
2.2.3 Preshower Detectors	17
2.2.4 Calorimeters	19
2.2.5 Muon System	24
2.3 Luminosity System	25
2.4 Trigger System	27
3 Event Selection	30
3.1 Data Set	30
3.2 Track and Vertex Reconstruction	32
3.3 Electron Identification	33
3.4 Offline Selection Criteria	35

4	Single Electron Efficiencies	39
4.1	Preselection Efficiency	40
4.2	Spatial Track Matching Efficiency	42
4.3	Trigger Efficiency	45
4.4	H-Matrix Efficiency	46
5	Monte Carlo Simulation	53
5.1	Physics Generator	54
5.2	Parameterized Monte Carlo Simulation	54
5.2.1	Energy Scale	54
5.2.2	Energy Resolution	55
5.2.3	Position Resolutions	61
5.2.4	Vertex Distribution	61
5.2.5	Parameters	62
5.3	Comparison between Data and Monte Carlo	62
6	Backgrounds	73
6.1	QCD Backgrounds	73
6.2	Non QCD Backgrounds	76
6.2.1	$Z \rightarrow \tau^+\tau^-$	76
6.2.2	Di-boson backgrounds	76
7	Efficiency×Acceptance Correction	78
7.1	Efficiency and Acceptance	78
7.2	Dependence of the selection efficiency on the boson p_T	78
7.3	Dependence of the geometric and kinematic acceptance on the boson p_T	82
7.4	p_T dependent Efficiency×Acceptance	83
8	Results	86
8.1	Unfolding the Detector Smearing	86

8.2	The Program RUN	86
8.3	Setup of the Unfolding Program	87
8.4	Test of the Unfolding Program	88
8.5	Unfolded Result	89
8.6	Systematic Uncertainties	89
8.6.1	Uncertainties from the smearing parameters during unfolding	90
8.6.2	Uncertainties from the 40 PDFs	92
8.6.3	Uncertainties from the unfolding program	93
8.6.4	Uncertainties from the Efficiency \times Acceptance p_T dependence	94
8.6.5	Uncertainties from the QCD background	95
8.7	Z p_T Distribution For Low p_T Region	95
8.8	Tuning of ResBos g_2 parameter	96
8.9	Z p_T Distribution For All p_T Regions	96
9	Result of Z bosons with rapidity greater than 2.0	106
10	Closure tests	111
10.1	Full Monte Carlo Test For All y Region	111
10.2	Full Monte Carlo Test For Z s with $y > 2$	111
10.3	Test For Z s with $0.5 < y < 2$	112
11	Conclusions	121
	Bibliography	122

LIST OF TABLES

1.1	Fundamental forces and force carriers of the Standard Model.	4
2.1	Central Calorimeter Module Parameters.	25
2.2	End Calorimeter Module Parameters. IFH, ICH, MFH, MCH, OH stand for inner fine hadronic, inner coarse hadronic, middle fine hadronic, middle coarse hadronic and outer hadronic section respectively. UNb and SS stand for Uranium-Niobium alloy and Stainless Steel.	26
3.1	Results of event selection	36
4.1	Results of event selection for preselection efficiency measurement	42
4.2	Trigger efficiency for different trigger lists	49
5.1	Parameters tuned according to data	63
6.1	Background fractions for events in different calorimeter regions.	75
6.2	Expected number of events for 1 fb ⁻¹ data.	77
8.1	Normalized differential cross section $\frac{1}{\sigma} \frac{d\sigma}{dp_T}$	104
8.2	Error correlation matrix	105

LIST OF FIGURES

1.1	Elementary particles. The lepton and quark families are shown as well as the force-carrying bosons. The mass of the particles increases with generation number (with the possible exception of neutrinos).	5
1.2	Lowest-order Feynman diagram for Z boson production in hadronic collisions. . . .	6
1.3	Initial state gluon radiation and Compton scattering in Z production.	8
1.4	Theoretical predictions for the Z p_T spectrum at Tevatron Run II. The solid lines represent p_T spectrum calculated without small- x correction. The dashed lines represent those with the small- x correction.	10
2.1	The general layout of the collider facility at Fermilab.	12
2.2	Tevatron bunch scheme for Run I (top) and Run II (bottom).	13
2.3	A view of the DØ Run II upgraded detector.	16
2.4	Cross-sectional view of the DØ tracking volume.	17
2.5	DØ Run II Silicon Microstrip Tracker detector.	18
2.6	(a) A quarter $r - z$ view of the CFT detector showing the nested eight barrel design. (b) A magnified $r - \phi$ end view of the two doublet layer configuration for two different barrels.	19
2.7	Cross-sectional end view (left) and side view (right) of the Central Preshower Detector.	20
2.8	One quarter view of the Forward Preshower Detector.	21
2.9	Overall view of the calorimeter system.	22
2.10	Side-view of one quarter of the DØ calorimeter system, showing segmentation and tower definitions. The line extending from the center of the detector denote the pseudo-rapidity coverage of cells and projected towers.	23
2.11	Schematic view of a representative calorimeter unit cell. The gap structure, grounded absorber plates, and signal boards are shown.	24
2.12	Exploded view of the muon wire chambers	27

2.13	Exploded view of the muon scintillation detectors	28
2.14	Summary of the three-level DØ trigger system for Run II with the decision time and bandwidth allocated to each level.	29
3.1	Integrated luminosity delivered by the Tevatron Collider and recorded by the DØ detector (pb^{-1}).	31
3.2	Invariant mass distribution of $Z/\gamma^* \rightarrow e^+e^-$ candidates.	37
3.3	p_T distribution of $Z/\gamma^* \rightarrow e^+e^-$ candidates.	38
4.1	Preselection efficiency vs electron detector eta.	43
4.2	Preselection efficiency vs electron detector eta.	44
4.3	Preselection efficiency vs electron detector eta.	45
4.4	Preselection efficiency vs electron detector eta.	46
4.5	Spatial Track Matching efficiency vs CC electron η_{det}	47
4.6	Spatial Track Matching efficiency vs EC electron η_{det}	48
4.7	Spatial Track Matching efficiency vs CC electron p_T	48
4.8	Spatial Track Matching efficiency vs EC electron p_T	49
4.9	Trigger efficiency vs electron p_T	50
4.10	Trigger efficiency vs electron η_{det}	51
4.11	H-matrix efficiency as a function of detector η , detector ϕ , phimod, p_T of CC electron	52
4.12	H-matrix efficiency as a function of detector η , detector ϕ , phimod, p_T of EC electron	52
5.1	Tuning of energy scale and offset for negative endcap region. The top left plot is the invmass peak for data sample, the top right plot is the invmass peak for Monte Carlo sample. The bottom two plots are the tuning of energy offset and scale, respectively.	56
5.2	Sampling term η_{phys} dependence for central calorimeter.	58
5.3	p_0 dependence for central calorimeter.	59
5.4	p_1 dependence for central calorimeter.	59

5.5	Detector setup in the GEANT simulation of the Endcap Calorimeter and the materials in front of it.	60
5.6	Radiation length of the materials in front of the Endcap Calorimeter as a function of η_{phys} . The big error bars between -1.5 and -2.5 of η shows big materials (the Forward Preshower Detector) variations in the ϕ direction.	64
5.7	Sampling term η_{phys} dependence for positive endcap calorimeter.	65
5.8	Sampling term η_{phys} dependence for negative endcap calorimeter.	65
5.9	η_{phys} dependence of s0 for positive endcap calorimeter.	66
5.10	η_{phys} dependence of s0 for negative endcap calorimeter.	66
5.11	η_{phys} dependence of s1 for positive endcap calorimeter.	67
5.12	η_{phys} dependence of s1 for negative endcap calorimeter.	67
5.13	The energy flow in a 1×5 slice in η - ϕ tower space as a function of the ϕ separation from the electron cluster centroid	68
5.14	Average energy per EM tower for CC electrons from $W^- \rightarrow e\nu$ studies	68
5.15	Vertex z distribution of the $Z/\gamma^* \rightarrow e^+e^-$ events.	69
5.16	Invariant mass distribution for data and Monte Carlo of $Z/\gamma^* \rightarrow e^+e^-$ events . . .	69
5.17	Invariant mass distribution for data and Monte Carlo of $Z/\gamma^* \rightarrow e^+e^-$ events . . .	70
5.18	Electron p_T distribution for CC-CC, CC-EC, EC-EC, All data and Monte Carlo Z/γ^* events	70
5.19	Electron η_{det} distribution for CC-CC, CC-EC, EC-EC, All data and Monte Carlo Z/γ^* events	71
5.20	Electron ϕ_{det} distribution for CC-CC, CC-EC, EC-EC, All data and Monte Carlo Z/γ^* events	71
5.21	Rapidity distribution for CC-CC, CC-EC, EC-EC, All data and Monte Carlo Z/γ^* events	72
6.1	Invariant mass distribution for the QCD background di-jet sample and EM+jet sample	74
6.2	p_T distribution for the QCD background di-jet sample and EM + jet sample . . .	74

6.3	Invariant mass distribution for the QCD background	76
6.4	p_T distribution for the QCD background	77
7.1	Profile of electron isolation, H-matrix(7)(CC), H-matrix(8)(EC) and spatial track match χ^2 probability as a function of Z p_T	80
7.2	Efficiency as function of Z boson p_T for PYTHIA and re-weighted Monte Carlo sample	81
7.3	Efficiency as function of Z boson p_T for different Z rapidity bins	82
7.4	Overall efficiency as a function of Z boson p_T	83
7.5	Revised efficiency as function of Z boson p_T for data and full Monte Carlo	84
7.6	Shown here are the acceptances as a function of Z boson p_T	84
7.7	Fractional uncertainty on the acceptances due to the smearing parameters as a function of Z boson p_T	85
7.8	Efficiency*acceptance as a function of Z boson p_T	85
8.1	Comparison between the generated Z boson p_T spectrum for different values of g_2 for ResBos.	88
8.2	Comparison between the unfolded and generated Z boson p_T for the test.	89
8.3	Cross section normalized unfolded Z boson p_T distribution. The error shown in this plot is statistical error only.	90
8.4	Fractional systematic uncertainty on Z boson p_T distribution due to the energy scales.	92
8.5	Fractional systematic uncertainty on Z boson p_T distribution due to the energy offsets.	93
8.6	Fractional systematic uncertainty on unfolded Z boson p_T distribution due to the constant terms.	94
8.7	Fractional systematic uncertainty on Z boson p_T distribution due to the sampling terms.	95

8.8	Fractional systematic uncertainty on Z boson p_T distribution due to all the smearing parameters.	96
8.9	Fractional systematic uncertainty on Z boson p_T distribution due to the CTEQ6.1m PDFs.	97
8.10	Fractional systematic uncertainty on Z boson p_T distribution due to the input MC of the unfold program.	98
8.11	Fractional systematic uncertainty on Z boson p_T distribution due to the parameter “KNOTS” of the unfold program.	99
8.12	Fractional systematic uncertainty on Z boson p_T distribution due to the QCD background.	100
8.13	Fractional systematic uncertainty on Z boson p_T distribution due to different sources.	100
8.14	Unfolded Z boson p_T distribution. The error contains both statistical and systematic uncertainties.	101
8.15	Tuning of ResBos g_2 parameter using unfolded Z p_T spectrum.	101
8.16	Event display for highest Z p_T event. This is the XY view.	102
8.17	Unfolded Z boson p_T distribution. The error contains both statistical and systematic uncertainties.	103
9.1	p_T distribution for Z candidates with $ y > 2$	106
9.2	Invariant mass distribution for Z candidates with $ y > 2$	107
9.3	Efficiency(Z p_T) distribution for Z candidates with $ y > 2$	108
9.4	Acceptance(Z p_T) distribution for Z candidates with $ y > 2$	108
9.5	Efficiency*Acceptance(Z p_T) distribution for Z candidates with $ y > 2$	109
9.6	Unfolded Z p_T distribution for Z candidates with $ y > 2$. The errors are statistical errors only.	109
9.7	Unfolded Z p_T distribution for Z candidates with $ y > 2$	110
9.8	Comparison of unfolded Z p_T distributions for Z candidates with $ y > 2$ and all y .	110

10.1	Acceptance $Z p_T$ dependence for the full Monte Carlo $Z/\gamma^* \rightarrow e^+e^-$ sample . . .	112
10.2	Efficiency*Acceptance $Z p_T$ dependence for the full Monte Carlo $Z/\gamma^* \rightarrow e^+e^-$ sample	113
10.3	Comparison of invariant mass distribution for the full Monte Carlo $Z/\gamma^* \rightarrow e^+e^-$ sample, linear scale	114
10.4	Comparison of invariant mass distribution for the full Monte Carlo $Z/\gamma^* \rightarrow e^+e^-$ sample, log scale	114
10.5	Comparison of the $Z p_T$ distributions for the unfold data and the PYTHIA generator in the full Monte Carlo closure test	115
10.6	Difference between the $Z p_T$ distributions for the unfold data and the PYTHIA generator in the full Monte Carlo closure test	116
10.7	Efficiency $Z p_T$ dependence for the full Monte Carlo $Z/\gamma^* \rightarrow e^+e^- y > 2$ sample.	116
10.8	Acceptance $Z p_T$ dependence for the full Monte Carlo $Z/\gamma^* \rightarrow e^+e^- y > 2$ sample.	117
10.9	Efficiency×Acceptance $Z p_T$ dependence for the full Monte Carlo $Z/\gamma^* \rightarrow e^+e^- y > 2$ sample.	117
10.10	Comparison of the $Z p_T$ distributions for the unfold data and the PYTHIA generator in the full Monte Carlo $ y > 2$ closure test.	118
10.11	Efficiency $Z p_T$ dependence for the $Z/\gamma^* \rightarrow e^+e^- 0.5 < y < 2$ sample.	118
10.12	Acceptance $Z p_T$ dependence for the $Z/\gamma^* \rightarrow e^+e^- 0.5 < y < 2$ sample.	119
10.13	Efficiency×Acceptance $Z p_T$ dependence for the $Z/\gamma^* \rightarrow e^+e^- 0.5 < y < 2$ sample.	119
10.14	Raw $Z p_T$ distribution for CC-CC, CC-EC $0.5 < y < 2$ sample.	120
10.15	Unfolded $Z p_T$ distribution for CC-CC, CC-EC $0.5 < y < 2$ sample.	120

Chapter 1

Introduction

1.1 Introduction

Calculations of experimental observables influenced by Quantum Chromodynamics (QCD) have always been difficult due to the large value of the strong coupling constant, α_s . The resummation technique developed by Collins, Soper, and Sterman (CSS)[1] allows the inclusion of contributions from large logarithms of the form $\ln^n(p_T/Q)$ (where p_T is the component of the momentum of the produced system transverse to the beam axis and Q is the four-momentum transferred) arising from unsuppressed soft and collinear radiation, to all orders of perturbation theory. Recent studies of data from deep inelastic scattering (DIS) experiments[2] [3] indicate that the resummed form factor may need to be modified for processes involving a small-Bjorken- x parton in the initial state. In [4], the authors discuss how such a modification would influence the p_T distributions of vector and Higgs bosons produced in hadronic collisions. A precision measurement of the mass of the W boson is one of the most sensitive indirect measures of the Higgs mass, and the p_T distribution of W bosons is an important systematic uncertainty in this measurement.

In this thesis, we present an experimental measurement of the p_T distribution of Z/γ^* bosons produced in $p\bar{p}$ collisions with a center-of-mass energy of 1.96 TeV using data taken with the D0 detector at the Tevatron Collider. At leading order in α_s , Z/γ^* bosons are produced through the annihilation of a quark and an anti-quark, with the partons in the proton and anti-proton carrying momentum fractions x_1 and x_2 , respectively. The parton momentum fractions are in turn directly related to the rapidity of the boson, defined $y = \frac{1}{2} \ln \frac{E+p_L}{E-p_L}$, where E is the energy of the boson and p_L is the component of its momentum along the beam direction, by $x_{1,2} = \frac{M_Z}{\sqrt{s}} e^{\pm y}$. Here, M_Z is the mass of the boson, and \sqrt{s} is the center of mass energy. Bosons with rapidity

between 2.0 and the kinematic limit, 3.0, thus probe processes involving a parton with Bjorken- x between 0.002 and 0.006, and can be used as a test of the resummed form factor at small x .

Regardless of the resummation technique, the results of the calculation depend on a parameterization of non-perturbative long-distance effects. We use the inclusive distribution to provide a more precise measurement of these effects following the formalism developed in [5]. The resulting parameterization can be used to reduce uncertainties in the W mass measurement. Z/γ^* p_T distributions have been published previously by the DØ [6] and CDF [7] collaborations using 100 pb^{-1} of data and thus have a much larger statistical uncertainty than this measurement. This measurement is also the first to present a distribution for forward-rapidity bosons.

This is a thesis in experimental elementary particle physics. Elementary particle physics is the study of the elementary constituents of matter and radiation, and the interactions between them. All the particles and their interactions observed to date can be described by a quantum field theory called the *Standard Model* (SM). Being a thesis in experimental physics, this document will involve the measurement of a specific physical quantity. In particular, I will describe the measurement of the transverse momentum of electron pairs produced in proton-antiproton collisions. The result of this measurement will be compared with the predictions of the Standard Model. Before describing the details of this measurement, I will first give a basic description of the Standard Model.

1.2 The Standard Model

In the standard model, all matter is composed of *quarks* and *leptons*. These are the fundamental and indivisible particles in the theory. There are six types of quarks and six types of leptons, as is shown in Fig. 1.1.

There are four types of fundamental forces in nature that govern the interactions among the fundamental particles: the gravitational, the strong, the weak and the electromagnetic interactions. These forces are transmitted by specific fields or particles (which are equivalent

concepts in relativistic quantum field theory [8]). All the fundamental forces, and the particles that transmit these forces, are summarized in Table 1.1.

The Standard Model describes the strong interaction, the weak interaction and the electromagnetic interaction. The SM is a quantum field theory that is based on the gauge symmetry $SU(3)_C \times SU(2)_L \times U(1)_Y$. This gauge group includes the symmetry group of the strong interactions ($SU(3)_C$) and the symmetry group of the electroweak interactions ($SU(2)_L \times U(1)_Y$). The symmetry group of the electromagnetic interactions ($U(1)_{em}$) appears in the SM as a subgroup of $SU(2)_L \times U(1)_Y$, and it is in this sense that the weak and electromagnetic interactions are unified.

In the 1960s, Glashow, Salam and Weinberg unified the electromagnetic and weak interactions into the electroweak theory [9] by using the concept of *spontaneous symmetry breaking* in a nonabelian gauge theory based on the symmetry group $SU(2)_L \times U(1)_Y$. The group $SU(2)_L$ describes a symmetry based on doublets in weak isospin space; the group $U(1)_Y$ describes a symmetry in weak hypercharge space. Spontaneous symmetry breaking takes place when a system that is symmetric with respect to some symmetry group goes into a vacuum state that is not symmetric. A scalar field with a non-vanishing vacuum expectation value can break the group $SU(2)_L \times U(1)_Y$ spontaneously to $U(1)_{em}$, leaving an electromagnetic force transmitted by a massless photon and a weak force transmitted by three spin-1, massive bosons, W^\pm and Z .

In the year 1983, an exciting event happened in the history of particle physics. The W and Z bosons were discovered by the UA1 and UA2 collaborations at the CERN $p\bar{p}$ collider in Geneva, Switzerland [10]. Their measured masses and other properties were close to the theoretical predictions.

The theory of the strong interaction is known as *Quantum Chromodynamics (QCD)*. In this theory, the strong force is ascribed to the exchange of gluons, the quanta of the color field responsible for the strong force. QCD is based on the $SU(3)$ symmetry group. $SU(3)$ is a symmetry representation of three-component color fields which are transmitted by eight massless gluons. The most important feature of QCD is that the interaction strength gets smaller as the

energy scale of the interaction increases. This property of QCD, called *asymptotic freedom*, means that at high energies (short distances), quarks and gluons within a hadron behave almost independently of one another.

This picture of particle physics based on the existence of quarks and leptons interacting via photons, gluons, W and Z bosons has withstood many experimental tests so far. However, the Standard Model is not perfect yet. For example, in electroweak theory, in order to have spontaneous symmetry breaking, there should exist a Higgs particle associated with the scalar field, but no such particle has yet been observed.

Force	Force Carrier	Symbol	Charge ($ e $)	Spin	Mass (GeV/c^2)
Strong	Gluon	g	0	1	0
Electromagnetic	Photon	γ	0	1	0
Weak	W-boson	W^\pm	± 1	1	80.423 ± 0.039
	Z-boson	Z^0	0	1	91.1876 ± 0.0021
Gravitational	Graviton	G	0	2	0

Table 1.1: Fundamental forces and force carriers of the Standard Model.

1.3 Z Boson production in $p\bar{p}$ collisions

In the $p\bar{p}$ collisions at the center-of-mass energy (\sqrt{s})=1.96 TeV produced at Run II of the Tevatron, Z bosons are produced predominantly through quark-antiquark annihilation. The lowest order diagrams for Z boson production is shown in Fig. 1.3.

In the parton model¹, Z s are produced in collisions of q and \bar{q} constituents within the proton and antiproton. The momenta of these constituents are assumed to be parallel to the momentum of the parent hadron, and consequently the component of the Z 's momentum transverse to the

¹The parton model was developed by Feynman and Bjorken in the late 1960s to explain data from deep inelastic scattering of electrons on nucleons. This model views nucleons are containing point-like constituents(called partons) and provides a simple framework to calculate scattering cross sections.

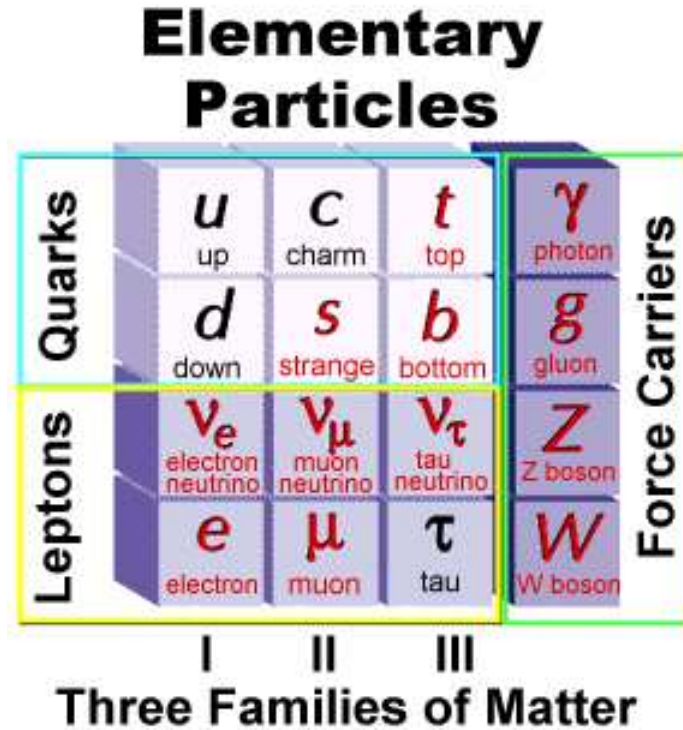


Figure 1.1: Elementary particles. The lepton and quark families are shown as well as the force-carrying bosons. The mass of the particles increases with generation number (with the possible exception of neutrinos).

beam axis (transverse momentum: p_T) must be zero. The magnitude of the transverse momentum is invariant to Lorentz boosts along the beam axis. The fact that, experimentally, Z bosons are found to have non-zero p_T must be attributed to QCD gluon radiation prior to quark-antiquark annihilation into the Z .

A useful quantity for particle physicists is the cross section, which is a measure of the likelihood of interaction between particles. The production cross section is related to the rate of particle production for any particular final state.

In the framework of QCD, the production rate of Z bosons can be calculated by multiplying the constituent cross section (the short-distance or perturbative physics) by the parton luminosities (the long-distance or non-perturbative physics). This prescription for the theoretical calculation is called the *factorization theorem* of QCD [11]. The short distance contribution can be

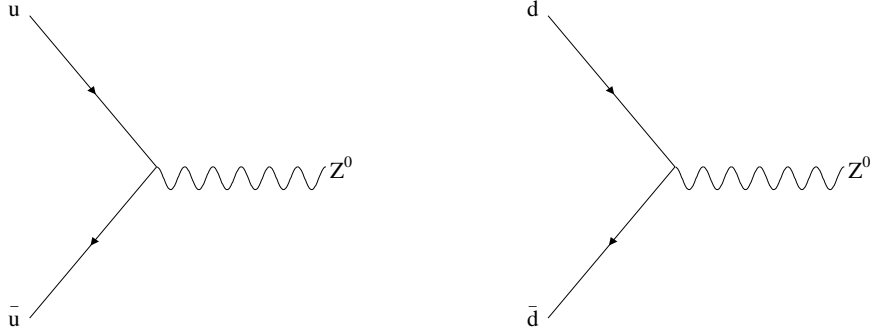


Figure 1.2: Lowest-order Feynman diagram for Z boson production in hadronic collisions.

calculated perturbatively order-by-order in the strong coupling constant α_S . The long distance part has to be parameterized and fit to experimental data.

The differential cross section for $p\bar{p} \rightarrow V + X$ (V is W or Z , X gives the rate for anything that is produced along with V) is given by:

$$\frac{d^2\sigma_V}{dp_T dy} = \sum_{i,j} \int dx_1 dx_2 f_i(x_1) f_j(x_2) \frac{d^2\sigma(ij \rightarrow V)}{dp_T dy} \quad (1.1)$$

where y is the rapidity of V ; x_1 and x_2 are the momentum fractions of the colliding partons; $f(x_1)$ and $f(x_2)$ are the *parton distribution functions*² (PDFs) for the incoming partons; $\sigma(ij \rightarrow V)$ is the partonic cross section for production of the state V . The sum is over the contributing parton flavors.

For relatively high Z boson p_T ($p_T \sim M_Z$), the production cross section can be calculated using standard perturbative methods. The leading-order Feynman diagrams are shown in Fig. 1.3. The result has the form

$$\frac{d^2\sigma_V}{dp_T dy} \sim \alpha_W \alpha_S (a_1 + a_2 \alpha_S + a_3 \alpha_S^2 + \dots) \quad (1.2)$$

²The parton distribution functions are the probability density for finding a particle with longitudinal momentum fraction x and momentum transfer Q^2

where α_W is the weak interaction strength and α_S is the strong interaction strength. This is called a *fixed-order perturbative* result. The result up to $o(\alpha_S^2)$ has been calculated by Arnold and Reno [12].

The dominant contributions to the perturbative result beyond leading order are of the form

$$\frac{d^2\sigma_V}{dp_T dy} \sim \frac{\alpha_W \alpha_S}{p_T^2} \ln\left(\frac{Q^2}{p_T^2}\right) [\nu_1 + \nu_2 \alpha_S \ln^2\left(\frac{Q^2}{p_T^2}\right) + \nu_3 \alpha_S^2 \ln^4\left(\frac{Q^2}{p_T^2}\right) + \dots] \quad (1.3)$$

where Q^2 is the square of the mass of the dilepton system (in our case, M_Z). Note that when $p_T \rightarrow 0$, this calculation diverges due to the $\frac{1}{p_T^2} \ln\left(\frac{Q^2}{p_T^2}\right)$ terms.

This problem is addressed using a technique called *resummation*, which sums the leading and the next-to-leading $\ln\left(\frac{Q^2}{p_T^2}\right)$ for each power of α_S to get an exponential factor. The Collins-Soper-Sterman (CSS) resummation formalism [1] gives the form

$$\frac{d^2\sigma_V}{dp_T^2} \sim \int d^2b e^{i\vec{p}_T \cdot \vec{b}} W(b, Q) + Y \quad (1.4)$$

where b is the impact parameter; $W(b, Q)$ sums to all orders the terms that are at least as singular as $(1/p_T^2)$ (as $p_T \rightarrow 0$); the Y term is a correction based on the fixed-order perturbative result.

The W term has the form

$$W(b, Q) \sim e^{-S(b, Q)} \quad (1.5)$$

The exponent, $S(b, Q)$, is called the *Sudakov factor*.

When p_T approaches λ_{QCD} , the perturbative techniques fail. Instead, a parameterization, that attempts to include non-perturbative effects, is used as a replacement of $W(b, Q)$,

$$W(b, Q) \rightarrow W(b_*, Q) e^{-S_{NP}(b, Q)} \quad (1.6)$$

where

$$b_* = \frac{b}{\sqrt{1 + \left(\frac{b}{b_{max}}\right)^2}} \quad (1.7)$$

is always greater than b_{max} and $S_{NP}(b, Q)$ is the non-perturbative function that controls $W(b, Q)$ for $b \gg b_{max}$.

$S_{NP}(b, Q)$ should satisfy the following requirements. When $b \rightarrow 0$ (corresponding to $p_T \rightarrow \infty$), the non-perturbative effects must decrease, so S_{NP} must $\rightarrow 0$. Large values for b ($b \rightarrow \infty$) should not contribute to the cross section, so S_{NP} should $\rightarrow \infty$ as $b \rightarrow \infty$. The value of b_{max} is usually taken to be $\sim 0.5 \text{ GeV}^{-1}$ [13].

The parameterization of S_{NP} has the following form

$$S_{NP}(b, Q) = h_1(b, x_A) + h_1(b, x_B) + h_2(b) \ln\left(\frac{Q}{2Q_0}\right) \quad (1.8)$$

where x_A and x_B are the momentum fractions of the colliding quarks; Q_0 is an arbitrary momentum scale; and $h_1(b, x_A)$, $h_1(b, x_B)$, and $h_2(b)$ are functions to be determined from experiment. In the Ladinsky-Yuan form[5], S_{NP} is

$$S_{NP}(b, Q) = g_1 b^2 + g_1 b^2 \ln\left(\frac{Q^2}{Q_0^2}\right) + g_1 g_3 b \ln(100 x_i x_j) \quad (1.9)$$

where x_i, x_j are the momentum fractions of the colliding partons. The values of g_1 , g_2 and g_3 are determined by fitting to the p_T distribution of vector bosons like the W , Z , or Photon. This has been done using Tevatron Run I results from Z data[14].

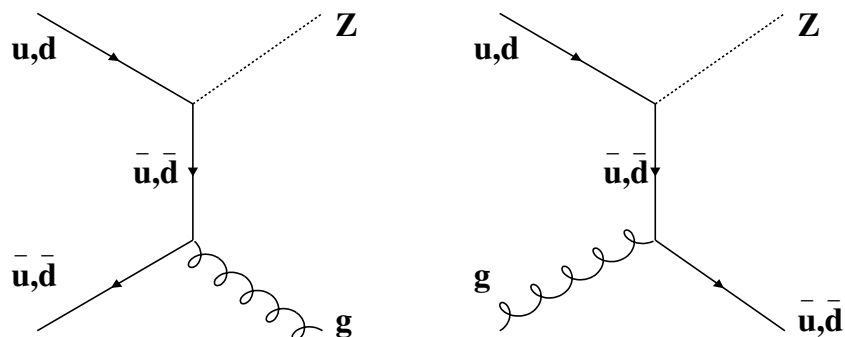


Figure 1.3: Initial state gluon radiation and Compton scattering in Z production.

1.4 Motivation for the Measurement of the Z Boson Transverse Momentum

There are several reasons for measuring the Z boson differential cross section $d\sigma/dp_T$.

First, the transverse momentum distribution of the Z boson is sensitive to the resummation calculation of the differential cross section, especially at low p_T . Second, in the high p_T region, the cross section tests the perturbative QCD part of the calculation. Third, the W boson shares the same production formalism as the Z boson, so the result of this measurement will also improve the knowledge of the production of W bosons, and thus reduce the theory uncertainty on the W mass measurement, which is a very important measurement since it can be used with other measurements to predict the Higgs mass. Although there are about ten times more W s than Z s produced in the semi-leptonic channels which are detectable in hadronic collisions, it is hard to directly reconstruct the p_T distribution of $W \rightarrow e\nu$ events, since a good measurement of the missing energy due to the neutrino is difficult.

The p_T distribution observed in experiments that scatter electrons off from nuclei (semi-inclusive deep inelastic scattering: SIDIS) is substantially wider than predicted by a conventional CSS calculation when $x < 0.01$. Stefan Berge et al.[4] modified the CSS formalism by introducing an extra x -dependent term in the Sudakov exponent. The interpretation of this term is that it mimics higher-order contributions of the form $\alpha_s^m \ln^n(1/x)$, which are not included in the resummed cross section. They also predicted the Z p_T distribution in forward Z boson production at the Tevatron Run II should be broadened as well, as shown in Fig. 1.4. With about 1 fb^{-1} data, we have more than 5000 Z bosons with $y > 2$, and we can perform a preliminary test of this prediction.

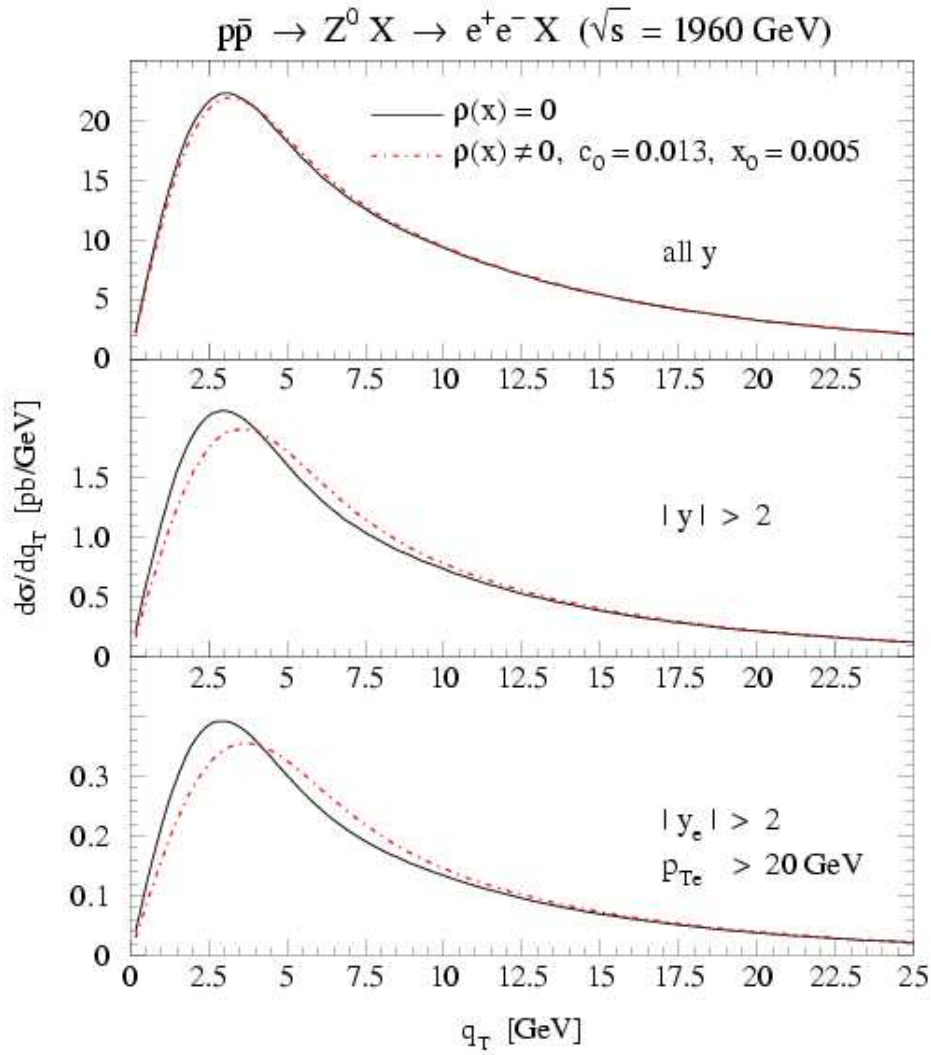


Figure 1.4: Theoretical predictions for the Z p_T spectrum at Tevatron Run II. The solid lines represent p_T spectrum calculated without small- x correction. The dashed lines represent those with the small- x correction.

Chapter 2

Fermilab Accelerator and DØ Detector

2.1 The Accelerator

The Fermi National Accelerator Laboratory is located at a western suburb of Chicago, Illinois. It is the site of the world's highest center-of-mass energy proton-antiproton colliding beam accelerator, the Tevatron. The Tevatron is a circular particle accelerator (or synchrotron) and consists of several stages to increase the energy of the protons and antiprotons. Figure 2.1 shows the layout of the accelerator system. A detailed description of the Tevatron can be found in [15]. The first step of the acceleration process begins with producing the hydrogen ions (H^-) from hydrogen gas using a Cockcroft-Walton accelerator. The Cockcroft-Walton accelerator then accelerates the H^- 's to an energy of 750 KeV before they are injected into a linear accelerator (the Linac), where they are accelerated to an energy of 400 MeV.

In the next step, the ions enter the Booster, a circular synchrotron nearly half a kilometer in circumference. They are directed through a thin carbon foil which strips off the electrons, leaving a beam of H^+ ions, which are bare protons. The steady beam of protons travels around the Booster, collecting more protons with each turn. After six revolutions, the Booster contains about 3×10^{12} protons, and the Linac ceases supplying them. The Booster then restores the bunch structure to the beam and accelerates the protons to 8 GeV.

In the third step, the protons are injected into a larger synchrotron, the Main Injector. The Main Injector is about two miles in circumference, was completed in 1999 and replaced the Main Ring that was used in the Tevatron Run I(1992-1996). With the Main Injector there is a factor of three increase in the number of protons that can be delivered to the Tevatron over what was possible in Run I.

In the Main Injector, part of the protons are accelerated from 8 GeV to 150 GeV before they are

injected into the Tevatron. The rest of the protons are accelerated to 120 GeV and directed onto a nickel target to produce antiprotons. For every about 10,000 incident protons, one antiproton is produced. The antiprotons are produced with a wide range of momenta. They are focused and stored in the Debuncher and Accumulator rings, where the beams are cooled, creating a beam of 8 GeV antiprotons to be injected into the Main Injector, and accelerated to 150 GeV. The 150 GeV antiprotons are then injected into the Tevatron in the direction opposite to the proton beam. The Tevatron is a synchrotron ring with a four mile circumference. It contains nearly 1,000 superconducting magnets which operate at a temperature of 4.6 Kelvin and provide a field of 4.2 Tesla. Once protons and antiprotons are accelerated to 980 GeV, low-beta quadrupole magnets squeeze the beams to small transverse dimensions. The beams are then brought into collision at two interaction points: $B\bar{O}$, where the CDF detector was built and $D\bar{O}$, the location of the other multi-purpose detector, also called $D\bar{O}$, since it was named after its interaction point.

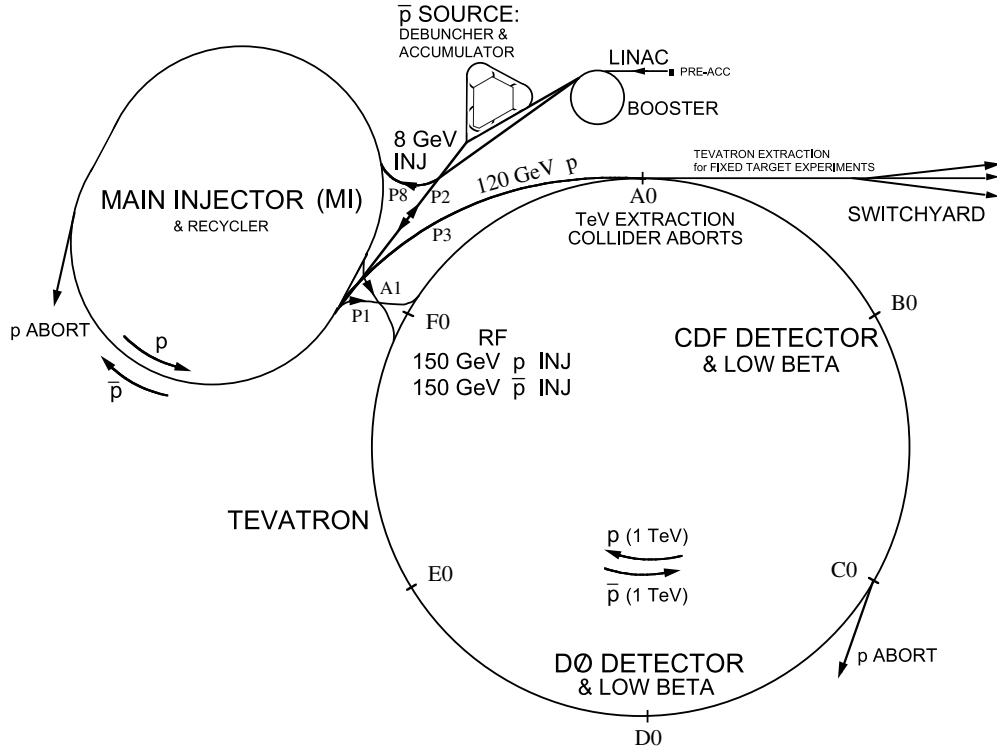


Figure 2.1: The general layout of the collider facility at Fermilab.

The bunch structure for Run I and Run II is shown in Fig. 2.2. In Run I, the accelerator

delivered 6 bunches of protons and antiprotons (“6 × 6” bunches), separated by a 3.5 μs gap. This gap was used to form the trigger and sample the detector baselines prior to the next crossing. In Run II, the proton and antiproton bunches circulate in superbunches of 4.36 μs duration, with a 2.64 μs gap spacing between them. The spacing between each bunch is 396 ns (“36 × 36” bunches).

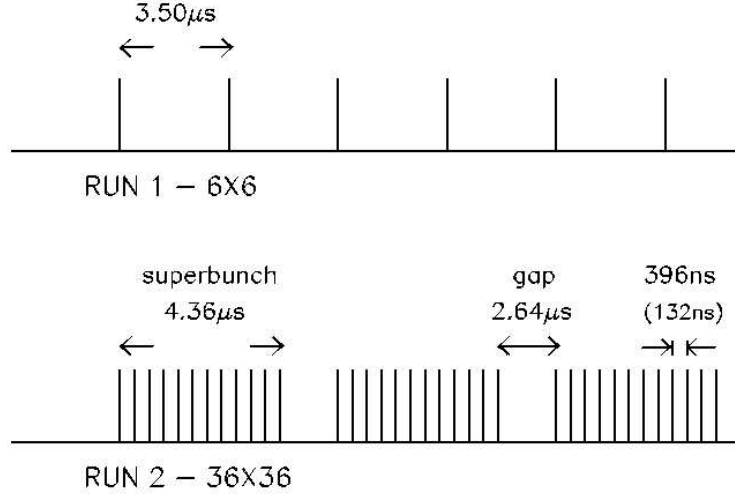


Figure 2.2: Tevatron bunch scheme for Run I (top) and Run II (bottom).

2.2 DØ Detector

The DØ detector is a multi-purpose particle detector designed for the study of high mass and large transverse energy phenomena. It consists of several different types of sub-detectors layered one-by-one around the expected interaction point.

The initial operation of the DØ detector started in 1992 with Run I of the Tevatron accelerator; it has played a key role in experimental high energy physics [17]. One example of this was the discovery of the top quark in 1995 with the CDF detector [18].

The Tevatron accelerator complex has been upgraded for the Run II which started in 2001 and the instantaneous luminosity was increased from $10^{31} \text{ cm}^{-2}\text{s}^{-1}$ in Run I to $10^{32} \text{ cm}^{-2}\text{s}^{-1}$ in Run II. Also the Tevatron beam energy was increased from 900 GeV to 980 GeV, increasing the $p\bar{p}$

center-of-mass collisions from 1.8 TeV to 1.96 TeV.

To take advantage of these improvements in the Tevatron and extend the physics reach of the experiment, the DØ detector went through a major upgrade. The details of the updated DØ detector are described in [16]. The upgraded DØ detector consists of three major subsystems: a tracking system with superconducting solenoid magnet, a nearly 4π solid angle uranium liquid argon calorimeter with two additional preshower detectors, and a muon toroidal spectrometer. Figure 2.3 shows an overview of the entire DØ detector.

2.2.1 The DØ Coordinate System

A right-handed coordinate system is defined with the origin at the center of the detector along the beam axis. The direction of the protons is the positive z direction, the positive x direction points away from the center of the Tevatron ring and thus the positive y direction points up. In spherical coordinates, the polar angle $\theta=0$ is set as the positive z direction and $\phi=0$ is set as the positive x direction. In cylindrical coordinates, r is defined as the distance to the beam line.

The rapidity y of a particle is defined as

$$y = \frac{1}{2} \ln \left(\frac{E + p_z}{E - p_z} \right) \quad (2.1)$$

The advantage of using rapidity is that it is invariant under the Lorentz transformation. If the energy of a particle is much larger than its mass ($m/E \rightarrow 0$), a handy variable called pseudo-rapidity is a good approximation to y . It is defined as:

$$\eta = -\log \tan(\theta/2) \quad (2.2)$$

To describe a conical region, it is convenient to define a variable:

$$R = \sqrt{(\Delta\eta)^2 + (\Delta\phi)^2} \quad (2.3)$$

where $\Delta\eta$ and $\Delta\phi$ are the η and ϕ differences between the compared objects.

Many of the particles produced in the $p\bar{p}$ collision, for example the remnants of the proton not participating in the hard-scattering interaction, escape down the beam pipe. Hence the

longitudinal boost of the center of mass system of the hard scattering partons cannot be measured. The transverse momentum of the particles that escape down the beam pipe is negligible compared to the detector resolution, making it possible to apply conservation of energy and momentum in the transverse plane. This makes the transverse momentum extensively used in hadron collider physics. It is defined as:

$$p_T = p \sin\theta \tag{2.4}$$

2.2.2 Tracking System

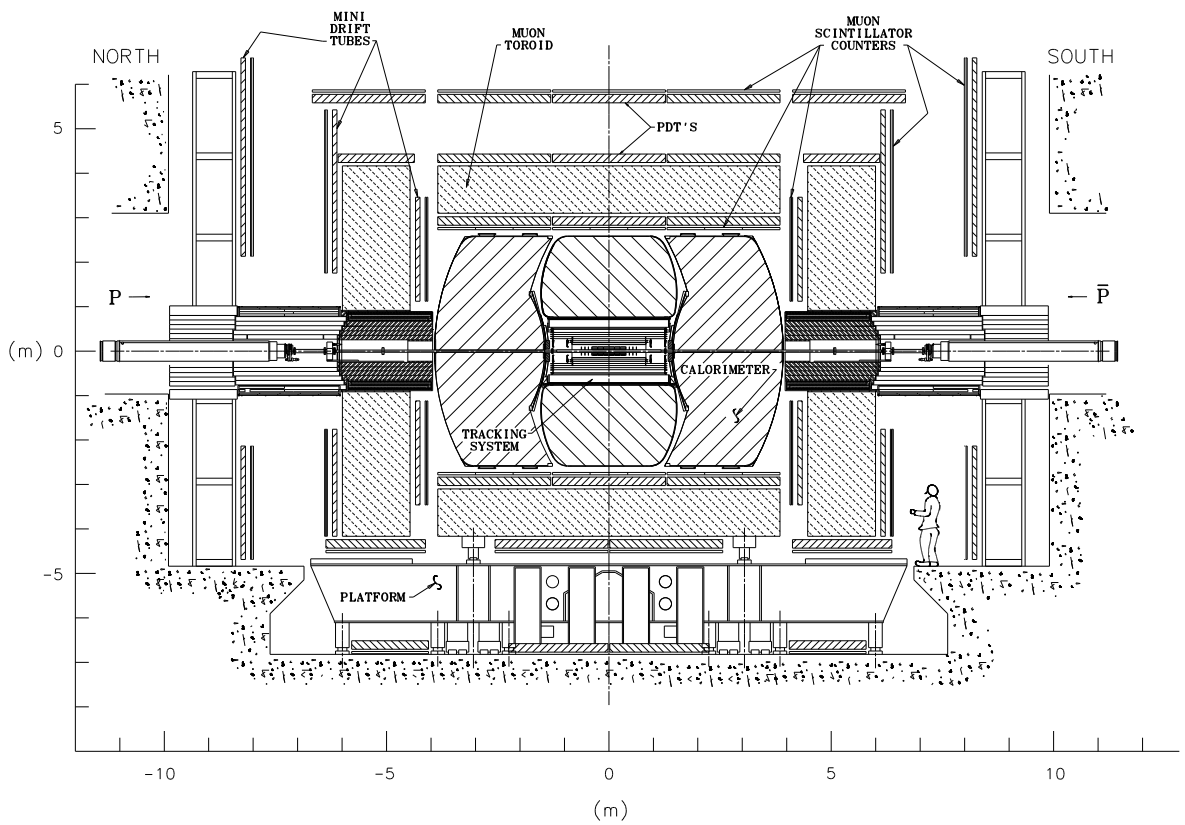
The central tracking system is designed to precisely measure the position of charged particles as they pass through the detector layers. The central tracking system in DØ Run II is composed of the silicon strip tracker(SMT) and the central fiber tracer(CFT), and is surrounded by a 2 Tesla superconducting solenoidal magnet. Fig. 2.4 shows the various components of the inner tracking detectors in DØ. The solenoid magnet bends the paths of charged particles with a curvature inversely proportional to their transverse momenta. Observing the curvature of a particle’s path allows for a precise measurement of its momentum, as well as the sign of the particle’s charge.

The Silicon Microstrip Tracker

The detector nearest to the interaction region is the Silicon Microstrip Tracker (SMT), which provides the high resolution position measurements of the charged particle paths that are used to reconstruct tracks and determine the vertex information [20]. Figure 2.5 shows an overview of the SMT detector. The SMT consists of six 12 cm long barrels, with interspersed disks (12 F-disks and 4 H-disks), and has approximately 793,000 readout channels with a $r\phi$ hit resolution of approximately 10 μm . The tracks for high η particles are reconstructed in three dimensions primarily by the disks, while particles at small η are detected primarily by the barrels.

The Central Fiber Tracker

The Central Fiber Tracker (CFT) surrounds the silicon detector, extends out to the solenoid magnet, and is used to aid the SMT in the reconstruction of charged particle tracks [21]. The CFT makes use of 76,800 scintillating fibers and can detect charged particles up to $|\eta|$ of 1.7.



900764
2/9/00

Figure 2.3: A view of the DØ Run II upgraded detector.

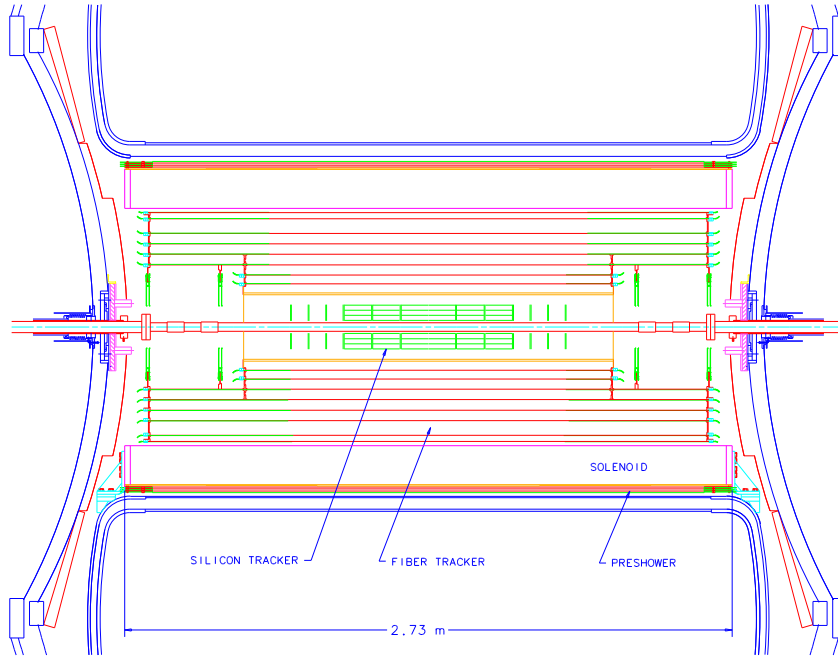


Figure 2.4: Cross-sectional view of the DØ tracking volume.

Each ionizing particle produces an average of about 10 photons in each fiber, which are then detected using a Visible Light Photon Counter (VLPC) that converts the photons into an electrical pulse. There are 8 super-layers, with each super-layer completely covered by two doublet layers of scintillating fibers. The innermost doublet layer is mounted along the axial direction to provide the ϕ information (called the x layer), and a stereo doublet-layer is on the top to provide the η (called the u/v layer, the u layer tilts 3 degree from the z axis clockwise and the v layer tilts 3 degree counter-clockwise). Each fiber is 835 microns in diameter and the position resolution is on the order of $100 \mu\text{m}$, corresponding to a ϕ resolution of 2×10^{-4} radians. Fig. 2.6 shows a view of the CFT as well as an illustration of the doublet layer configuration.

2.2.3 Preshower Detectors

The preshower detectors aid in electron identification and background rejection during both triggering and offline reconstruction. There are two preshower detectors located just before the

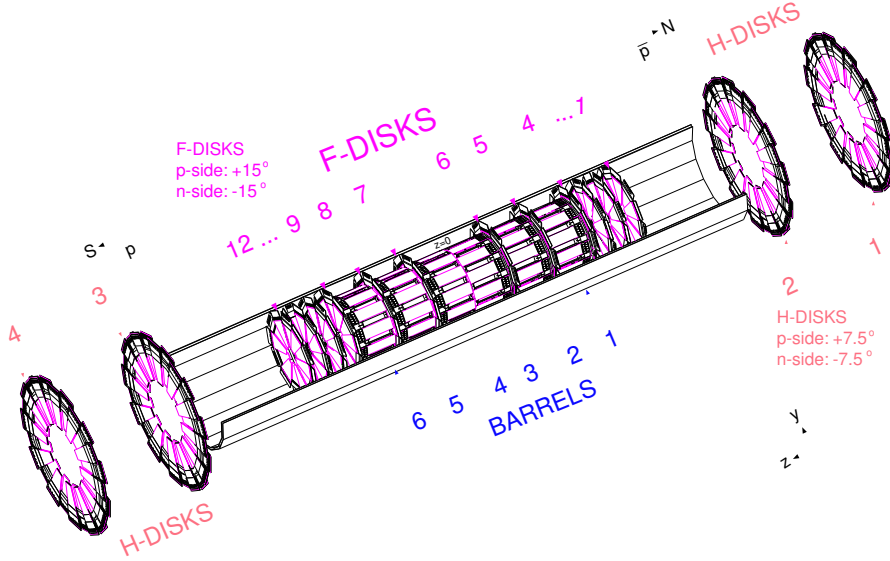


Figure 2.5: DØ Run II Silicon Microstrip Tracker detector.

calorimeters: a central preshower covering $|\eta| < 1.3$ (CPS), and a forward preshower covering $1.5 < |\eta| < 2.5$ (FPS) (shown in Fig. 2.7 and Fig. 2.8). The preshower detectors can provide discrimination between electrons/photons and hadronic jets by exploiting the differences between their energy loss mechanisms in showers.

The detectors function as a calorimeter by providing an early energy sampling and as a tracker by providing precise position measurements. The central system [22] consists of a lead radiator of two radiation lengths thickness at $\eta = 0$, followed by three layers of scintillating material arranged in an axial, $u - v$ geometry with a 22.5° stereo angle. The forward system [23] also consists of a lead radiator with a thickness of two radiation lengths, sandwiched between two layers of scintillating material. Each layer is made from two thinner layers of scintillating fibers, arranged in a $u - v$ geometry with a 22.5° stereo angle. Electrons are recognized based on the fact that muons and charged pions traversing the radiator will only deposit energy due to ionization, while electromagnetic particles will shower in the radiator.

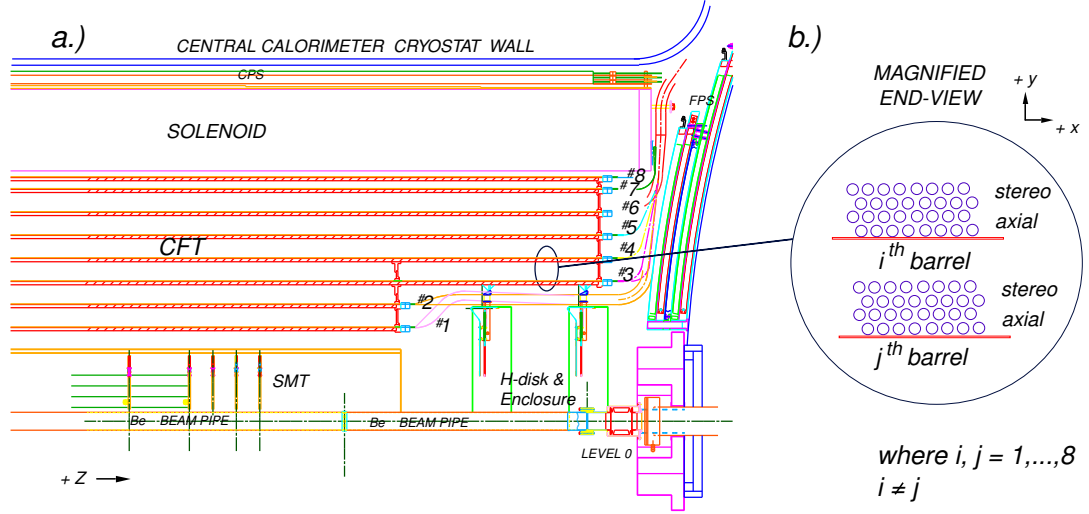


Figure 2.6: (a) A quarter $r - z$ view of the CFT detector showing the nested eight barrel design. (b) A magnified $r - \phi$ end view of the two doublet layer configuration for two different barrels.

2.2.4 Calorimeters

The $D\phi$ calorimeters have been designed to provide excellent measurement of the energy of photons, electrons and hadronic jets, by inducing them to create showers of energy using large amounts of dense material. The energy in the showers is then sampled at many points, to determine its shape and energy. Next, I will first describe the energy measurement in the calorimeter, then describe the calorimeter and its performance.

Energy Measurement

Electrons and photons interact with materials primarily via two processes: *pair production* ($\gamma \rightarrow e^+e^-$) and *bremsstrahlung* ($e \rightarrow e\gamma$). For each successive interaction the number of secondary particles increases while the average energy per particle decreases. It is the collection and measurement of these secondary particles that gives us information about the original EM object's energy. Because of these interactions, the energy of the original particle is expected to drop exponentially:

$$E(x) = E_0 e^{-x/X_0} \quad (2.5)$$

where E_0 is the particle's original energy, x is the distance traveled, and X_0 is the radiation

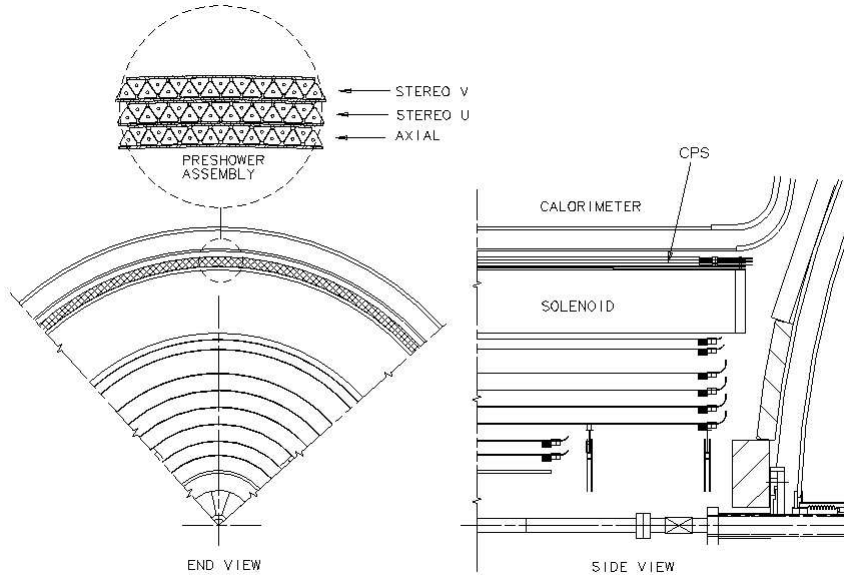


Figure 2.7: Cross-sectional end view (left) and side view (right) of the Central Preshower Detector.

length of the material being passed through. For uranium, X_0 is approximately 3.2 mm. For hadrons the interaction with material occurs with the nuclei via the strong nuclear force. These interactions also produce secondary particles, most of them are neutral pions (π^0) and charged pions (π^\pm). While the π^0 s produce electrons and photons which interact electromagnetically, the charged pions interact strongly. This type of particle shower tends to develop over longer distances and is also larger. The analog of the radiation length for hadronic interactions is the nuclear interaction length (λ_0), which is about 10.5 cm for uranium.

DØ Calorimeters

The DØ calorimeters are compensating sampling calorimeters, using liquid argon as the active medium and depleted uranium as well as copper and steel as absorber material. The choice of this configuration was driven by its ease of segmentation, compensation properties, stability of calibration, and homogeneity of response. The high density of uranium allows a compact detector that contains almost all shower energy while reducing cost.

There are three liquid argon calorimeters housed in three separate cryostats - one central (CC) (with $|\eta| < 1.1$) and two endcaps (EC) (with $1.5 < |\eta| < 4.2$). In the inter-cryostat region

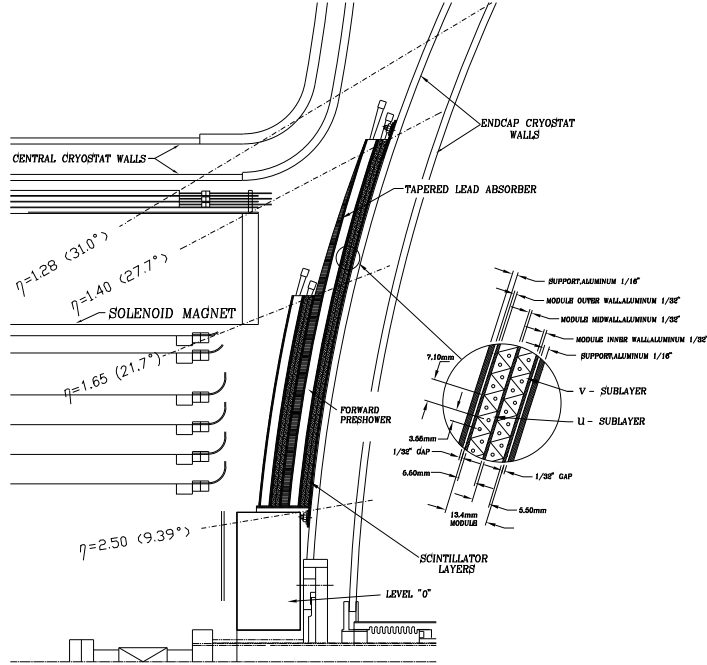


Figure 2.8: One quarter view of the Forward Preshower Detector.

($1.1 < |\eta| < 1.4$), both "massless gaps" and an inter-cryostat detector (ICD) have been added to sample the shower energy that is lost by particles that transverse the module endplates and cryostat walls.

Fig. 2.9 shows an overview of the $D\emptyset$ calorimeter system [24].

A typical calorimeter unit cell is shown in Fig. 2.11; The electric field is established by grounding the metal absorber plate and connecting the resistive surfaces of the signal boards to a positive high voltage (2.0 kV). Particles interact with the uranium and the liquid argon, thus producing charged particles in the liquid argon. These charged particles will then move in the electric field and be collected. The electron drift time across the argon gap is ~ 450 ns, which sets the time scale for the signal charge collection. The gap thickness was chosen to be large enough to observe minimum ionizing particle (MIP) signals and to avoid fabrication difficulties.

The pattern and sizes of the readout cells were determined from several considerations. The transverse sizes of the cells were chosen to be comparable to the transverse sizes of showers: 1-2 cm for EM showers and about 10 cm for hadronic showers.

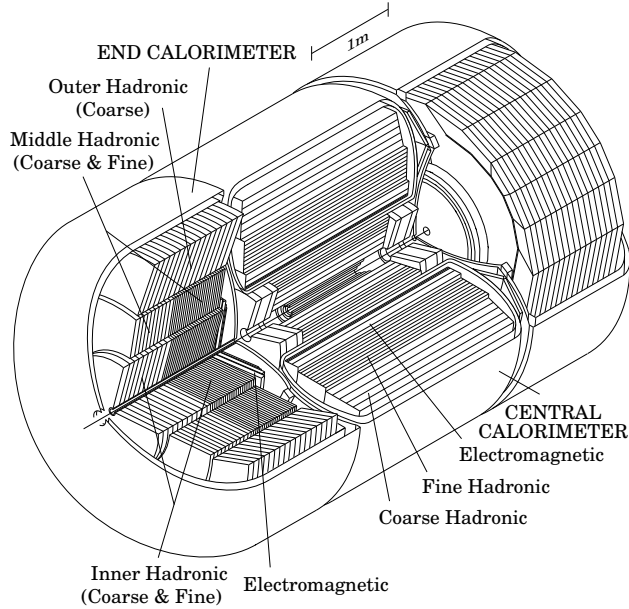


Figure 2.9: Overall view of the calorimeter system.

The cells are first ganged into layers, then arranged into semi-projective towers of size 0.1×0.1 in $\Delta\eta \times \Delta\phi$, and are segmented longitudinally into electromagnetic (EM), fine hadronic (FH), and coarse hadronic (CH) sections. The third layer of the EM section, which corresponds to the shower maximum, is segmented more finely transversely into 0.05×0.05 in $\Delta\eta \times \Delta\phi$.

A cross sectional view of one quarter of the detector, showing the η and depth segmentation is shown in Fig. 2.10.

Different absorber plate materials were used in different locations. The EM modules for both CC and EC used nearly pure depleted uranium; the thicknesses were 3 mm and 4 mm respectively.

The fine hadronic module sections have 6-mm-thick uranium-niobium (2%) alloy. The coarse hadronic module sections contain relatively thick (46.5 mm) plates of either copper (CC) or stainless steel (EC). For the CC, the EM section consists of 32 modules, each subtending $2\pi/32 \approx 0.2$ radians in azimuth.

Table 2.1 and 2.2 list the major parameters for the central and endcap calorimeters. At $\eta = 0$, the CC has a total of 7.2 nuclear absorption lengths; at the smallest angle of the EC, the total is 10.3 nuclear absorption lengths.

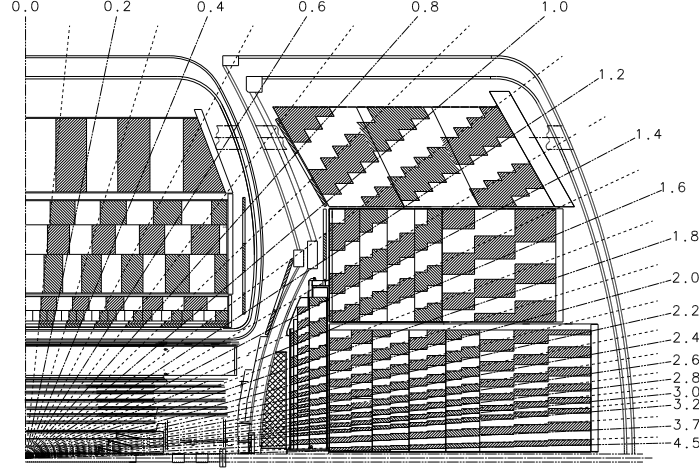


Figure 2.10: Side-view of one quarter of the $D\bar{O}$ calorimeter system, showing segmentation and tower definitions. The line extending from the center of the detector denote the pseudo-rapidity coverage of cells and projected towers.

Calorimeter Performance

The performance of the calorimeter is very crucial for the $Z p_T^{ec}$ measurement. The energy resolution can be empirically described using three parameters:

$$\frac{\sigma_E}{E} = \sqrt{\left(\frac{N}{E}\right)^2 + \left(\frac{S}{\sqrt{E}}\right)^2 + C^2} \quad (2.6)$$

where N , S and C are called the noise, sampling, and constant terms, respectively. The noise term has a fixed value, independent of the observed signal. It is due to the “noise” from the uranium decay, readout electronics and the underlying events. The sampling term which reflects statistical fluctuations in the energy deposited in the argon and therefore scales like the square root of the signal size. The third is the constant term, which reflects how well the response of different parts of the detector are equalized, in other words, how well we understand and calibrate the entire calorimeter. It therefore scales linearly with signal size, assuming the energy is distributed over approximately the same number of readout cells, independent of energy.

In Run I, these three terms were determined to be: $N = 0.003$ GeV, $S_{EM} = 0.15$ GeV^{1/2} [28] [29] and $C = 1.15^{+0.27\%}_{-0.36\%}$ [30]. The values for Run II will be discussed in Chapter 5.

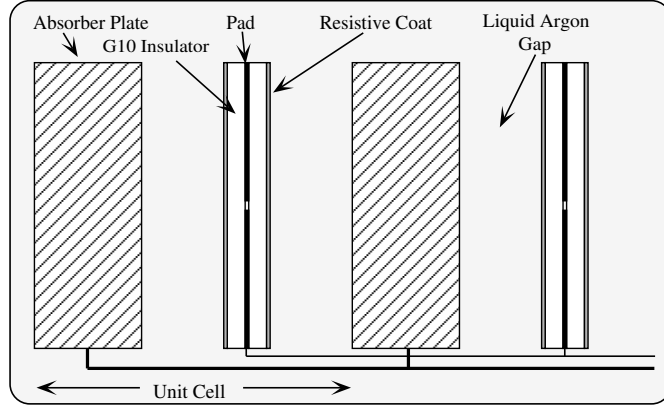


Figure 2.11: Schematic view of a representative calorimeter unit cell. The gap structure, grounded absorber plates, and signal boards are shown.

2.2.5 Muon System

Outside of the calorimeter is the muon system [31]. Muons are about 200 times heavier than electrons, therefore they lose very little energy via bremsstrahlung, unlike electrons. In the detector media, muons lose energy mostly due to ionization, which is a low energy loss absorption process. Therefore, muons above a certain energy threshold (about 3 GeV) pass through the whole $D\bar{O}$ detector. Since muons are measured after the electromagnetic and hadronic particle showers are absorbed in the calorimeters, they can be identified in the middle of hadron jets with much greater purity than electrons.

The muon system has three layers of detectors giving position measurements, and a toroid magnet with a 1.8 T field located between the first and second layer, allowing a measurement of momentum. Position measurements are provided by drift chambers. These chambers are made of rectangular aluminum tubes filled with gas which is ionized by charged particles passing by. The chambers are arranged in planes. The central muon system is made up of four planes surrounding the calorimeter and providing coverage up to $|\eta| \sim 1$. Two further planes of detectors are located at either end of the calorimeter, making up the forward muon system. These extend the detector coverage out to $|\eta| \sim 2.2$. The drift chambers provide an accurate (to within 0.5 mm) measurement of the coordinate perpendicular to the sense wires (corresponding

	EM	FH	CH
Number of Modules	32	16	16
Absorber	Uranium	Uranium	Copper
Absorber Thickness (mm)	3	6	46.5
Argon Gap (mm)	2.3	2.3	2.3
Number of Readout Layers	4	3	1
Cells per Readout Layer	2, 2, 7, 10	20, 16, 14	9
Total Radiation Length (X_0)	20.5	96.0	32.9
Total Interaction Length (λ)	0.76	3.2	3.2

Table 2.1: Central Calorimeter Module Parameters.

to η). The muon detectors also have layers of scintillating material arranged in pixels; these provide the best measurement of the other coordinate (corresponding to ϕ). Signals from the drift chambers and scintillators in each region are combined into segments. Segments are then joined in a fit, with a measurement of the bending in the toroidal magnetic field giving a measurement of muon momentum. Fig. 2.12 and Fig. 2.13 shows the exploded view of the drift chambers and the scintillation counters respectively.

2.3 Luminosity System

The expected number of events produced in $p\bar{p}$ collisions for a process is given by:

$$N = \sigma \mathcal{L} \tag{2.7}$$

where σ is the cross section of this process and \mathcal{L} is the integrated luminosity, with a unit called barn, 1 barn = 10^{-24} cm⁻². The integrated luminosity is calculated by integrating the instantaneous luminosity over time:

$$L = \int_{t_1}^{t_2} f n \frac{N_p N_{\bar{p}}}{A} dt \tag{2.8}$$

	EM	IFH	ICH	MFH	MCH	OH
Number of Modules	1	1	1	16	16	16
Absorber	Uranium	UNb	SS	UNb	SS	SS
Absorber Thickness (mm)	4	6	46.5	6	46.5	46.5
Argon Gap (mm)	0.23	0.21	0.21	0.22	0.22	0.22
Number of Readout Layers	4	4	1	4	1	3
Cells per Readout Layer	2, 2, 6, 8	16	14	15	12	8
Total Radiation Length (X_0)	20.5	121.8	32.8	115.5	37.9	65.1
Total Interaction Length (λ)	0.95	4.9	3.6	4.0	4.1	7.0

Table 2.2: End Calorimeter Module Parameters. IFH, ICH, MFH, MCH, OH stand for inner fine hadronic, inner coarse hadronic, middle fine hadronic, middle coarse hadronic and outer hadronic section respectively. UNb and SS stand for Uranium-Niobium alloy and Stainless Steel.

where f is the revolution frequency(47.713 kHz), N_p and $N_{\bar{p}}$ are the numbers of protons and antiprotons in a bunch respectively, n is the number of bunches in either beam and A is the cross sectional area of the beam interaction region.

The luminosity is measured at $D\bar{O}$ with the aid of the luminosity monitors, which are mounted 1.35 meters away from the center of the detector at either end, with a coverage $2.7 < |\eta| < 4.4$. Each luminosity monitor consists of 24 wedge shaped scintillation counters surrounding the beam pipe. The luminosity monitors detect the high rapidity particles produced in inelastic processes. Because the mean number of interactions that will occur when the beams cross should be proportional to the instantaneous luminosity, with the knowledge of the inelastic cross sections and the acceptance for these processes, the luminosity can be determined by counting the number of events found.

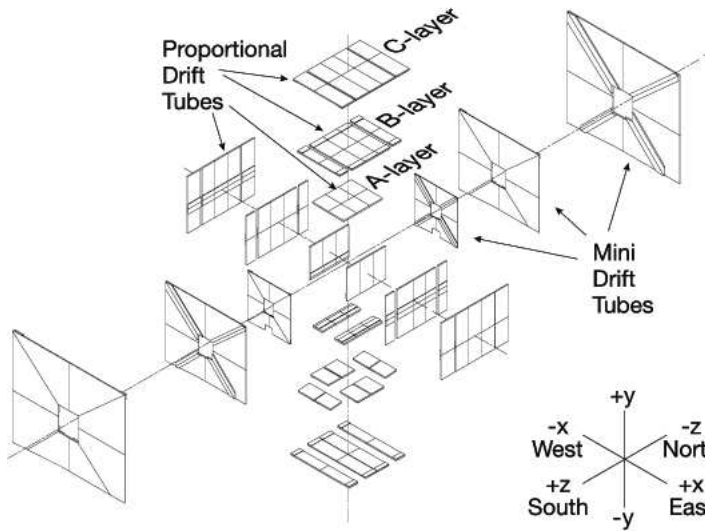


Figure 2.12: Exploded view of the muon wire chambers

2.4 Trigger System

The proton-antiproton beams make about 1.7 million collisions per second at the center of the DØ detector. The information collected for each collision is called an event. Not every event needs to be saved to the tape. Actually, roughly only a few collisions in a million are of physics interest. The task of the trigger system is to reduce this rate by evaluating events and deciding whether they are interesting or if they can be discarded.

With the increased luminosity and higher interaction rate delivered by the upgraded Tevatron, a significantly enhanced trigger was necessary to select the interesting physics events to be

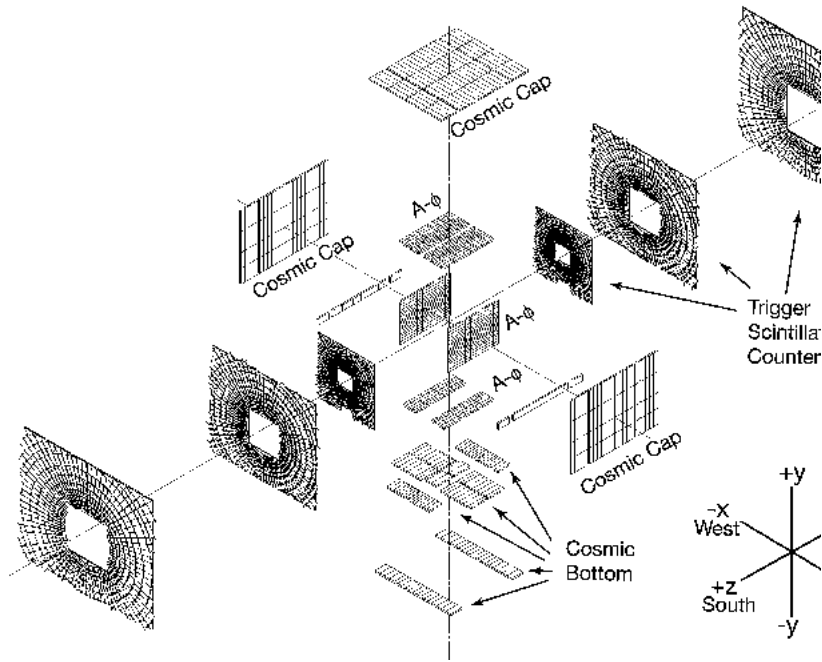


Figure 2.13: Exploded view of the muon scintillation detectors

recorded. Three distinct levels form this new trigger system: the level 1 trigger (L1) consists of a collection of hardware trigger elements that were designed to have an output rate of 2 kHz; in the level-2 trigger (L2), hardware engines and embedded microprocessors associated with specific sub-detectors provide information to a global processor to construct a trigger decision based on individual objects as well as object correlations. The L2 output rate is about 1 kHz; Candidates passed by L1 and L2 are sent to a farm of level 3 (L3) microprocessors, where sophisticated algorithms reduce the output rate to 50 Hz (shown in Fig. 2.14).

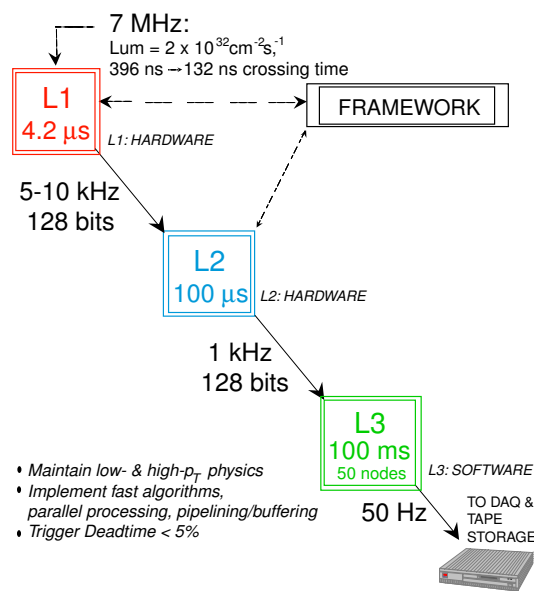


Figure 2.14: Summary of the three-level $D\bar{O}$ trigger system for Run II with the decision time and bandwidth allocated to each level.

Chapter 3

Event Selection

3.1 Data Set

Since the start of Run II in 2001, the DØ detector has collected about 1.6 fb^{-1} data; Fig. 3.1 shows the integrated luminosity delivered by the Tevatron collider and recorded by the DØ detector since 2001 [36].

The sample used for this particular analysis was collected from October 2002 to November 2005. The detector, on occasion, does not function properly. The detector and the data is monitored continuously by the collaboration for signs of problems, and data taken during a period when one is detected is marked. Runs declared bad for calorimeter, silicon tracker or central fiber tracker due to hardware failure or unusually large electronics noise [37] are removed from this sample, leaving a total of $976 \pm 59 \text{ pb}^{-1}$ of integrated luminosity.

Events that have fired one or more triggers are stored on tape and sent to a farm containing hundreds of standard x86-based Linux computers for reconstruction. The information recorded is in the form of “raw” digital signals, which need to be interpreted as physics objects. This complicated task is performed by the standard reconstruction software package, called DØ Offline Reconstruction Program(DØRECO) [38]. The time used to reconstruct one event takes about 15 to 30 seconds on a 1 GHz machine.

DØRECO reconstructs events in four hierarchical steps: first, detector unpackers unpack the RDC (Raw Data Chunk) which is created by the Level 3 trigger system, then apply detector specific calibration constants. This information is then converted to clusters or hits. During the second step, the hits in the tracking system are grouped together and used to reconstruct global tracks. The third step is vertexing. Since the beams have a finite extent along their direction of travel (the z direction), the z positions of the hard scatterings have a Gaussian distribution with

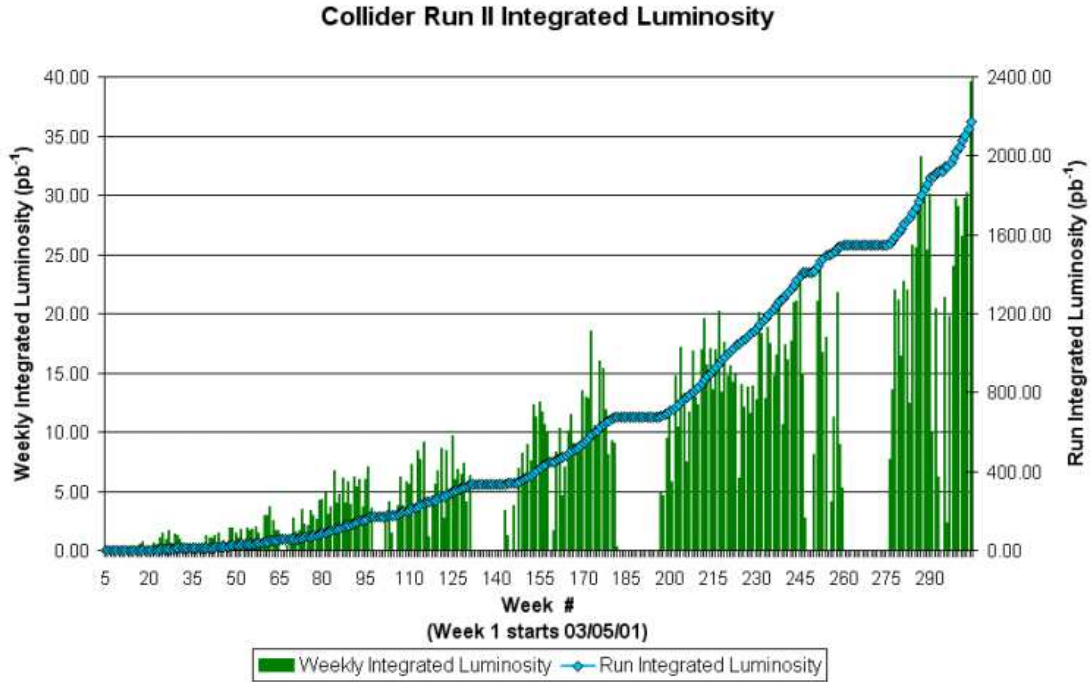


Figure 3.1: Integrated luminosity delivered by the Tevatron Collider and recorded by the DØ detector (pb^{-1}).

a r.m.s. of about 25 cm. The z location of the hard scattering and of any additional soft scatterings (“primary vertices”) are located during the vertexing step. After that, the displaced secondary vertex candidates which are associated with the decays of long-lived particles are identified. The final step of DØRECO is particle identification. It first finds electron, photon, muon, neutrino (missing E_T) and jet candidates, which are based on detector, track and vertex objects. Finally, using all previous results, candidates for heavy-quark and τ decays are identified. In the following, I concentrate on track, vertex and electron reconstruction, since they are the most important for this measurement.

3.2 Track and Vertex Reconstruction

The track reconstruction focuses on finding trajectories of charged particles passing through the tracker layers using the hits left in the detector. These hits are formed by grouping readout channels in a single tracker layer. The extrapolation of the track is then performed by a road following algorithm[39]. The basic idea of the algorithm is to start with a track segment consisting of three hits and iteratively building up the track by matching to hits in adjacent layers.

The track + hits combination is fit to a curve and a χ^2 test is performed to determine if the hit should be added. If no hit is matched in a layer then it is referred to as a miss. A final list of track candidates is then produced and ordered according to track quality, which is based on number of hits, fewest misses and best χ^2 value.

The interaction point of an event is called the *event vertex*. There are two types of vertices: primary and secondary vertices. A primary vertex is the original interaction point, and generally has the largest number of associated tracks. There can also be additional minimum bias vertices associated with soft scatterings of protons and antiprotons in the same bunches as the ones that produced the hard scattering. Finding the primary vertex of an event is very important because it is needed for many purposes, such as the reconstruction of electrons, photons, and jets. The x and y coordinates of the primary vertex is expected to be very close to the beam line[40] however the z coordinate varies considerably with a rms width of 25 cm and a central value close to zero [41]. The details of the algorithm for used to find primary vertices is described in [42]. It has three steps. The first step consists of selecting all tracks in the events which have transverse impact parameter significance with respect to beam position smaller than 3.0. Here, *impact parameter significance* is defined as the distance of closest approach with respect to the beam line divided by its uncertainty. In the second step, all tracks are fitted together and the χ^2 contribution of each track to the vertex is computed. The track with the highest χ^2 is excluded and the vertex is re-fitted. The process is repeated until the χ^2 value is smaller than 10. The same finding procedure is repeated to find more vertices using the tracks not already included in

a vertex. The final step is then to select the primary vertex with the highest $\Sigma \log(p_T)$, where the sum runs over all the tracks for the vertex. The algorithm is designed this way in order to select vertices from hard scattering interactions, and exclude ones from secondary interactions or minimum bias interactions, which are characterized by low p_T , high rapidity tracks.

A secondary vertex is a displaced vertex due to long-lived meson decay (e.g. B , K_s or D).

Secondary vertices are not used in this analysis because the Z boson is a short-lived particle and can always be considered as decaying at the primary vertex.

3.3 Electron Identification

The identification of both electrons and photons is based on clusters of calorimeter energy called EM objects. A simple cone algorithm is used to find EM objects in the EM calorimeter. The seeds are EM towers of high transverse energy¹(greater than 500 MeV). EM clusters are made around these seeds by adding towers within a cone of $\mathcal{R}(\sqrt{(\Delta\eta)^2 + (\Delta\phi)^2})=0.2$.

To be considered an EM object, the cluster needs to have a minimum transverse energy of 1.5 GeV, a minimum EM fraction of 0.9 and an isolation less than 0.2. The EM fraction is defined as the ratio of the EM energy to the total energy in the cluster. The isolation variable is defined as:

$$f_{iso} = \frac{E_{tot}(0.4) - E_{EM}(0.2)}{E_{EM}(0.2)} \quad (3.1)$$

where $E_{tot}(\mathcal{R})$ and $E_{EM}(\mathcal{R})$ are total energy and EM energy, respectively, in the cone with radius $\mathcal{R}=\sqrt{(\Delta\eta)^2 + (\Delta\phi)^2}$.

Since hadron jets² usually deposit only a small amount of their energy in the EM calorimeter, and electrons from W and Z boson decays tend to be isolated from other particles, EM fraction

¹Transverse energy(E_T) is the part of the energy measured by the calorimeter in the transverse plane, which is perpendicular to the beamline

²A jet is a cone of hadrons and other particles produced by the hadronization of a quark or a gluon. Because of the QCD confinement of color charged particles, such as quarks, can not exist in free form; therefore they fragment into hadrons before they can be directly detected. The jets, like electrons, deposit their energies in the calorimeter, but with different lateral and longitudinal shower developments. However, there is a chance that a jet still passes the electron selection requirements and is mis-identified as an electron.

and isolation provide powerful discrimination between the EM objects and hadronic jets.

At this stage, various quantities that describe cluster properties are computed and stored. A few examples are cluster energy, η and ϕ direction, H-matrix, EMID and In_fiducial.

The electron energy is computed from the signals in all EM towers within a window of 0.5×0.5 in $\Delta\eta \times \Delta\phi$ (5×5 towers) (for CC) or within a cone of 10 cm radius in EM3 (for EC) centered on the tower which registered the highest fraction of the electron energy.

The calorimeter shower centroid position is determined using a log-energy-weighted algorithm. If an electron has a matched track, the direction of this electron is then given by the direction of the matched track. If the electron does not have a matched track, then the calorimeter shower centroid position and the primary vertex position are used to define the electron direction.

The shower shape of an electron has a longitudinal and transverse profile that is quite distinct from that of a jet. To obtain the best discrimination against hadrons, the reconstruction code uses both longitudinal and transverse shower shapes, along with the correlations between energy deposits in the calorimeter (preshower) cells. This is done using a covariance matrix (H-matrix) technique. The H-matrix(7) is built up with a set of seven variables:

- EM fraction in EM calorimeter layers EM1
- EM fraction in EM calorimeter layers EM2
- EM fraction in EM calorimeter layers EM3
- EM fraction in EM calorimeter layers EM4
- Area of the EM cluster at the third floor(2D)
- $\log_{10}(\text{Energy})$
- vertex z position

The H-matrix(8) is built up from these seven variables and the following one:

- Transverse width of shower (1-D)

Another variable called EMID is used to tag likely candidates. An electromagnetic cluster is assigned an ID of 10 if it has $E_T > 1.5$ GeV and $f_{EM} > 0.9$. If the cluster also has a track loosely matched to it, it will be assigned an ID of ± 11 , depending on the sign of the track (+11 for electron, -11 for positron)[45].

A boolean variable called In_fiducial is true when the EM object is in a well-understood region of the calorimeter. There are 32 equal modules in the CC region, and the modules are located at $\phi = 2\pi N/32$, where $N = 0, 1, \dots, 31$. The ϕ module boundaries are excluded with cuts: $\text{mod}(\phi, 2\pi/32) < 0.1$ and $\text{mod}(\phi, 2\pi/32) > 0.9$. Electrons near the ends of the calorimeter are also excluded, with cuts: $|\eta_{det}| < 1.05$ ³ for central calorimeter and $1.5 < |\eta_{det}| < 3.2$ for End Cap calorimeter.

3.4 Offline Selection Criteria

Electrons from Z/γ^* decay typically have large p_T and are usually well isolated; thus the requirements for an electron to pass the selection are as follows:

- $p_T > 25$ GeV/c
- $|\eta_{det}| < 1.1$ (Central Calorimeter) or $1.5 < |\eta_{det}| < 3.2$ (End Cap Calorimeter)
- ID=10 or ± 11 , $f_{EM} > 0.9$, $f_{iso} < 0.15$
- is in fiducial region of the calorimeter
- not in a bad calorimeter region
- H-matrix(7) < 12 for CC electrons, H-matrix(8) < 20 for EC electrons

The bad calorimeter regions that have identified hardware problems are discussed in [41]. Monte Carlo comparisons with and without these cuts indicate an acceptance loss of 20% for Z

³There are two kinds of η used in this analysis: detector η (or η_{det}) and physical η (η_{phys} or simply η). η_{det} is derived from the angle between the beamline and the line linking the center of the detector and the cluster position in the EM calorimeter; η_{phys} is derived from the physical polar angle between the beamline and the line linking the interaction vertex and the cluster position. η_{phys} is thus related to the true angle made by the particle with respect to the detector whereas η_{det} is related to the true position of the particle in the detector.

candidate events. These hardware problems only happen for runs before 180956; 153 pb^{-1} of our data sample is affected.

An important source of background for electrons is QCD jet faking as electron. This background can be greatly reduced by requiring a track from a charged particle in the tracking detector be consistent with the position of the cluster in the calorimeter.

The χ^2 variable is constructed as:

$$\chi^2 = \left(\frac{\Delta\phi}{\sigma_\phi}\right)^2 + \left(\frac{\Delta z}{\sigma_z}\right)^2 \quad (3.2)$$

where $\Delta\phi$, Δz are the angle difference and the spatial difference between the electron position and the extrapolated track position, σ_ϕ and σ_z are the tracking resolutions in ϕ and z direction, respectively. Tracks with a track match significance χ^2 probability > 0.01 are considered good spatial matches.

The offline selection for the $Z/\gamma^* \rightarrow e^+e^-$ sample is as following:

- for CC-CC ⁴ event, each electron has a spatial track match ($P(\chi^2) > 0.01$)
- for CC-EC and EC-EC event, at least one electron has a spatial track match
- the invariant mass of the two electrons is between [70,110] GeV/ c^2
- at least one of the two electrons fires a single EM trigger.

If there are more than 2 electron candidates, the two electron candidates with the highest p_T are used. This results in a sample of 63656 candidate events.

Table 3.4 shows the result of event selection for different electrons in different calorimeter regions.

CC-CC	CC-EC	EC-EC	All
23957	30116	9583	63656

Table 3.1: Results of event selection

⁴If two electrons from Z decays are both located in CC or EC region, we call it a CC-CC or EC-EC Z candidate; if one electron is located in CC region and the other one located in EC region, we call it a CC-EC Z candidate.

Fig. 3.2 shows the invariant mass distribution of the Z boson candidate events.

Fig. 3.3 shows the p_T distribution of the Z boson candidate events.

After data selection, some corrections need to be applied. First, the background contribution needs to be subtracted. Then the effect of the event selection on the observed p_T spectrum needs to be corrected. Finally, we need to unfold the detector response to get the detector independent p_T spectrum.

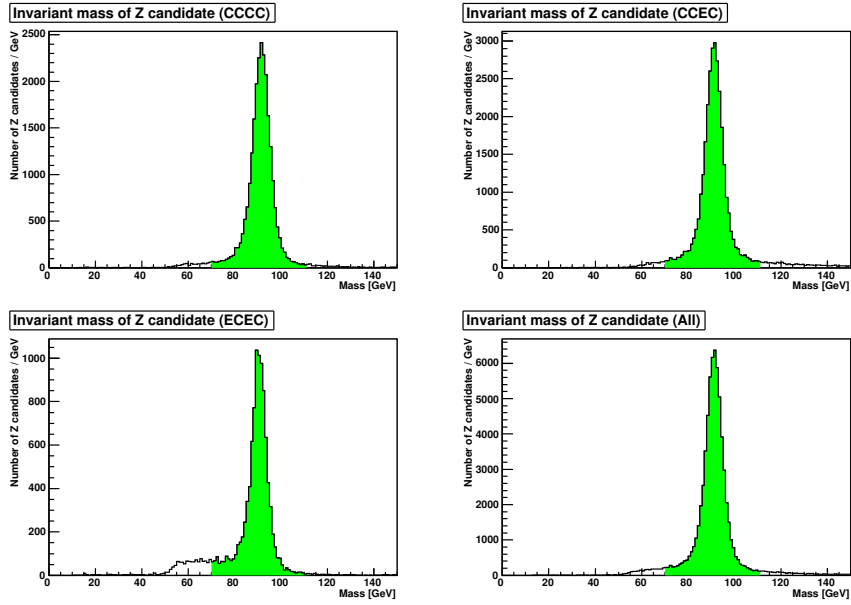


Figure 3.2: Invariant mass distribution of $Z/\gamma^* \rightarrow e^+e^-$ candidates.

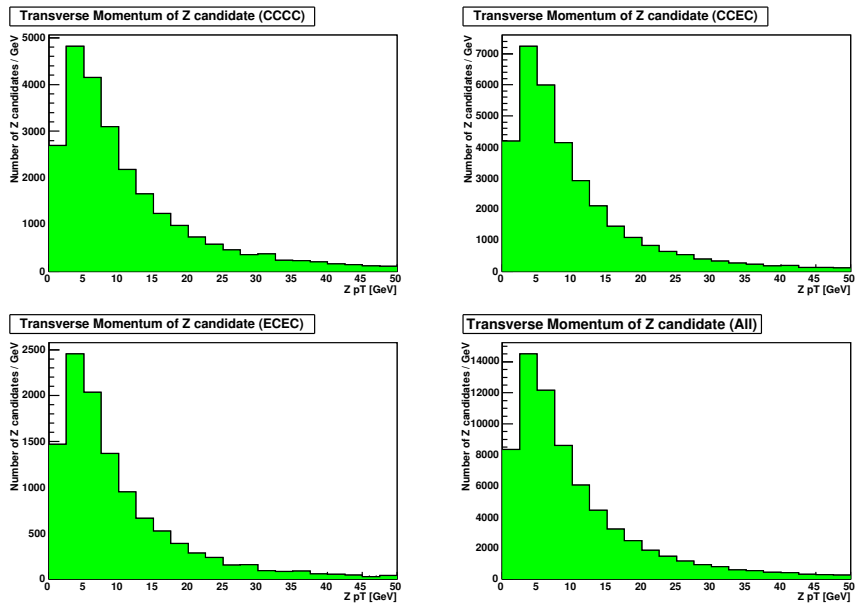


Figure 3.3: p_T distribution of $Z/\gamma^* \rightarrow e^+e^-$ candidates.

Chapter 4

Single Electron Efficiencies

When selecting single electrons, there are two main sources of inefficiency: those related to the hardware trigger, and those related to electron identification. To understand the selection effect, it is important to measure the efficiencies of these selection cuts, as well as their kinematic dependences. These dependences will be modeled in the parameterized Monte Carlo program which will be discussed in Chapter 5.

The selection efficiencies for single electrons are measured from $Z/\gamma^* \rightarrow e^+e^-$ data using a “tag and probe” method. The “tag and probe” method is a way of obtaining a relatively background free sample of inclusive electrons without using the electron identification cuts. Z events are identified using just one of the Z 's decay electrons. The second electron in the events then provides a relatively unbiased electron sample that can be used to evaluate selection efficiencies. In practice, one leg of $Z/\gamma^* \rightarrow e^+e^-$ is required to pass very tight electron identification cuts (the tag electron), while the other leg only needs to pass very loose cuts (probe electron). For this analysis, the tag electron is always required to pass all the single EM requirements and the trigger requirement. If both electrons in an event satisfy the tag electron requirements, they are both then considered as tags as well as probes.

The efficiencies are measured in the following order:

- Preselection efficiency
- Spatial track matching efficiency
- Trigger efficiency
- H-matrix efficiency

Probe electrons must pass all the requirements of the previous selections. Using this method, it is important to carefully correct for background contribution, which is a concern for the preselection

and spatial track-matching efficiencies. For trigger and H-matrix efficiencies, since spatial track match has already been required for the probe electron, the level of background is very small.

4.1 Preselection Efficiency

The preselection efficiency is defined as the efficiency of an EM object satisfying kinematic ($p_T > 25 \text{ GeV}/c$) and geometric requirements to pass following electron identification requirements:

- ID=10 or ± 11
- $f_{EM} > 0.9$
- $f_{iso} < 0.15$

The data sample used to study the preselection efficiency is a skimmed data¹, which requires each event to have at least one electromagnetic cluster with ID=10 or ± 11 and $p_T > 20 \text{ GeV}/c$. The tag is an electron satisfying trigger, kinematic, geometric, preselection, H-matrix and spatial track match requirements. Since we are trying to evaluate the efficiency of the basic calorimetry requirements, we do not want to use calorimeter information to identify the probe electron.

Instead, the probe is chosen as a good track, satisfying:

- $p_T > 12 \text{ GeV}/c$
- DCA < 1.0 cm. This cuts on the Distance of Closest Approach to the beam line in the transverse plane.
- $\chi^2 < 8.0$. This is the χ^2 from the track fit.
- $0.1 < \phi_{mod}$ of track at the calorimeter < 0.9 (CC region only). This avoids the central calorimeter ϕ crack.

¹In experiments like DØ, a lot of data is recorded but usually only a small part of it fits the needs of a specific analysis. To reduce the amount of data one needs to process, different working groups make their own “skims” by applying preliminary event selections.

- No muon candidate within $\mathcal{R}(=\sqrt{\Delta\eta^2 + \Delta\phi^2})=0.2$
- p_T sum of the other tracks within $\mathcal{R}=0.4$ of the probe track less than $3 \text{ GeV}/c$. This is the isolation requirement.

Additionally, we also require the tracks from the tag and the probe satisfy:

- $\Delta z(\text{tag EM, probe track}) < 2 \text{ cm}$. This makes sure they are from the same vertex.
- $\Delta\phi(\text{tag EM, probe track}) > 2$. This makes sure that they are back-to-back in ϕ .
- $65 < \text{invariant mass calculated from the tag EM cluster and the probe track} < 115 \text{ GeV}/c^2$

EM clusters are matched to the track if they are within $\mathcal{R} = 0.1$ of the track position extrapolated to the third floor of the EM calorimeter. The highest p_T EM cluster that matches the probe track is checked to see if passes the preselection requirement.

The main background source for this data is QCD multi-jet events, where two jets fake two electrons, or $W + \text{jets}$ events, where a jet fakes an electron. After checking the preselection requirements for the probe electron, the data sample is divided into four categories: passing with opposite sign charge (PO), passing with same sign charge (PS), failing with opposite sign charge (FO), failing with same sign charge (FS). Fig. 4.1 and Fig. 4.2 presents the invariant mass distribution for the four different groups separately for probe tracks in CC and EC regions, respectively.

The plots of FO and FS are made using the calorimeter information of the tag electron and the tracking information of the probe track. Since we have a better energy resolution in the calorimeter than in the tracking system, for the plots of PO and PS, we use the calorimeter information of the tag and the calorimeter information of the EM object that is matched to the probe track. We expect the signal to have opposite sign charge EM objects while background to have random relative signs. So the same sign samples PS and FS are considered backgrounds. However, due to possible charge mis-identification, the signal could have a same sign charge. Before the track matching, most of the same sign events are backgrounds. After the track matching, most of the left same sign events are signals. This is also shown from the invariant

mass distribution: PS has a very clear Z peak, which indicates that the events in this sample are mostly from Z boson decays.

Defining the number of probes passing with opposite sign as P_o , the number of probes passing with same sign as P_s , the number of probes failing with opposite sign as F_o , the number of probes failing with same sign as F_s , the preselection efficiency can be calculated as:

$$\epsilon_{pre sel} = \frac{P_o + P_s}{P_o + P_s + F_o - F_s} \quad (4.1)$$

with uncertainty calculated as :

$$\delta\epsilon_{pre sel} = \sqrt{\frac{(F\delta P)^2 + (P\delta F)^2}{(F + P)^4}} \quad (4.2)$$

where $P=P_o+P_s$, $F=F_o-F_s$, $\delta P=\sqrt{P_o + P_s}$, $\delta F=\sqrt{F_o + F_s}$.

The numbers of events with an invariant mass between 65 and 115 GeV/ c^2 are listed in Table 4.1.

region	PO	PS	FO	FS
CC	28074	1110	317	184
EC	7227	535	122	57

Table 4.1: Results of event selection for preselection efficiency measurement

Using these numbers, we can calculate the average preselection efficiency as:

$$\epsilon_{pre sel}^{CC} = (99.6 \pm 0.1)\% \quad (4.3)$$

$$\epsilon_{pre sel}^{EC} = (99.2 \pm 0.1)\% \quad (4.4)$$

We also plot the η_{det} , ϕ_{det} and p_T dependence of the preselection efficiency in Fig. 4.3 and 4.4.

4.2 Spatial Track Matching Efficiency

The spatial track matching efficiency measures how well the tracking system finds the track associated with a real electron.

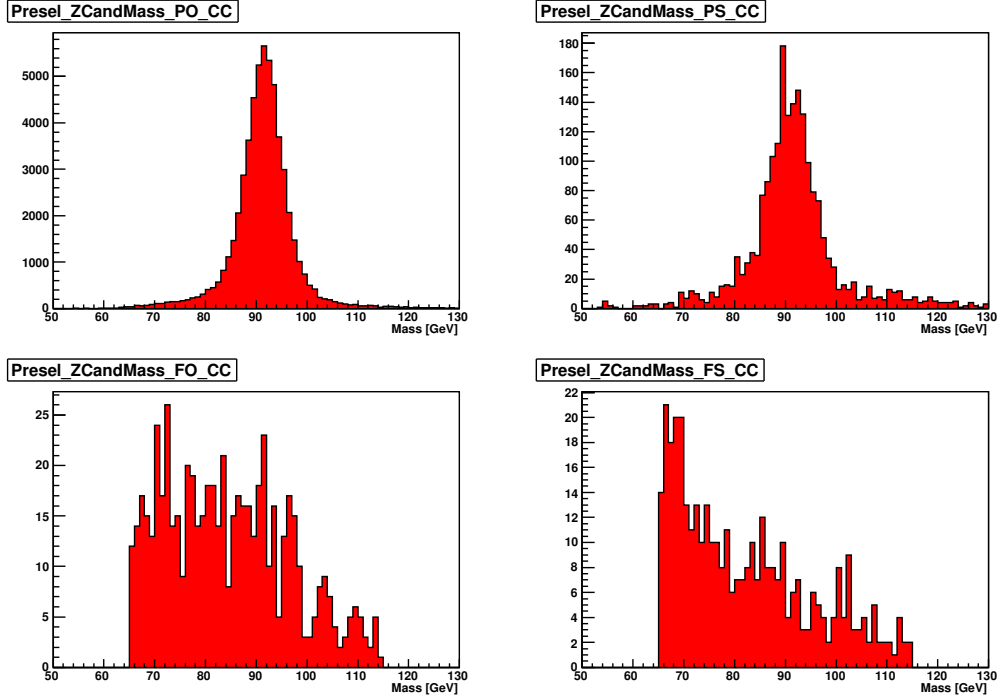


Figure 4.1: Preselection efficiency vs electron detector eta.

The data sample used for measuring the spatial track match efficiency is a skimmed 2EM sample, with two high p_T ($p_T > 15$ GeV/ c) good EM objects (ID=10 or ± 11).

The spatial track matching efficiency is measured using the tag and probe method. A tag is an EM cluster satisfying kinematic, geometric, trigger, preselection, H-matrix and spatial track-match requirements. A probe is an EM cluster passing kinematic, geometric and preselection requirements. The invariant mass of the tag and probe should be between 70 and 110 GeV/ c^2 . Since only one spatial track match is required in the event selection, the QCD background level is big enough that its contribution has to be carefully taken into account. To estimate the background fraction, the Di-EM invariant mass distribution is fitted as a linear sum of the $Z/\gamma^* \rightarrow e^+e^-$ signal predicted using ResBos[49]+PHOTOS[50], which is described in Chapter 5, and the QCD background mass distribution, which is described in Chapter 6.

The average spatial track matching efficiencies in the CC and EC regions are calculated to be:

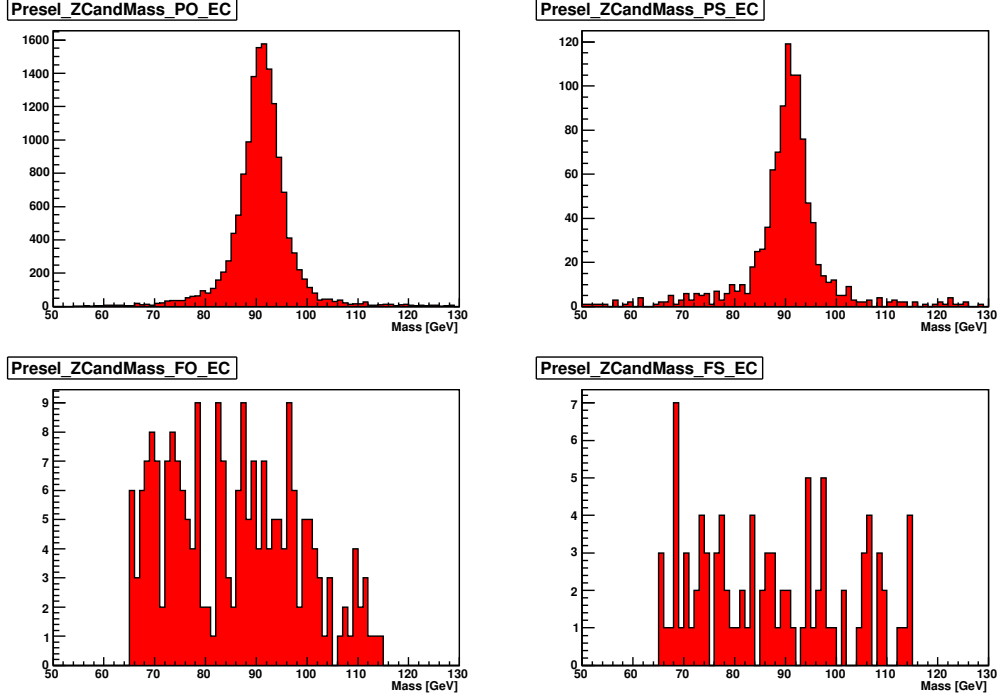


Figure 4.2: Preselection efficiency vs electron detector eta.

$$\epsilon_{trk}^{CC} = (90.5 \pm 0.1)\% \quad (4.5)$$

$$\epsilon_{trk}^{EC} = (61.5 \pm 0.3)\% \quad (4.6)$$

The spatial track matching efficiency is low in the EC region because of the limited coverage of the tracking system in the forward region.

The spatial track matching efficiency strongly depends on the z of the primary vertex. We divide the z vertex distribution into 5 bins: -100 cm to -40 cm, -40 cm to -10 cm, -10 cm to 10 cm, 10 cm to 40 cm and 40 cm to 100 cm. Fig. 4.5 and Fig. 4.6 shows the η_{det} dependence of the spatial track matching efficiency for the five different z vertex bins for CC and EC electrons, respectively, after background subtraction. Background fractions are determined using the invariant mass fitted in each η_{det} bin to take into account the η_{det} dependence of the background fractions. Fig. 4.7 and Fig. 4.8 also shows the electron p_T dependence of the spatial track

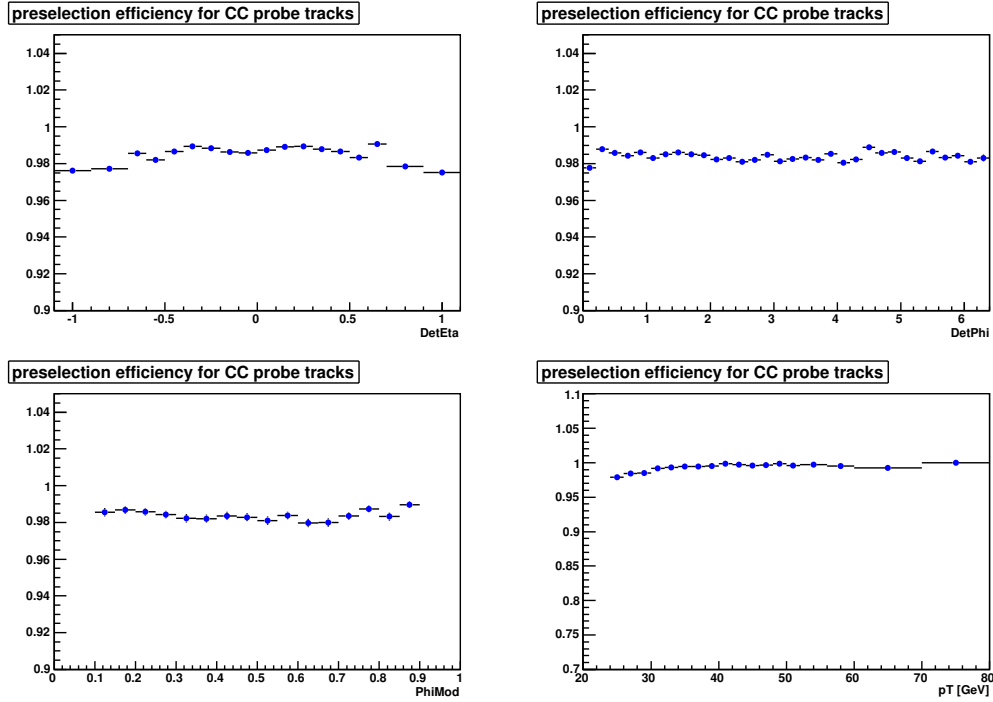


Figure 4.3: Preselection efficiency vs electron detector eta.

matching efficiency for the CC and EC electrons, respectively, after background subtraction.

4.3 Trigger Efficiency

The efficiency for an electron to pass at least one of the triggers is studied using the “tag and probe” method. Due to different trigger definitions, the trigger lists for the dataset are divided into five versions: v8-10, v11, v12, v13 and v14. The data sample used to study trigger efficiency is also the 2EM high p_T skim. The tag electron passes all the single electron selection requirements. The probe is an electron that passes kinematic, geometric, preselection and spatial track match requirements and is checked for the single EM trigger requirements. Table 4.3 shows the number of probes passing the trigger requirements for different trigger lists within an invariant mass window $[70,110] \text{ GeV}/c^2$.

The trigger efficiency has a strong dependence on electron E_T , as is shown in Fig. 4.9. The η_{det} dependence of the trigger efficiency is presented in Fig. 4.10.

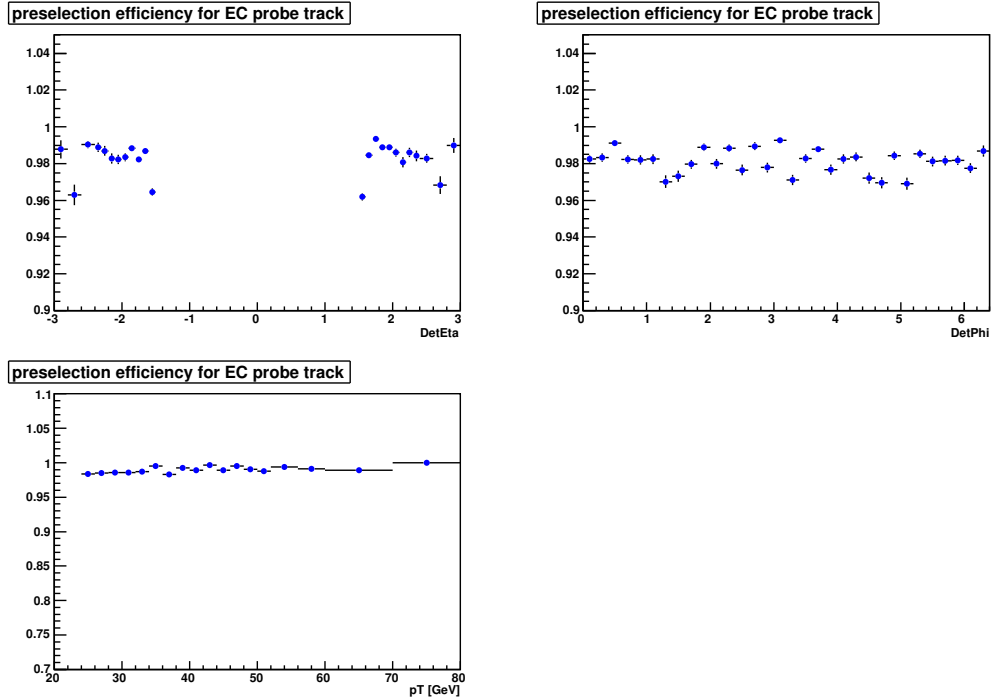


Figure 4.4: Preselection efficiency vs electron detector eta.

4.4 H-Matrix Efficiency

H-matrix measures how well the shape of the EM object measured in the calorimeter agrees with the typical shower shape of an electron, as determined from a GEANT-based Monte Carlo simulation [44]

Based on the effort of the Run II W/Z cross section analysis[41], the optimum cut values are $H\text{-matrix}(7) < 12$ for CC electrons and $H\text{-matrix}(8) < 20$ for EC electrons.

The data sample is the same as was used to evaluate the trigger efficiency. The tag is required to be a good EM cluster satisfying kinematic, geometric, trigger, preselection, H-matrix and spatial track-match requirements. The probe is a good EM cluster passing all these requirements except H-matrix. The number of CC probes with the invariant mass of the tag and the probe between 70 and 110 GeV/c^2 before and after the $H\text{-matrix}(7)$ requirement are 65076 and 63203, respectively, yielding an average efficiency $(97.1 \pm 0.1)\%$. The number of EC probes with the invariant mass of the tag and the probe between 70 and 110 GeV/c^2 before and after the $H\text{-matrix}(8)$ requirement

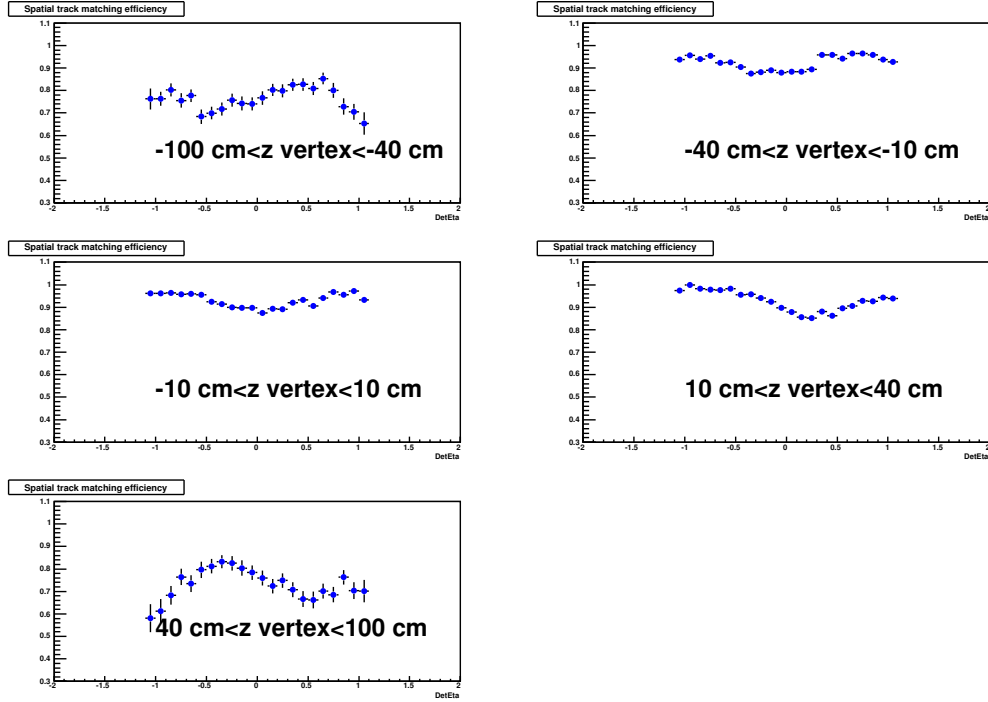


Figure 4.5: Spatial Track Matching efficiency vs CC electron η_{det} .

are 23877 and 23129, respectively, yielding an average efficiency $(96.9 \pm 0.1)\%$.

The η_{det} , p_T and ϕ_{det} dependences of the H-matrix efficiency are shown in Fig. 4.4 and 4.4, for CC and EC electrons, respectively.

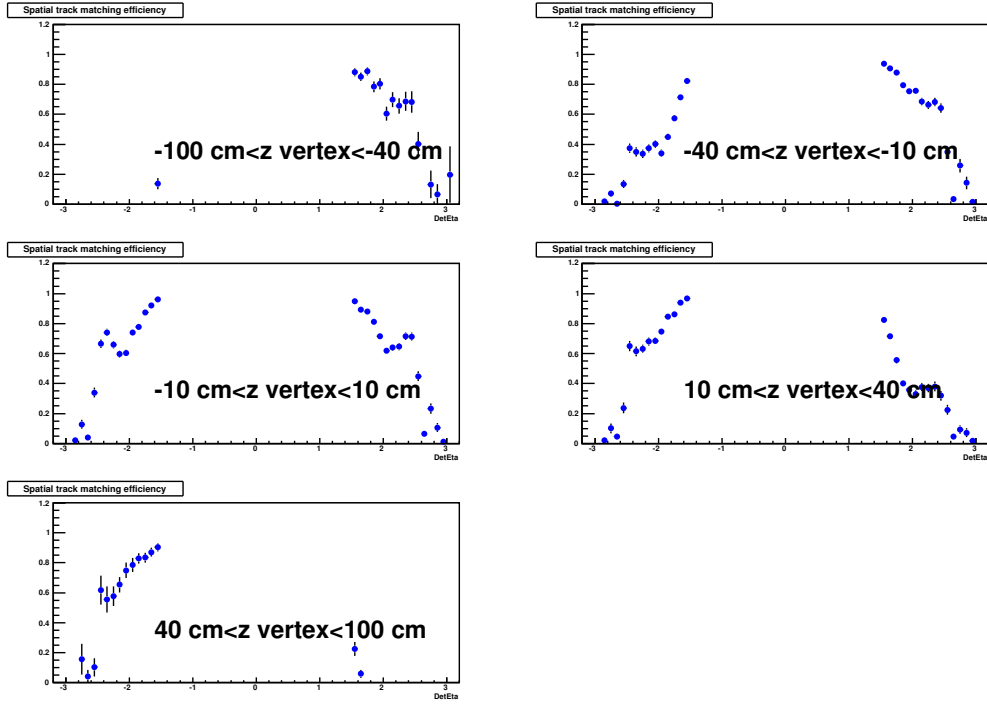


Figure 4.6: Spatial Track Matching efficiency vs EC electron η_{det} .

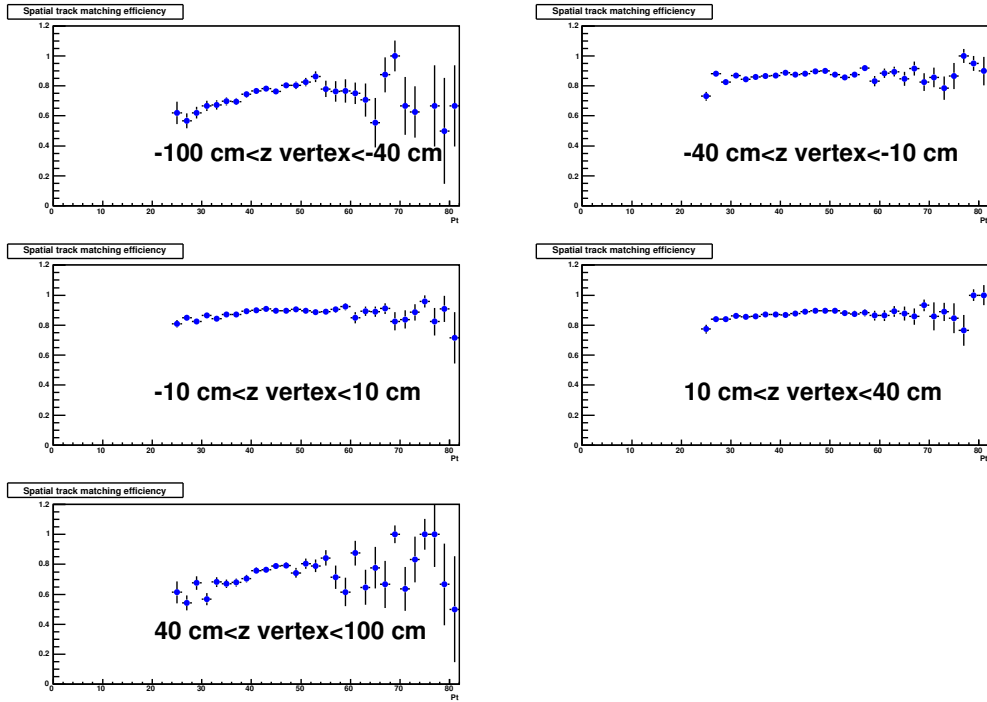


Figure 4.7: Spatial Track Matching efficiency vs CC electron p_T .

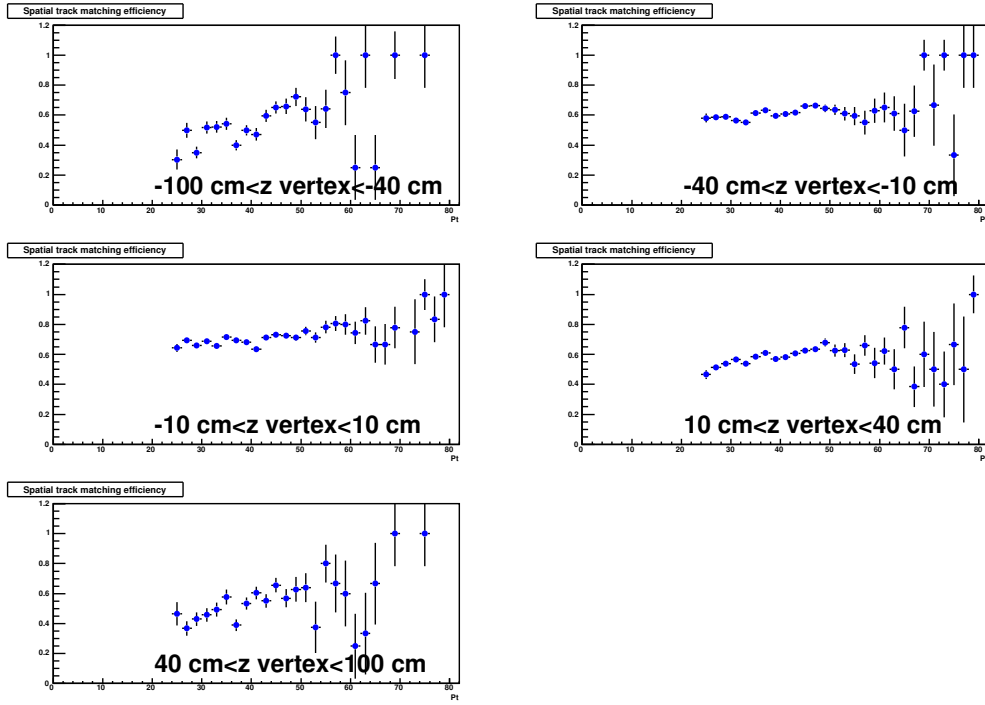


Figure 4.8: Spatial Track Matching efficiency vs EC electron p_T .

	v8-10	v11	v12	v13	v14
before	6160	9439	89250	123794	144690
after	5951	9255	86768	122513	142512
Efficiency	$(96.6 \pm 0.2)\%$	$(98.1 \pm 0.2)\%$	$(97.2 \pm 0.1)\%$	$(99.0 \pm 0.1)\%$	$(98.5 \pm 0.1)\%$

Table 4.2: Trigger efficiency for different trigger lists

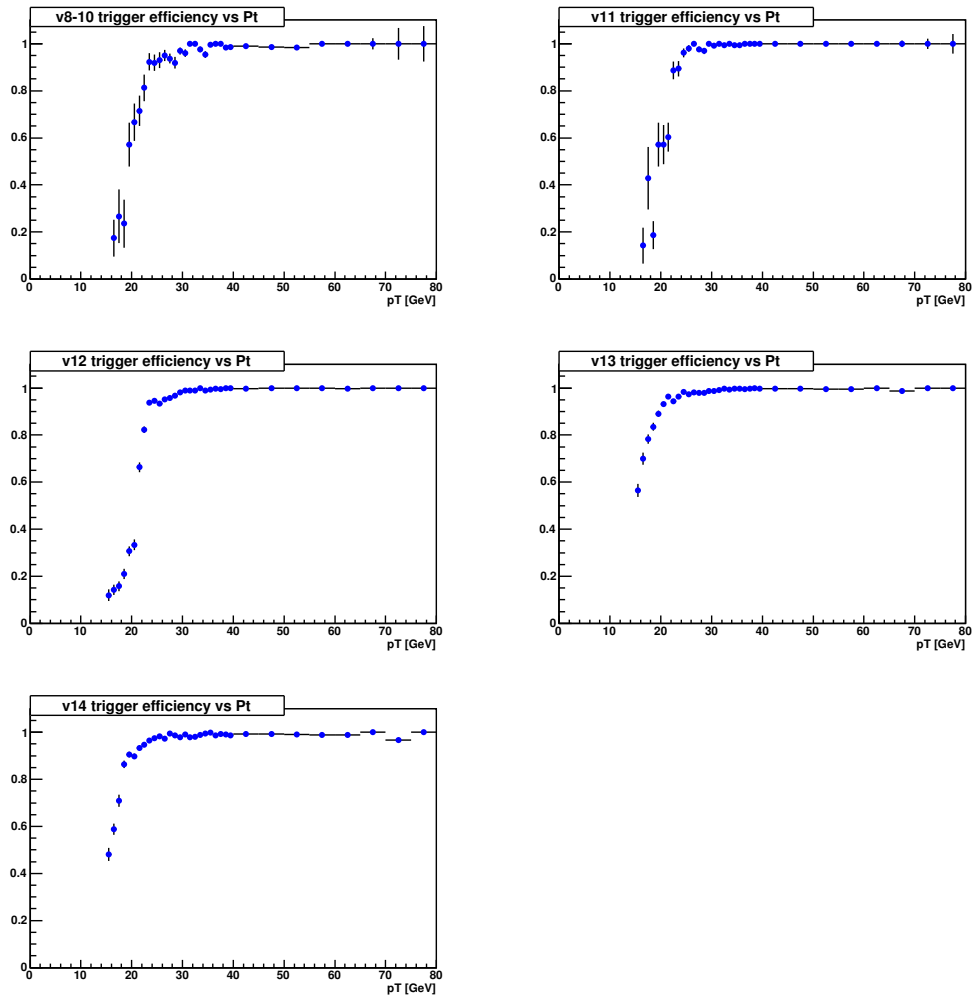


Figure 4.9: Trigger efficiency vs electron p_T .

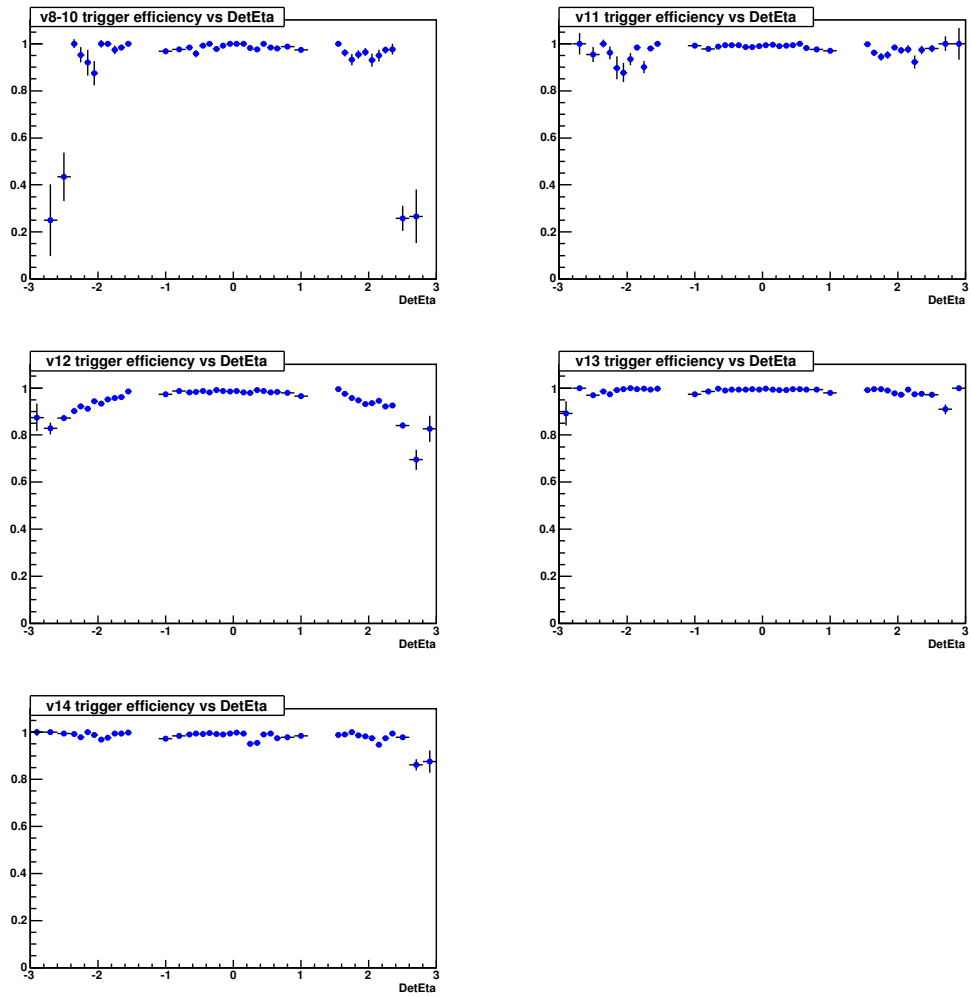


Figure 4.10: Trigger efficiency vs electron η_{det} .

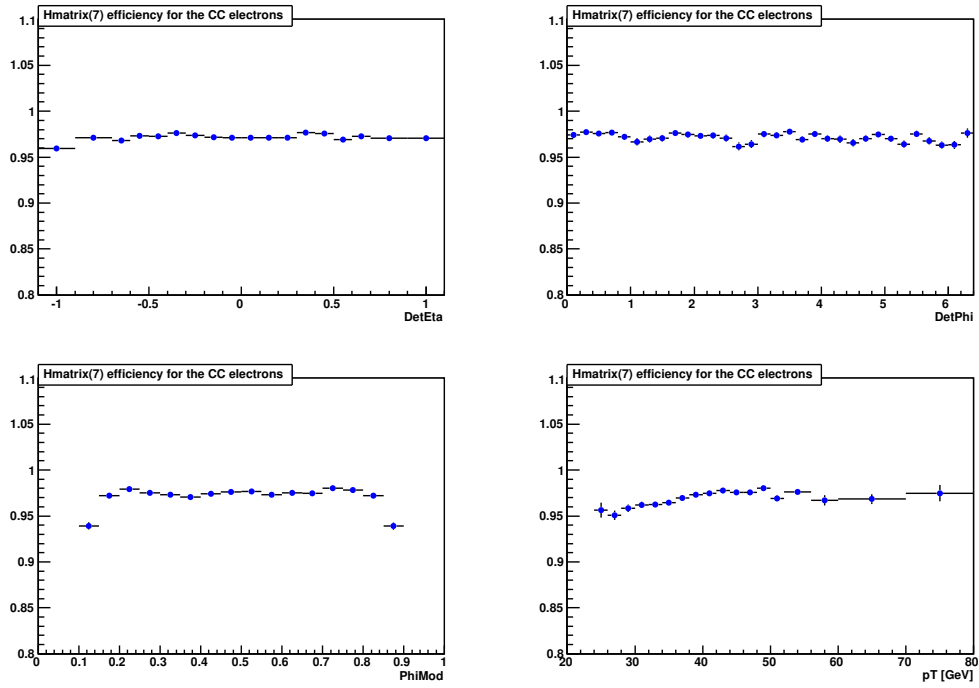


Figure 4.11: H-matrix efficiency as a function of detector η , detector ϕ , phimod, p_T of CC electron

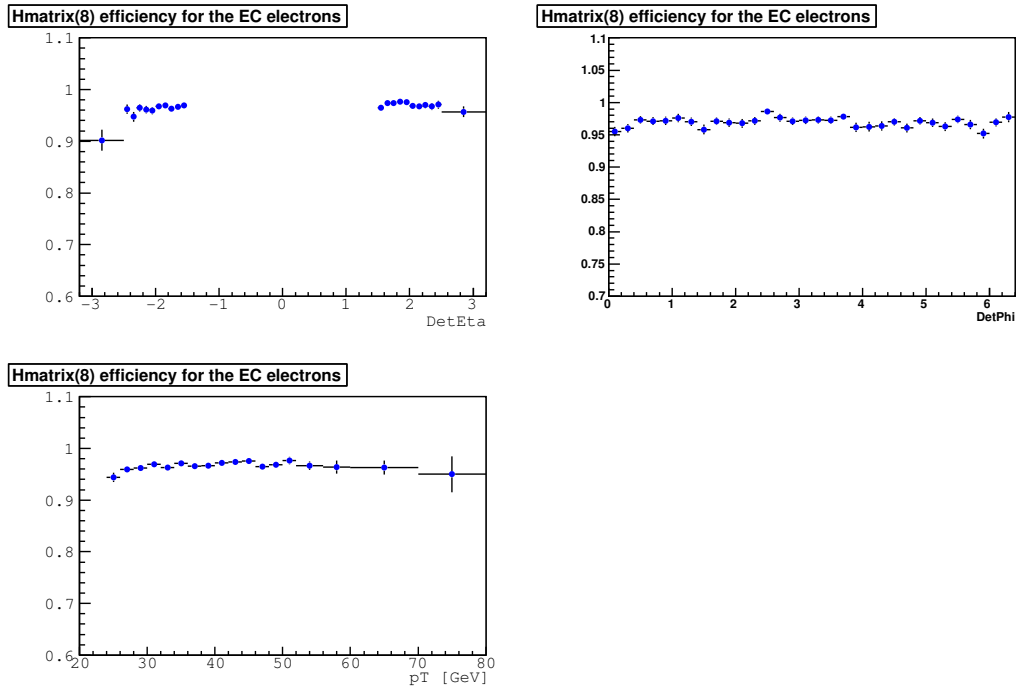


Figure 4.12: H-matrix efficiency as a function of detector η , detector ϕ , phimod, p_T of EC electron

Chapter 5

Monte Carlo Simulation

Monte Carlo simulation is used to understand the effect detector resolutions have on our measured Z p_T spectrum. The measured spectra must be corrected for this smearing, or "unfolded", before it can be compared with the theoretical calculations. The effect of resolutions on the shape of the mass distribution is also needed to estimate the size of backgrounds containing fake electrons in our data sample. We also use Monte Carlo simulations to predict the size of backgrounds containing two real high p_T , isolation electrons from, for example, WW production, $t\bar{t}$ production, and other such interactions.

The $D\bar{O}$ full detector simulation[47] contains two consecutive programs: $D\bar{O}gstar$ and $D\bar{O}Sim$. $D\bar{O}gstar$ ($D\bar{O}$ GEANT Simulation of the Total Apparatus Response) is a GEANT-based simulation of the Run II $D\bar{O}$ detector. What it does is to track the motion of, and simulate the detector response to, particles, determine how much energy is deposited in the active areas of the detector. $D\bar{O}Sim$ is a multi-purpose program which simulates the response of the detector electronics to the hits provided by $D\bar{O}gstar$ and also simulates the pile-up¹ and the minimum bias interactions² that occur in the same crossing as the signal event.

In this analysis, to understand the detector smearing effect, we do not use the $D\bar{O}$ full Monte Carlo simulation (we only use it to determine the Z p_T dependence of the efficiency, as is described in Chapter 7.); instead we use our own parameterized detector simulation, which is much faster and is suitable for our analysis.

¹Pile-up occurs when the readout of a particle detector includes information from more than one primary beam particle interaction - these multiple interactions are said to be "piling-up". The average number of interactions created in a bunch crossing scales linearly with instantaneous luminosity.

²Normally the detector simulation does not include effects from the uranium noise, accelerator conditions causing multiple interactions nor the pile-up. These three effects are modeled by zero-bias events. A minimum bias event is a zero-bias event with the additional requirement of a coincidence signal in the scintillating tile hodoscopes[48]. This additional requirement indicate an inelastic collision during the bunch crossing.

5.1 Physics Generator

We use ResBos[49] and PHOTOS[50] together as the $p\bar{p} \rightarrow Z/\gamma^* \rightarrow e^+e^-$ event generator.

ResBos is a Monte Carlo for *Resummed Boson* production and decay. It is used to compute the differential cross section $\frac{d^2\sigma}{dp_T dy}$ for processes $p\bar{p} \rightarrow B(\rightarrow l_1 l_2)$ with soft-gluon resummed initial state QCD corrections included. Here B is a boson ($W^\pm, Z, \gamma^* \dots$) and l_1, l_2 are leptons. PHOTOS is a Monte Carlo program for QED single-photon radiative corrections in decays, and is run on the output of ResBos to simulate the final state photon radiations. The resummation calculation fails at large p_T , as large terms are missing from the calculation because of its $p_T \rightarrow 0$ approximation. Instead, ResBos uses a fixed order perturbative calculation (NLO) to describe the high- p_T region.

5.2 Parameterized Monte Carlo Simulation

After the generator generates $Z/\gamma^* \rightarrow e^+e^-$ events, electrons (photons) are extrapolated from the primary vertex to the third layer of the EM calorimeter. Because of finite detector segmentation, photons which are nearly co-linear with the electrons will be merged into the electrons during reconstruction. We simulation this effect in the fast simulation by merging the generator-level photons with the nearest electron if the distance between the electron and the photon is small. For the CC calorimeter, they are merged if $R(=\sqrt{\Delta\phi^2 + \Delta\eta^2})$ is less than 0.2. In EC region, the cone is defined by a radius of 10 cm of the electron at the 3rd layer of the EM calorimeter. These cut values are consistent with the values used in the full reconstruction code DØRECO.

We use a parameterized Monte Carlo simulation (PMCS) [51] to simulate the effect of the detector response and resolution (smearing).

5.2.1 Energy Scale

In an ideal detector, the measured electron energy would be linear in the true electron energy with a slope of 1 and an intercept of 0. However, because of the effects of non-linearities in the electronics, and because of pileup from the underlying event and pile-up events, while the

relationship is approximately linear, the slope and intercept can differ from their ideal values. To simulate these effects in PMCS, the energy of the generator electron is first scaled by the measured EM energy scale.

$$E' = \alpha \times E_{gen} + \beta \quad (5.1)$$

where α is the EM energy scale and β is the EM energy offset. α and β are determined by comparing the invariant mass peak from the $Z/\gamma^* \rightarrow e^+e^-$ Monte Carlo to that of the $Z/\gamma^* \rightarrow e^+e^-$ data. The method used is a binned-log-likelihood method[52].

The invariant mass distribution is binned for the Monte Carlo and data from 70 to 110 GeV/ c^2 , and then a binned likelihood function is calculated:

$$L = - \sum_i [x_i \times \ln(y_i) - y_i - \ln(x_i!)] \quad (5.2)$$

where x_i is the number of data points in bin i and y_i is the number of the Monte Carlo events in bin i . The other smearing parameters are fixed to some reasonable values and only the electron energy scale α (or energy offset β) is varied. For each value of α (or β), L is evaluated. To determine a minimum value we then fit L to a quadratic function. First CC-CC events are used to obtain the CC energy scale and energy offset. Then the EC energy scales and energy offsets are obtained from the CC-EC data, fixing the CC energy scale and offset to the values obtained from the CC-CC sample. An example of the fitting is shown in Fig. 5.1 for the negative endcap calorimeter region. The tuned energy scale and energy offset values for central and endcap calorimeters are included in Table 5.2.5.

5.2.2 Energy Resolution

In PMCS, after the scale is applied, the electron energy are then smeared according to the measured energy resolution. A typical empirical parameterization of the energy resolution of a calorimeter in a particle physics experiment is :

$$\frac{\sigma_{EM}(E')}{E'} = \sqrt{C_{EM}^2 + \frac{S_{EM}^2}{E'} + \frac{N_{EM}^2}{E'^2}} \quad (5.3)$$

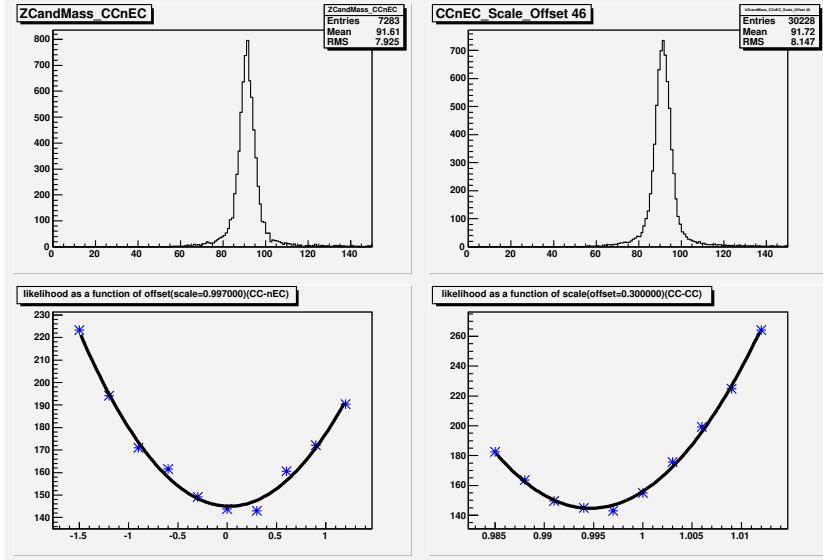


Figure 5.1: Tuning of energy scale and offset for negative endcap region. The top left plot is the invmass peak for data sample, the top right plot is the invmass peak for Monte Carlo sample. The bottom two plots are the tuning of energy offset and scale, respectively.

where C_{EM} is the constant term, which results from non-uniformity in the detector response, S_{EM} is the sampling term and is due to sampling fluctuations, and N_{EM} is the noise term due to the “noise” from the uranium decays, readout electronics noise, the underlying event, and pile-up events.

The smeared electron energy is then

$$E_{smeared} = E' + x * \sigma_{EM}(E') \quad (5.4)$$

where x is a random variable from a normal Gaussian distribution with zero mean and unit width.

The constant term and noise term can be different in each DØ calorimeter, but should not depend on the position within the calorimeter. The sampling term has a dependence on the position and angle of impact of the incident electron. In DØ Run I the sampling term had a weak position dependence of the form $1/\sqrt{(\sin(\theta))}$.

As found in a study by Jan Stark using a GEANT-based Monte Carlo simulation[53], for the upgraded Run II detector, in the CC region, the sampling term of the energy resolution no longer

scales as $1/\sqrt{\sin(\theta)}$. The reason for that is: in DØ Run II, materials are added in front of the calorimeter. This causes the sampling term to vary dramatically with the position and angle of the incident electron. To evaluate this effect, Dr. Stark generated single energy electrons(45 GeV) and passed them through the DØ full Monte Carlo simulation. He fitted the reconstructed energy spectrum with a Gaussian to extract the energy resolution as a function of the energy and position of the electrons. The results show a strong dependence on η_{phy} , as shown in Fig. 5.2. This η_{phy} dependence of the energy resolution can then be fitted to the following function:

$$\sigma_E/E = p_0/\exp(p_1) \times \exp(p_1/\sin(\theta)) \quad (5.5)$$

where p_0 and p_1 correspond to resolution term at normal incidence and angle respectively. By repeating the same steps with different electron energies(from 5 to 400 GeV) and he was able to get the energy dependence of p_0 and p_1 , as presented in Fig. 5.3 and Fig. 5.4. They were fitted to the following forms:

$$p_0 = 16.4\%/\sqrt{E} + 12.2\%/E \quad (5.6)$$

$$p_1 = 1.35193 - 2.09564/E - 6.98578/(E \times E) \quad (5.7)$$

Since, in the GEANT-based Monte Carlo simulation, the detector is uniform and the noise is small, the constant and noise terms are close to zero, the energy resolution dependence determined above gives only the sampling term of the energy resolution.

The final form of the energy resolution in CC region is:

$$\frac{\sigma_{EM}(E')}{E'} = \sqrt{C_{EM}^2 + \frac{N_{EM}^2}{E'^2} + (p_0 \times \exp(\sin(\theta)))/\exp(p_1)}^2 \quad (5.8)$$

Using the same idea, in the EC region, we assume the sampling term is also a function of both η_{phy} and energy of the incident electron. Fig. 5.5 shows the detector setup in the GEANT simulation for the endcap calorimeter and materials in front of it. Fig. 5.6 shows the number of

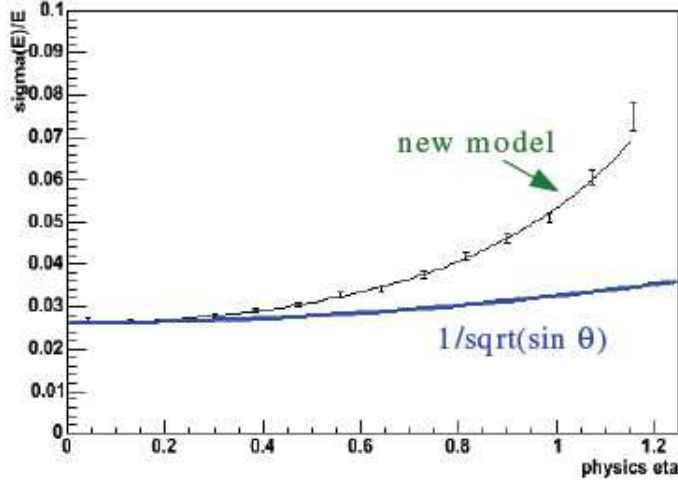


Figure 5.2: Sampling term η_{phys} dependence for central calorimeter.

radiation length of the materials in front of the endcap calorimeter as a function of η_{phys} and we do see a strong dependence.

By generating different energy electrons and injecting them into the detector from different angles, we can determine the energy resolution as a function of the electron's energy and η_{phy} :

$$\sigma_E/E = p \times (s_0/\sqrt{E} + s_1/E)/(s_0/\sqrt{45} + s_1/45.) \quad (5.9)$$

where p is the η_{phy} dependence and $(s_0/\sqrt{E} + s_1/E)/(s_0/\sqrt{45} + s_1/45.)$ parameterizes the electron energy dependence. Parameters s_0 and s_1 are also functions of η_{phy} .

To determine the η_{phy} dependence p , we generated 45 GeV single electron samples at different angles and put them through the full Monte Carlo simulation. We then plotted σ_E/E for each angle to get p .

Fig. 5.7 and 5.8 show p 's distribution for both positive and negative endcap calorimeter regions.

They can be parameterized as:

$$p = 14.808 - 53.358\eta + 80.874\eta^2 - 66.687\eta^3 + 32.331\eta^4 - 9.222\eta^5 + 1.434\eta^6 - 0.094\eta^7 (PositiveEC) \quad (5.10)$$

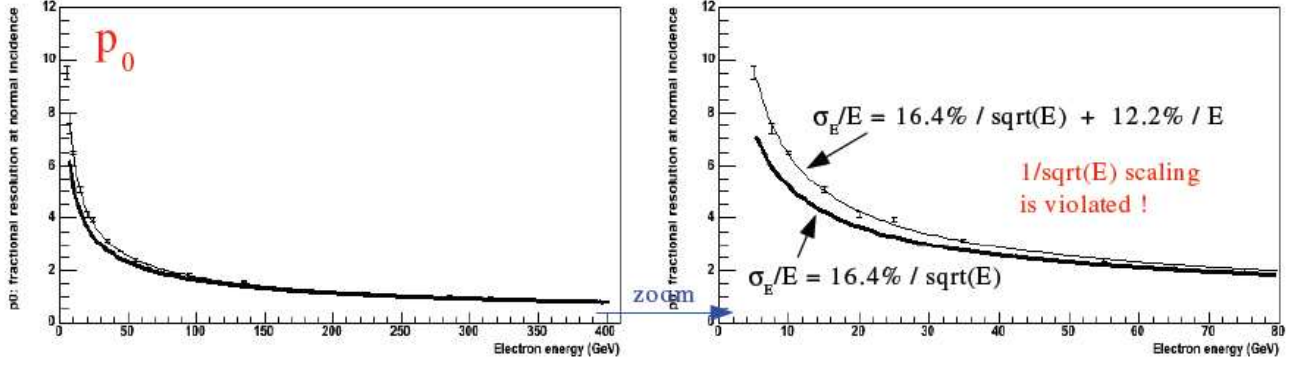


Figure 5.3: p_0 dependence for central calorimeter.

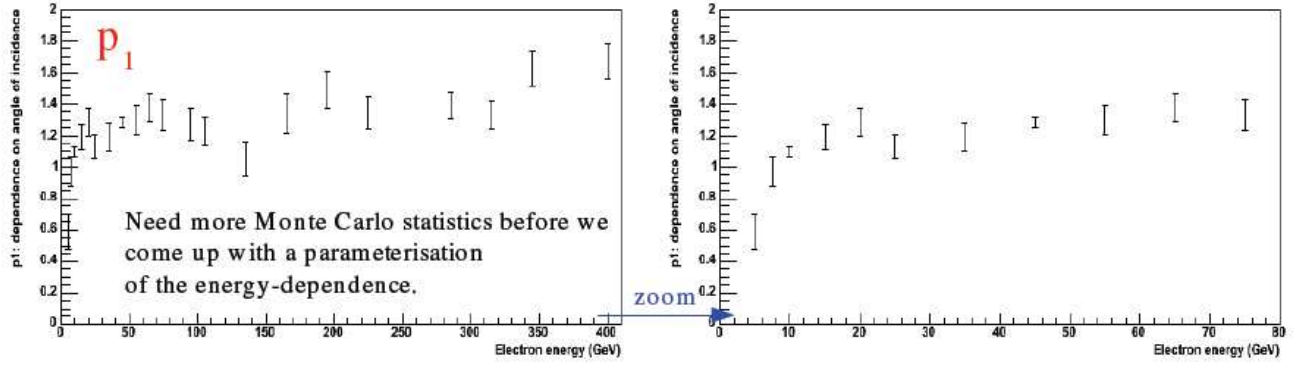


Figure 5.4: p_1 dependence for central calorimeter.

$$p = -9.507 + 27.044(-\eta) - 31.337\eta^2 + 19.008(-\eta^3) - 6.364\eta^4 + 1.115(-\eta^5) - 0.080\eta^6 \text{ (Negative EC)} \quad (5.11)$$

For the electron energy dependence, we generated single electron samples with different energies and a fixed η_{phy} . Then we plotted σ_E/E as the function of the energy and fit it to $(s_0/\sqrt{E} + s_1/E)$, with s_0 and s_1 as free parameters. We repeated the same steps at different η_{phy} s to get the η_{phy} dependence of s_0 and s_1 . Fig. 5.9 and Fig. 5.11 show the s_0 and s_1 for positive endcap calorimeter. Fig. 5.10 and Fig. 5.12 show the s_0 and s_1 for negative endcap calorimeter. The parameterizations of s_0 and s_1 are:

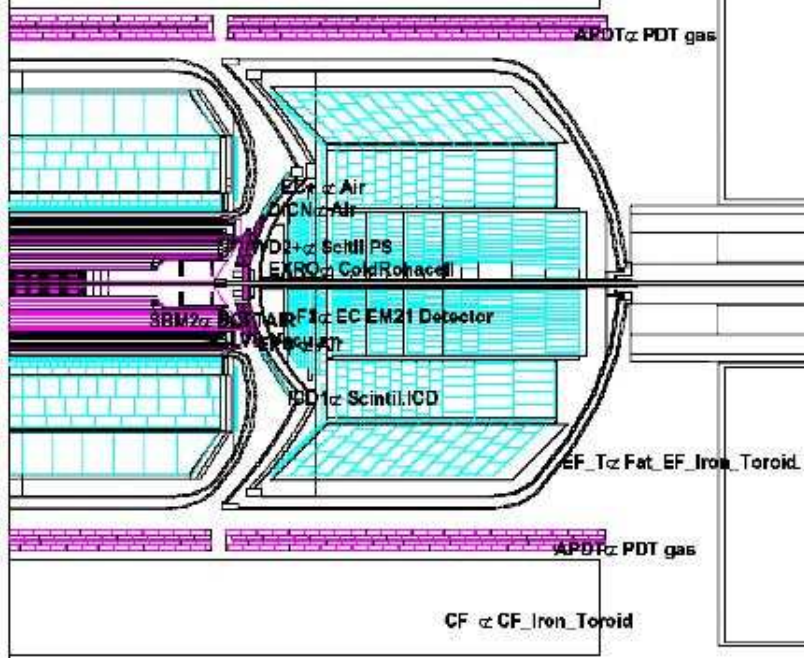


Figure 5.5: Detector setup in the GEANT simulation of the Endcap Calorimeter and the materials in front of it.

$$s_0 = 0.217 + 0.003\eta - 0.007\eta^2 \quad (PositiveEC) \quad (5.12)$$

$$s_0 = 0.221 - 0.025(-\eta) + 0.002\eta^2 \quad (NegativeEC) \quad (5.13)$$

$$s_1 = 57.247 - 104.577\eta + 71.148\eta^2 - 21.127\eta^3 + 2.306\eta^4 \quad (PositiveEC) \quad (5.14)$$

$$s_1 = 9.479 - 21.201(-\eta) + 17.503\eta^2 - 6.027(-\eta^3) + 0.734\eta^4; \quad (NegativeEC) \quad (5.15)$$

Finally the $(s_0/\sqrt{45} + s_1/45)$ term is used for normalization purpose.

After the sampling term is determined and put into the parameterized Monte Carlo, I then tune the constant term C_{EM} to $Z/\gamma^* \rightarrow e^+e^-$ data using the binned-log-likelihood method. This time, only the constant term is varied and again the Monte Carlo and data invariant mass peaks are compared to find the best constant term value. As with the energy scale, we first determine

the CC constant term using CC-CC events and then determine the EC constant terms using CC-EC events.

The details of determining the noise term from $W \rightarrow e\nu$ events is described in [54]. The energy flow in a 1×5 slice in η - ϕ tower-space is measured as a function of the ϕ separation from the electron cluster centroid, as is shown in Fig. 5.13. For ϕ differences between 0.2 and 0.4, the energies are considered from the underlying events; their distribution is shown in Fig. 5.14. As can be seen in this plot, the average energy per tower is roughly 10 MeV. Assuming the r.m.s. of the energy per tower is σ , and since the r.m.s. shown in this plot (0.04 GeV) = $\sqrt{5} \times \sigma/5$, we find $\sigma = 0.09$ GeV for each tower. There are 13 towers for each EM cluster, so the r.m.s. of the energies below electron window is : $0.09 \times \sqrt{(13)} \sim 0.3$ GeV. Similarly the noise term for EC is determined to be ~ 0.125 GeV.

5.2.3 Position Resolutions

The calorimeter position resolution is modeled using two parameters:

$$\eta_{smear}^{det} = \eta_{gen}^{det} + y * \sigma_{\eta^{det}} \quad (5.16)$$

$$\phi_{smear}^{det} = \phi_{gen} + z * \sigma_{\phi^{det}} \quad (5.17)$$

where $\sigma_{\eta^{det}}$ and $\sigma_{\phi^{det}}$ are the detector η and ϕ resolution, and y and z are two random variables from a normal Gaussian distribution with zero mean and unit width.

The methods of measuring the position resolutions from a data sample of electrons passing the preselection requirements are described in [55]. The idea of the method is to treat the track position as the true position of the electron, and measure the difference between the track position and the calorimeter position to extract the resolutions.

5.2.4 Vertex Distribution

The decay vertex of the Z boson has a large variance in the z direction, with a $\sigma \sim 25$ cm. While the x and y components can be determined by the beam spot position of each run, the z component is found using the following algorithm:

- if both electrons have track, the average of the z of the two tracks is defined as the z vertex of the Z boson.
- if only one electron has a track, the z vertex of this track is defined as the z vertex of the Z boson.
- if neither electron has a track, the z vertex of the Z boson is the z of the primary vertex of this event.

Fig. 5.15 shows the z vertex distributions for $Z/\gamma^* \rightarrow e^+e^-$ data.

The vertex resolutions are modeled in the parameterized Monte Carlo.

5.2.5 Parameters

The values of the parameters are summarized in Table 5.2.5.

All efficiencies measured in Chapter 4 are included in the Monte Carlo simulation using the η_{det} , electron p_T and z vertex (for the spatial track match efficiency) dependences.

5.3 Comparison between Data and Monte Carlo

To test the efficacy of our modeling, we make some comparison plots between the data and the parameterized Monte Carlo simulation.

Figures 5.16 to 5.21 show data/Monte Carlo comparison for the Z/γ^* invariant mass, electron p_T , electron η_{det} , electron ϕ_{det} and Z/γ^* rapidity distributions. These plots also include the contribution from the background, which is described in detail in section 6.1. In general, we have found good agreement between the data and the parameterized Monte Carlo simulation. For these plots, the ResBos parameters were set to their default values. These parameters will be re-tuned using the result of this measurement.

parameter	value
EM Energy Scale(CC)	1.0089 ± 0.0003
EM Energy Offset(CC)	-0.101 ± 0.017
EM Energy Scale(ECP)	0.9936 ± 0.0008
EM Energy Offset(ECP)	-0.290 ± 0.233
EM Energy Scale(ECN)	0.9983 ± 0.0010
EM Energy Offset(ECN)	-0.284 ± 0.123
EM Constant Term(CC)	0.028 ± 0.001
EM Constant Term(ECP)	0.032 ± 0.002
EM Constant Term(ECN)	0.027 ± 0.002
Calorimeter Position Resolution(CC) σ_η	0.0020 ± 0.0002
Calorimeter Position Resolution(CC) σ_ϕ	0.0004 ± 0.0001
Calorimeter Position Resolution(EC) σ_η	0.0029 ± 0.0035
Calorimeter Position Resolution(EC) σ_ϕ	0.0041 ± 0.0034

Table 5.1: Parameters tuned according to data

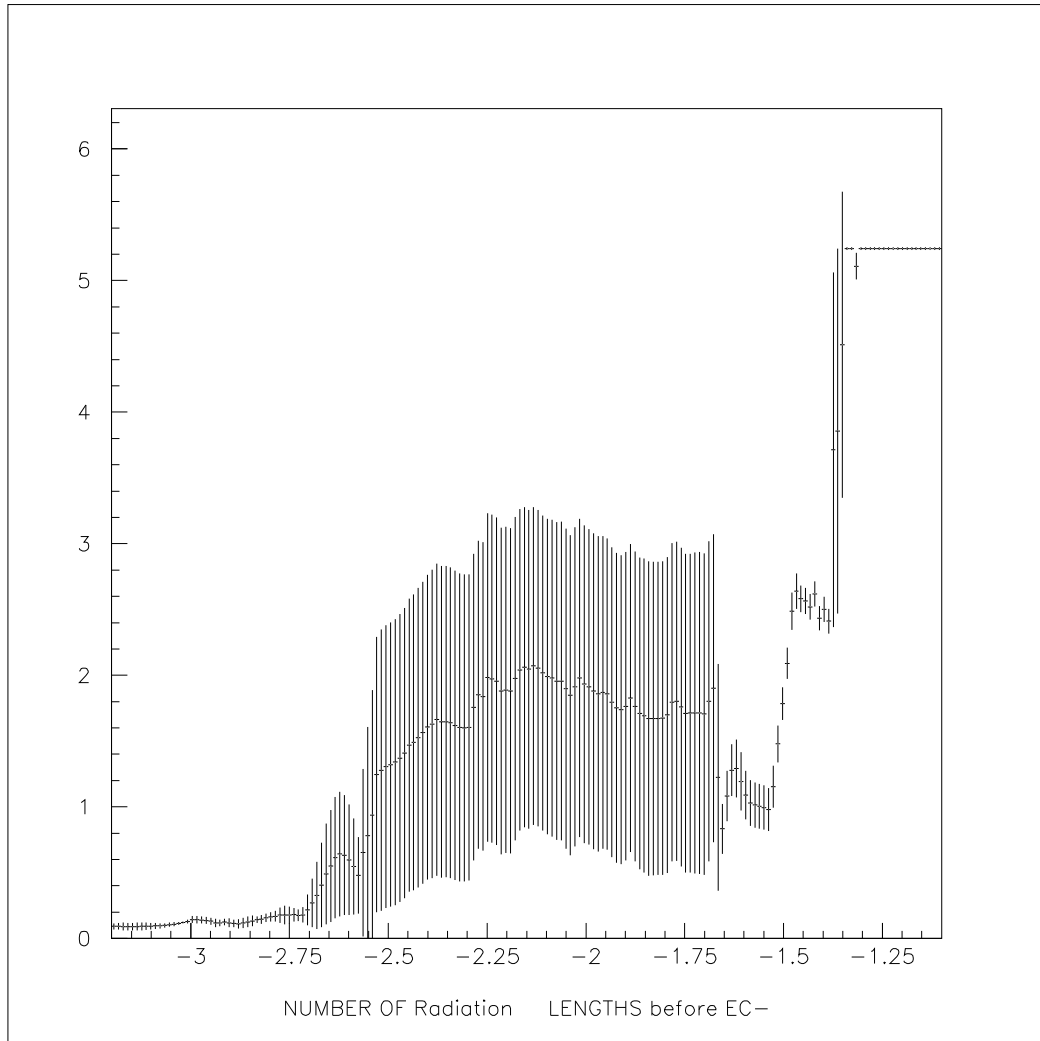


Figure 5.6: Radiation length of the materials in front of the Endcap Calorimeter as a function of η_{phys} . The big error bars between -1.5 and -2.5 of η shows big materials (the Forward Preshower Detector) variations in the ϕ direction.

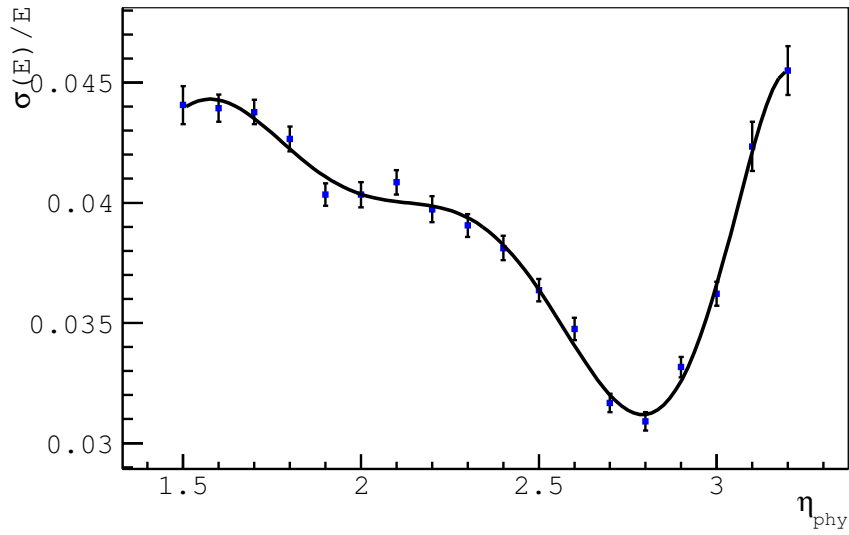


Figure 5.7: Sampling term η_{phys} dependence for positive endcap calorimeter.

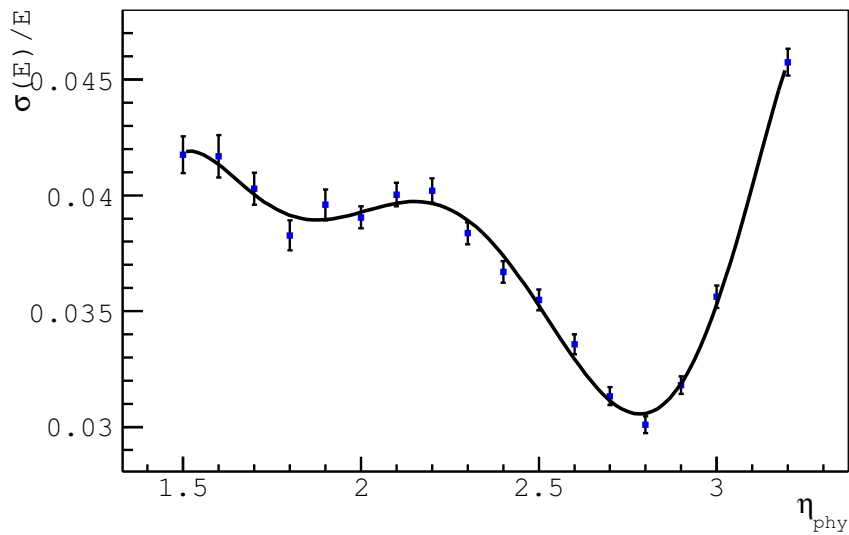


Figure 5.8: Sampling term η_{phys} dependence for negative endcap calorimeter.

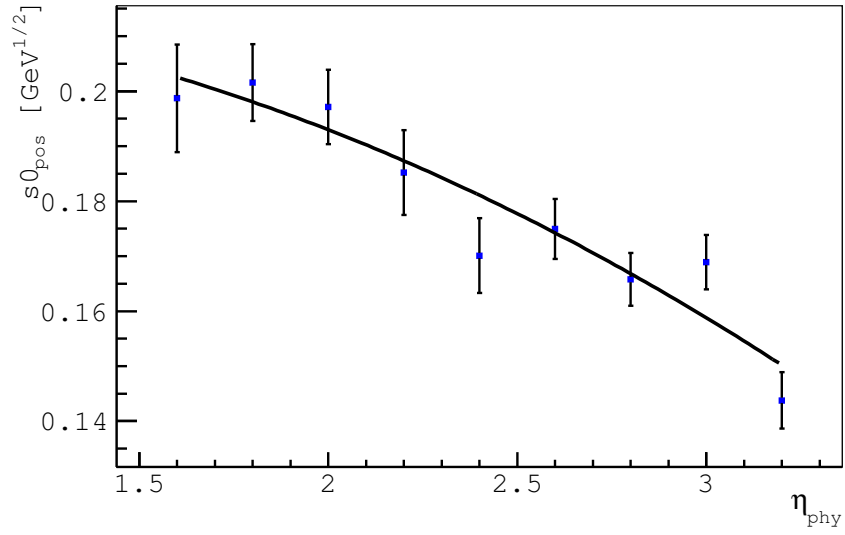


Figure 5.9: η_{phys} dependence of $s0$ for positive endcap calorimeter.

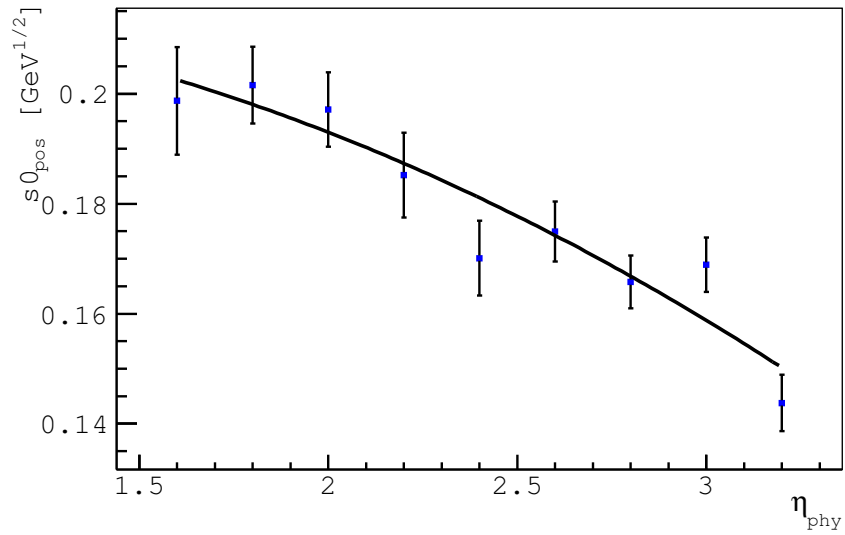


Figure 5.10: η_{phys} dependence of $s0$ for negative endcap calorimeter.

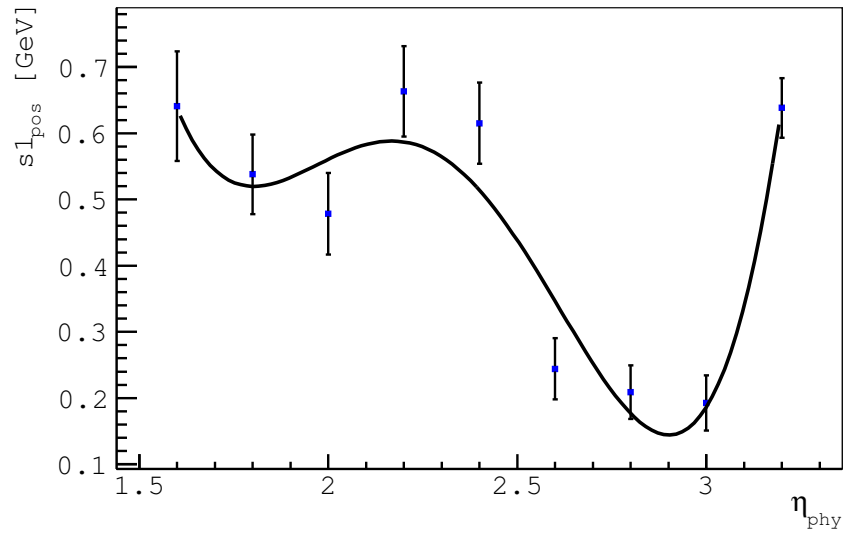


Figure 5.11: η_{phys} dependence of $s1$ for positive endcap calorimeter.

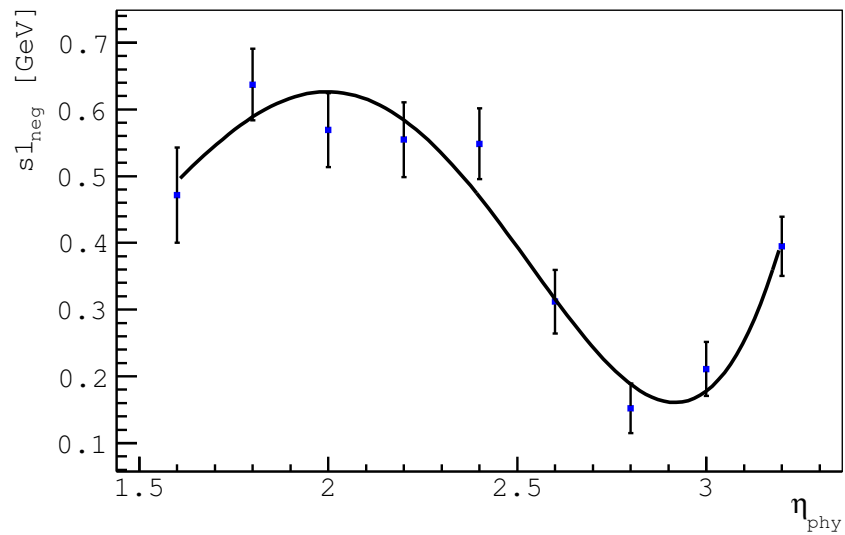


Figure 5.12: η_{phys} dependence of $s1$ for negative endcap calorimeter.

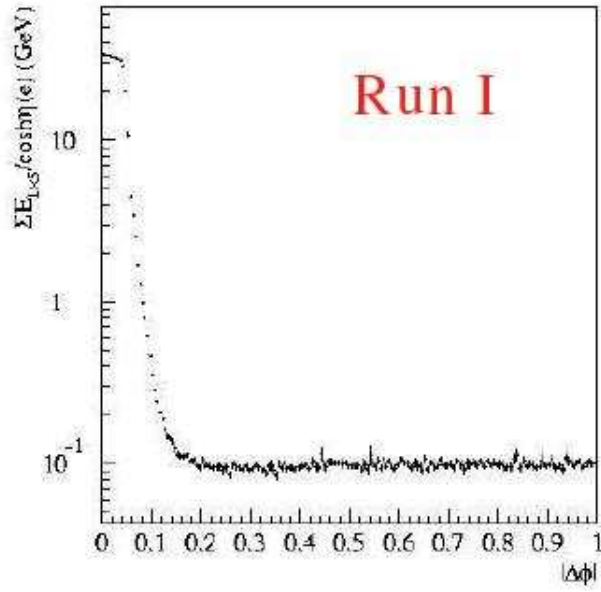


Figure 5.13: The energy flow in a 1×5 slice in η - ϕ tower space as a function of the ϕ separation from the electron cluster centroid

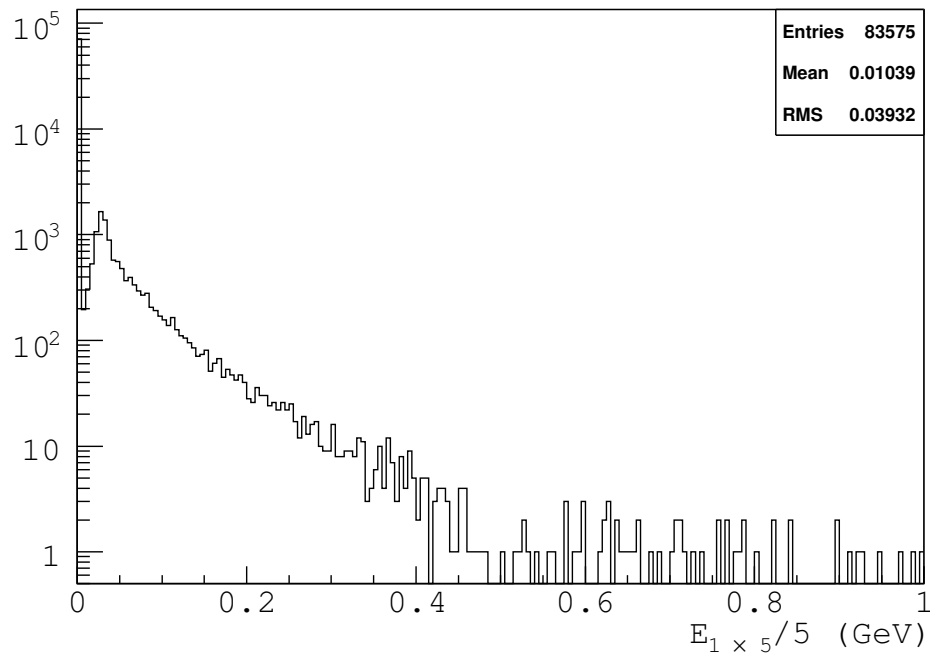


Figure 5.14: Average energy per EM tower for CC electrons from $W^- \rightarrow e\nu$ studies

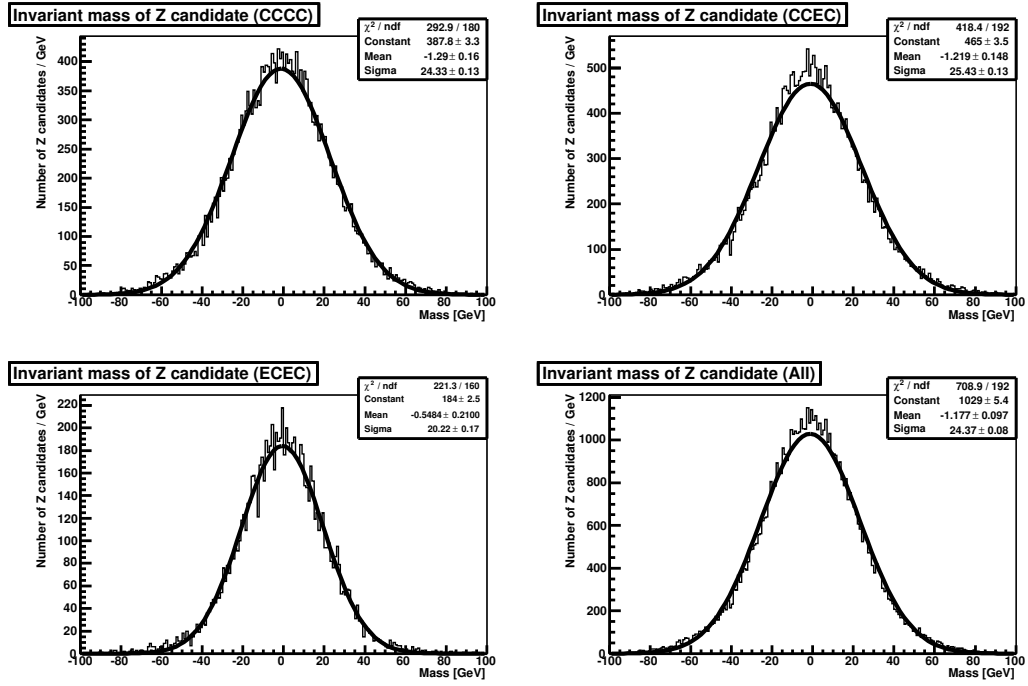


Figure 5.15: Vertex z distribution of the $Z/\gamma^* \rightarrow e^+e^-$ events.

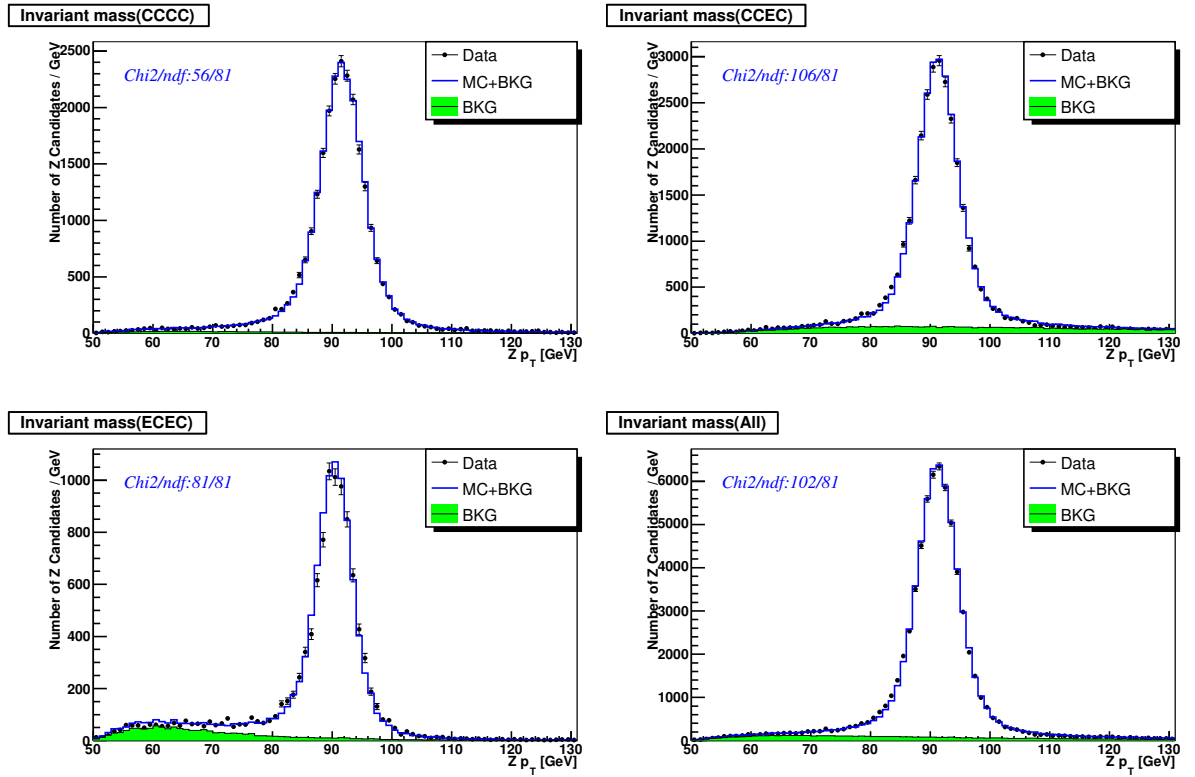


Figure 5.16: Invariant mass distribution for data and Monte Carlo of $Z/\gamma^* \rightarrow e^+e^-$ events

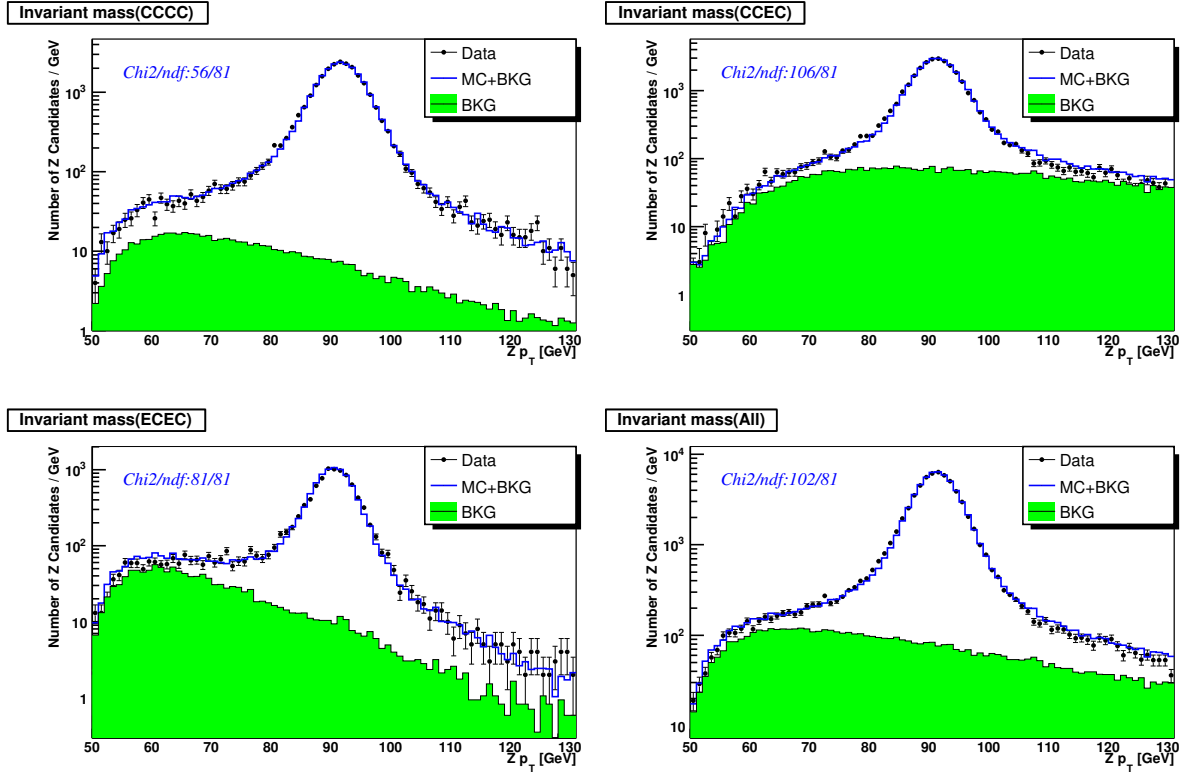


Figure 5.17: Invariant mass distribution for data and Monte Carlo of $Z/\gamma^* \rightarrow e^+e^-$ events

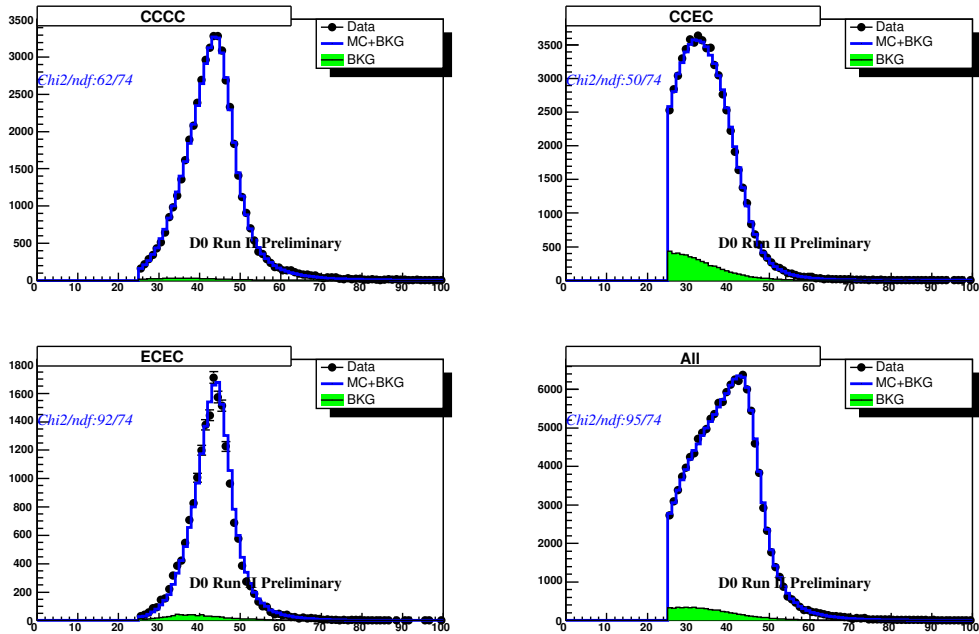


Figure 5.18: Electron p_T distribution for CC-CC, CC-EC, EC-EC, All data and Monte Carlo Z/γ^* events

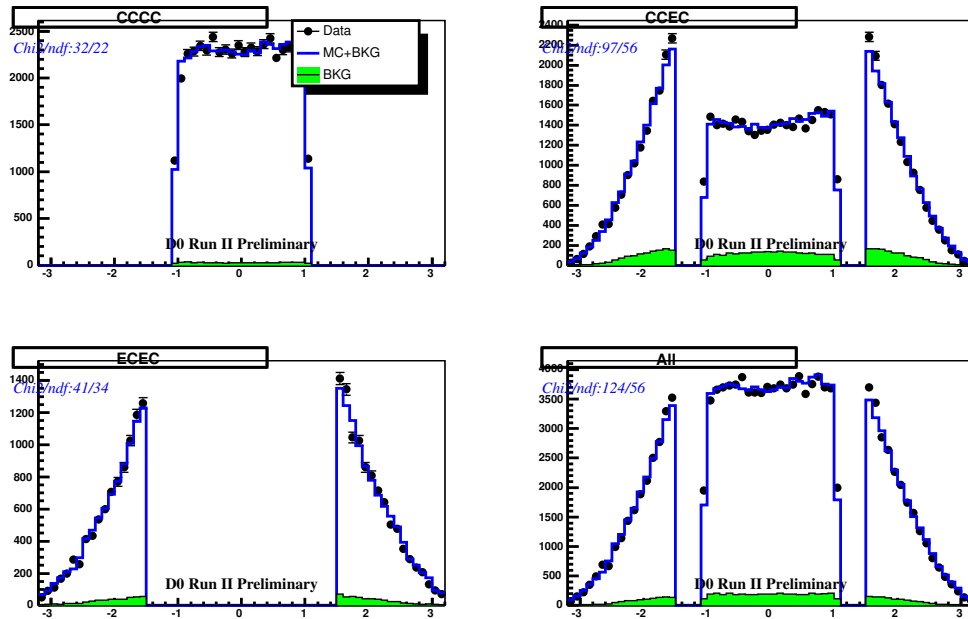


Figure 5.19: Electron η_{det} distribution for CC-CC, CC-EC, EC-EC, All data and Monte Carlo Z/γ^* events

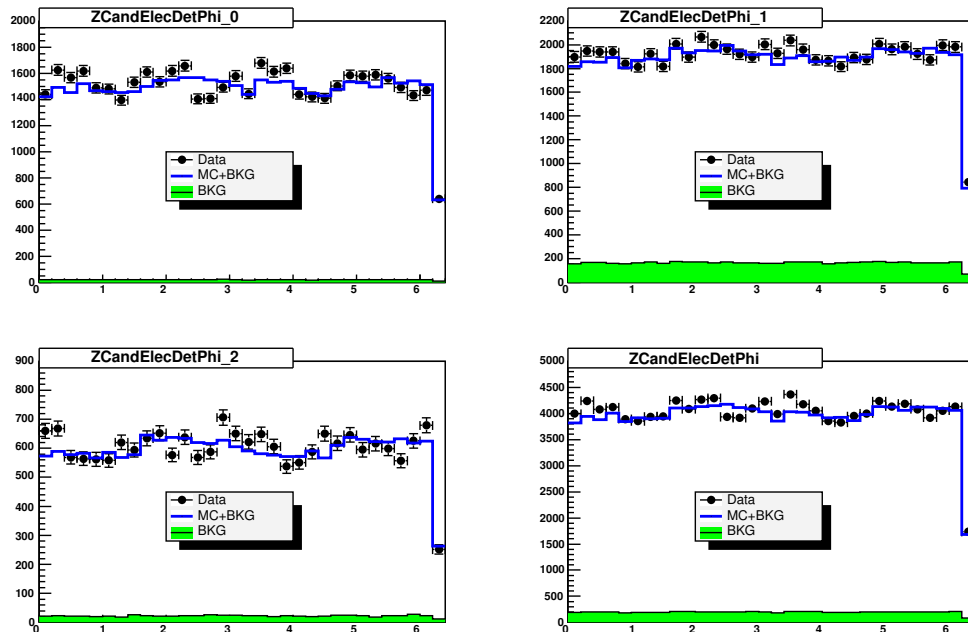


Figure 5.20: Electron ϕ_{det} distribution for CC-CC, CC-EC, EC-EC, All data and Monte Carlo Z/γ^* events

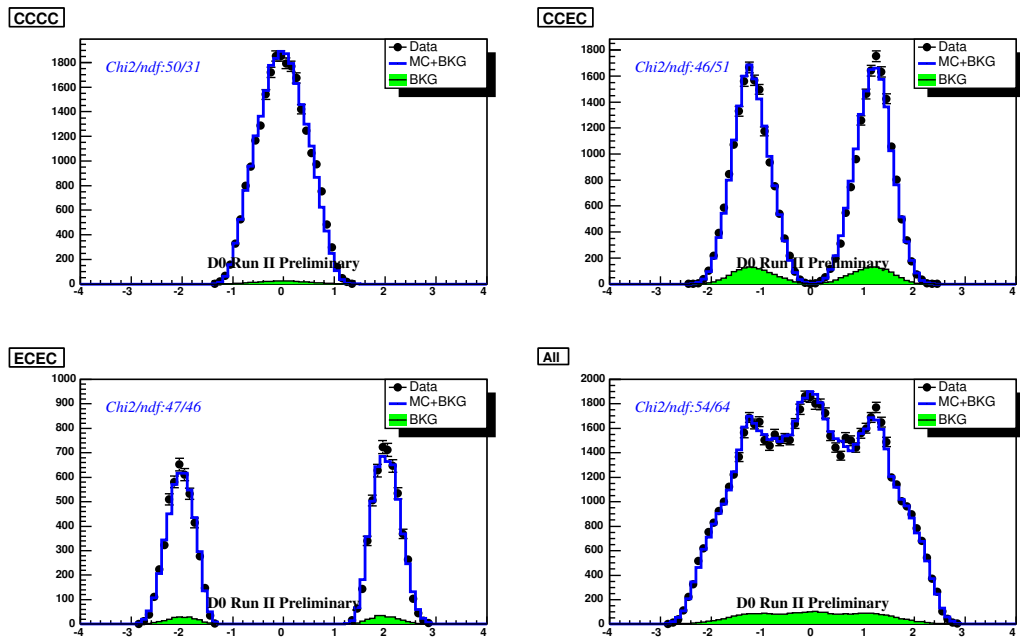


Figure 5.21: Rapidity distribution for CC-CC, CC-EC, EC-EC, All data and Monte Carlo Z/γ^* events

Chapter 6

Backgrounds

For this analysis, the following processes can contribute to background for Z/γ^* signal:

- QCD background where one or two jets fake as electrons.
- events containing a γ recoiling against a jet, with the jet faking an electron
- $Z \rightarrow \tau^+\tau^- \rightarrow e^+e^-\nu_\tau\nu_e\bar{\nu}_\tau\bar{\nu}_e$
- WZ event, where $W \rightarrow$ all and $Z \rightarrow e^+e^-$
- $W^+W^- \rightarrow e^+e^-\nu_e\bar{\nu}_e$ event
- $W\gamma$ where $W \rightarrow e\nu$ and the photon is mis-identified as an electron

6.1 QCD Backgrounds

The QCD backgrounds include di-jet events and EM+jet (direct γ , W +jet) events that contain jet(s) faking electrons. To get a sample of background events that are as similar as possible to the ones that passed the selection requirements of our data sample, we look for events that pass almost all our selection criteria, but that contain one or more EM candidates that are somehow well-identified as a fake electrons. We use an inverse H-matrix cut to select EM candidates that are due to jets. We can require either one or both of the EM candidates fail the H-matrix selection, and see how this affects the kinematic distributions of our background sample. The "di-jet" sample is made by requiring that both jet candidates fail the H-matrix cut (H-matrix(7) greater than 30 for candidates in the CC, H-matrix(8) greater than 40 for candidates in the EC). The "EM plus jet" sample is made by requiring one EM candidate pass all selections, including Hmtrx, and an additional EM candidate that satisfies all requirements, except H-matrix (H-matrix(7) > 120 for CC candidates, H-matrix(8) > 150 for EC candidates). Because most EM

candidates due to jets will not have a matched track, we also removed the spatial track match requirement in the event selection. The di-jet QCD background is selected from the 2EM high p_T skim and the EM+jet is selected from the 1EM skim. Fig.6.1 shows the invariant mass distributions of the di-jet and EM+jet QCD backgrounds, overlaid. Fig.6.2 shows the p_T distributions of the di-jet and EM+jet QCD backgrounds overlaid.

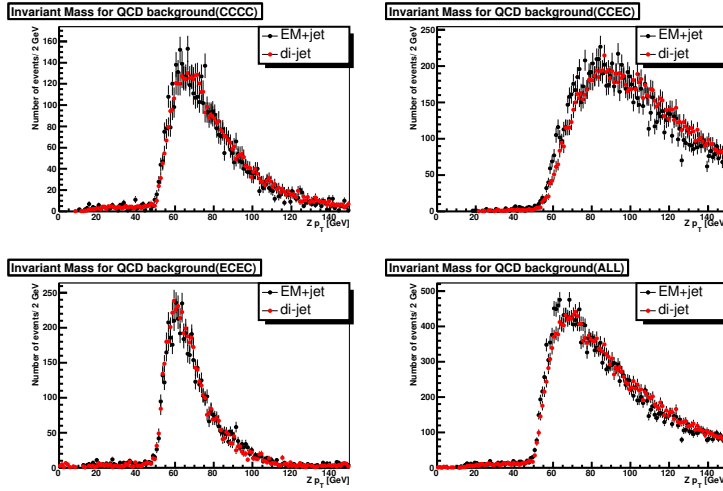


Figure 6.1: Invariant mass distribution for the QCD background di-jet sample and EM+jet sample

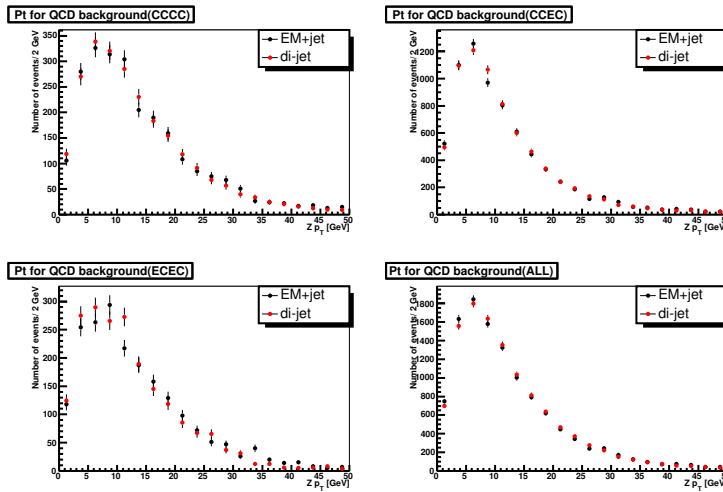


Figure 6.2: p_T distribution for the QCD background di-jet sample and EM + jet sample

The invariant mass distribution of the QCD background is determined from the average of the

invariant mass distributions of the two kinds of QCD backgrounds, as is presented in Fig.6.3. To determine the background fraction, the invariant mass distribution of the $Z/\gamma^* \rightarrow e^+e^-$ data sample is fitted as a linear combination of the invariant mass distribution of the QCD background and the signal (from ResBos+PHOTOS+PMCS). The fit is performed in the invariant mass window $[50,130]$ GeV/ c^2 .

$$N_{50-130}^{data} = \alpha_1 \times N_{50-130}^{signal} + \alpha_2 \times N_{50-130}^{bkg} \quad (6.1)$$

and we calculate a likelihood for each α_1 and α_2 pair. The configuration that has the maximum likelihood gives the best fit values for α_1 and α_2 . The fitting results are shown in Fig.5.16 and 5.17. Finally, the background fraction in the $[70,110]$ invariant mass window is calculated as:

$$f_{bkg} = \alpha_2 \times \frac{N_{70-110}^{bkg}}{N_{70-110}^{data}} \quad (6.2)$$

The error on α_2 , $\delta\alpha_2$ is determined from the maximum likelihood fit. The total uncertainty on f_{bkg} is calculated as $\sqrt{\delta\alpha_2^2 + \delta_{stat}^2}$, where δ_{stat}^2 is due to limited events statistics.

Table 6.1 shows the background fraction for events in different calorimeter regions.

Region	χ^2/ndf	background fraction
CC-CC	64/80	1.30±0.14%
CC-EC	106/80	8.55±0.26%
EC-EC	80/80	4.71±0.30%
All	111/ 80	4.70±0.13%

Table 6.1: Background fractions for events in different calorimeter regions.

We also use the average of the p_T distributions of the QCD background when correcting the measured distribution from our sample for background contamination. The p_T distribution is presented in Fig. 6.4. We assign the difference between the average and the result using the individual shapes as the systematic errors on the QCD background shape.

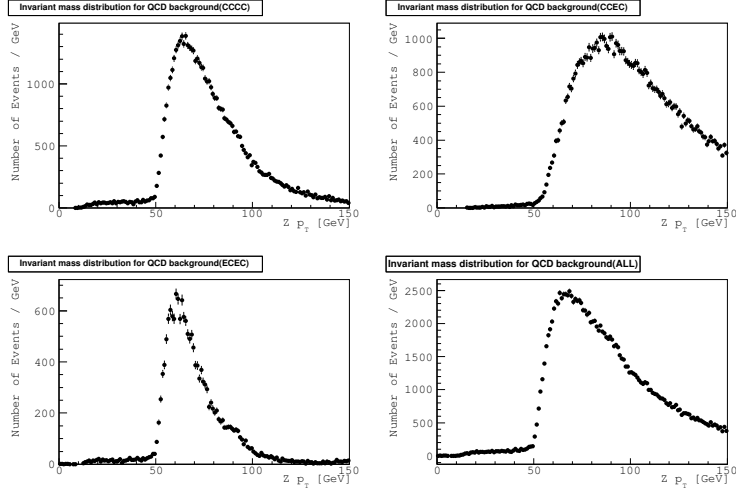


Figure 6.3: Invariant mass distribution for the QCD background

6.2 Non QCD Backgrounds

Other potential sources of background include $Z \rightarrow \tau^+\tau^-$ and diboson ($WW, WZ, W\gamma$) production; their contributions are studied using Monte Carlo simulation.

6.2.1 $Z \rightarrow \tau^+\tau^-$

We use PYTHIA[56] to generate $Z \rightarrow \tau^+\tau^-$ events and use the Tauola[57] Monte Carlo code to decay the τ . The $\sigma \times \text{Br}(Z \rightarrow \tau^+\tau^- \rightarrow e^+e^-)$ is about 7 pb. The generated 500k events were fed into parameterized Monte Carlo for smearing and event selection. The resulting acceptance is about 0.0025, yielding an expected 16.9 events for 1 fb^{-1} data sample. The contribution of $Z \rightarrow \tau^+\tau^-$ to the sample is thus negligible.

6.2.2 Di-boson backgrounds

Di-boson events are generated using PYTHIA and they are also fed into parameterized Monte Carlo to determine the acceptance. Table 6.2.2 shows the expected number of events for each of the di-boson background.

As can be seen from the table, contributions from di-boson background processes are negligible.

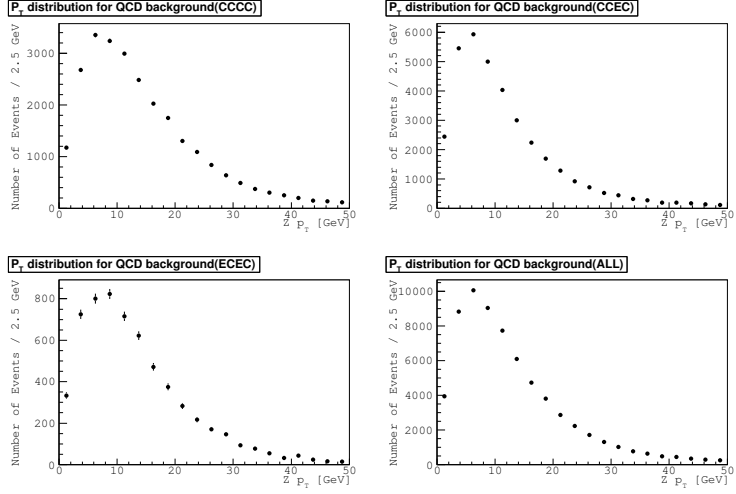


Figure 6.4: p_T distribution for the QCD background

Di-boson	$\epsilon * A$	$\sigma * Br$	$N(1 \text{ fb}^{-1})$
WW	0.059	0.1 pb	6.2
WZ	0.17	0.009 pb	15.5
$W\gamma$	0.005	12.2 pb	61

Table 6.2: Expected number of events for 1 fb^{-1} data.

Chapter 7

Efficiency×Acceptance Correction

Once the data is selected, corrections are needed in order to turn the measured p_T distribution into a differential cross section. In the previous Chapter, I discussed background subtraction. In this Chapter, I discuss another important correction.

7.1 Efficiency and Acceptance

When selecting signal events, one tries to enhance the number of signal events relative to the number of the background events. During selection, some fraction of both the signal and background events will fail the selection criteria. The effect of these selection cuts needs to be carefully studied and taken into account in the final result.

7.2 Dependence of the selection efficiency on the boson p_T

I first discuss the efficiency of the electron selection criteria as a function of the Z boson p_T . To understand the effect of each selection variable on the Z p_T , first, we look at their individual Z p_T dependences. To see this dependence, for each good electron in a selected $Z/\gamma^* \rightarrow e^+e^-$ event from the data sample, the average value for each selection variable as a function of electron p_T can be plotted. Fig. 7.1 shows the average values for isolation, H-matrix(7), H-matrix(8) and spatial track match χ^2 probability as a function of Z p_T , respectively.

We can see that the isolation of the electron has the most dependence on the Z p_T . This dependence is due to jet activities, especially jet activity due to the recoil against the the Z , which spoils the isolation of nearby electrons, and is strongly depend on the Z boson p_T . The other electron identification variables have only a weak (negligible) dependence on the boson p_T . We use the GEANT-based DØ full Monte Carlo detector simulation help us understand p_T dependent efficiency. $Z/\gamma^* \rightarrow e^+e^-$ events are generated using PYTHIA and overlaid with

minimum bias events. Since PYTHIA is a leading order event generator, it does not produce events with the correct p_T distribution. To correct for this, at the generator level, we re-weighted the events to correct to the ResBos Z p_T spectrum. The generated events were then passed through the detector simulation. The *efficiency as a function of Z boson p_T* is defined as the ratio of the number of reconstructed events that pass kinematic, geometric and electron quality requirements to the number of reconstructed events that pass only kinematic and geometric requirements.

$$eff(Z p_T) = \frac{Z p_T(\text{acceptance cuts, efficiency cuts})}{Z p_T(\text{acceptance cuts})} \quad (7.1)$$

Included in the electron efficiency requirements are the preselection(including isolation, EM fraction and EM ID), spatial track-match and H-matrix requirements. The total efficiency as a function of Z p_T is presented in Fig. 7.2 . The efficiency first decreases as Z p_T rises; this is because when Z p_T is low, the recoil is small, and the two electrons tend to be back-to-back. As Z p_T increases, the recoil also increases, and spoils the isolation quality of the electrons. At Z p_T of about 45 GeV/ c , the kinematics change; the two electrons both tend to be in the direction opposite that of the recoil, and the recoil does not affect the electron isolation as much any more. On the other hand, the p_T of the electrons also increases as Z p_T increases, and this causes the efficiency to rise as well, slowly back to the initial efficiency, and goes flat thereafter.

It is important that the Z p_T dependence of the efficiency be insensitive to the Z p_T distribution of the sample that was used to derive the dependence. We compare the dependence of the efficiency on Z p_T for two cases: using the original PYTHIA Z p_T and using the re-weighted Z p_T , as presented in Fig. 7.2. We can see that the efficiency Z p_T dependence changes very little after re-weighting.

This study only measures the p_T dependence of the efficiency. For the normalization, we use the total selection efficiency measured from the data convoluted with the kinematic distributions of Z boson events through the parameterized Monte Carlo simulation, which contains the measured single electron efficiencies. The average efficiency is determined to be $(75.04 \pm 0.05)\%$.

Since the Z p_T spectrum also depends on the Z boson rapidity, we divide our Z events into four different Z rapidity bins: $|y| < 1$, $1 < |y| < 2$, $|y| > 2$ and all y . We plot the Z p_T dependence of the efficiency for different Z rapidity binnings in Fig.7.3 . Finally, we fit the scaled efficiency as function of Z p_T for all Z rapidity and obtain:

$(0.768 \pm 0.001) - (0.0025 \pm 0.0001)p_T + (0.000038 \pm 0.000003)$ for $p_T < 62.5$ GeV/ c ; (0.760 ± 0.004) for $p_T > 62.5$ GeV/ c , as is presented in Fig.7.4.

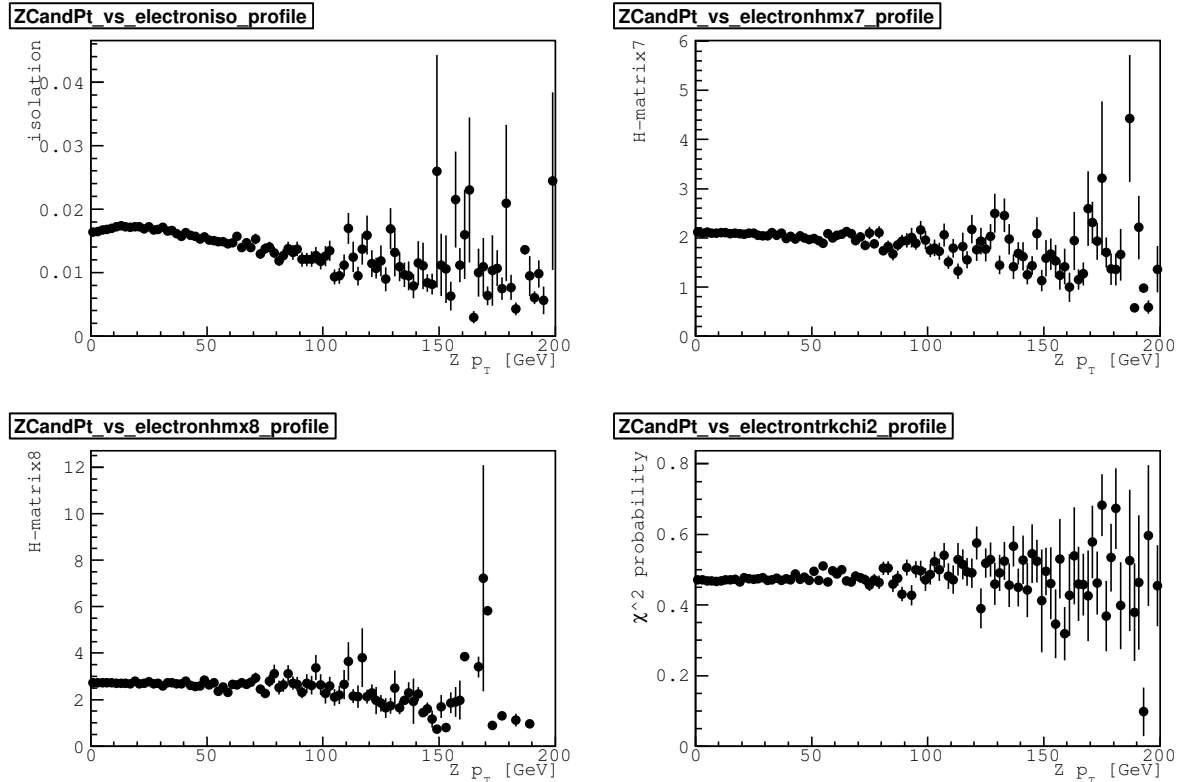


Figure 7.1: Profile of electron isolation, H-matrix(7)(CC), H-matrix(8)(EC) and spatial track match χ^2 probability as a function of Z p_T .

To study the systematic uncertainty, we compare data to full Monte Carlo events. From the data, we can't really get the Z p_T dependence of the efficiency, as defined by equation 7.1, because in the denominator there are no efficiency cuts applied, and the QCD background dominates the signal. But we can add a spatial track-match requirement, and get rid of most of the QCD background. Furthermore, since the track-match efficiency does not depend on Z p_T ,

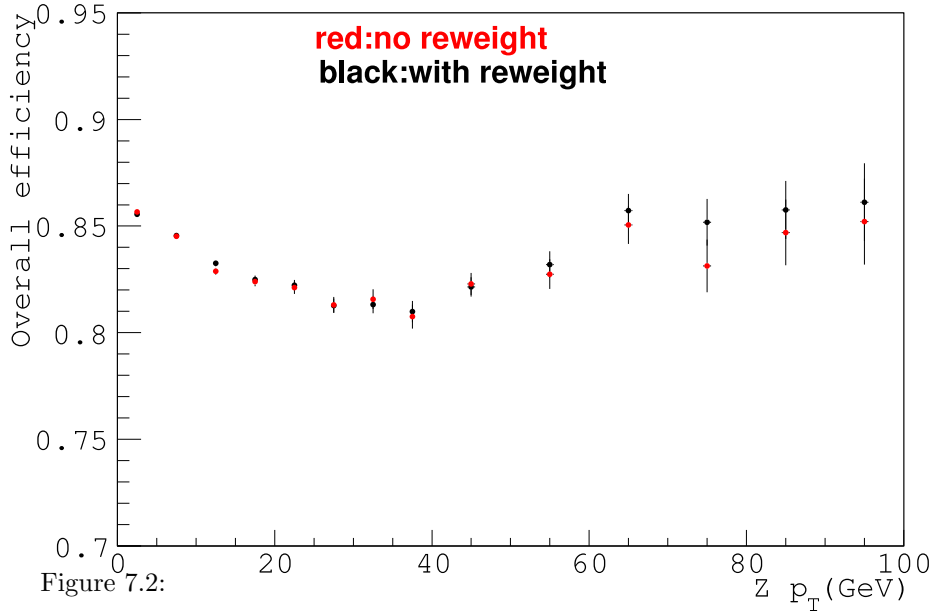


Figure 7.2:

Efficiency as function of Z boson p_T for PYTHIA and re-weighted Monte Carlo sample

adding this requirement should not affect the shape of the distribution.

The efficiency, excluding track-match efficiency, as a function of $Z p_T$ can be written as follows:

$$eff(Zp_T) = \frac{Zp_T(\text{acceptance cuts, efficiency cuts})}{Zp_T(\text{acceptance cuts, spatial track match cut})} \quad (7.2)$$

There is still background in both numerator and denominator samples that need to be subtracted. After background subtraction, the revised efficiency $Z p_T$ dependence from data is shown in Fig.7.5 and compared with the same plot from the full Monte Carlo. The two distributions are in good agreement, showing that our full Monte Carlo does a good job describing the jet activity and its effect on the $Z p_T$ spectrum. From this data and full Monte Carlo comparison plot, we assign an estimated uncertainty on the dependence of the efficiency on Z boson p_T of 2% in the bins below 60 GeV/ c and 4% in the bins above 60 GeV/ c .

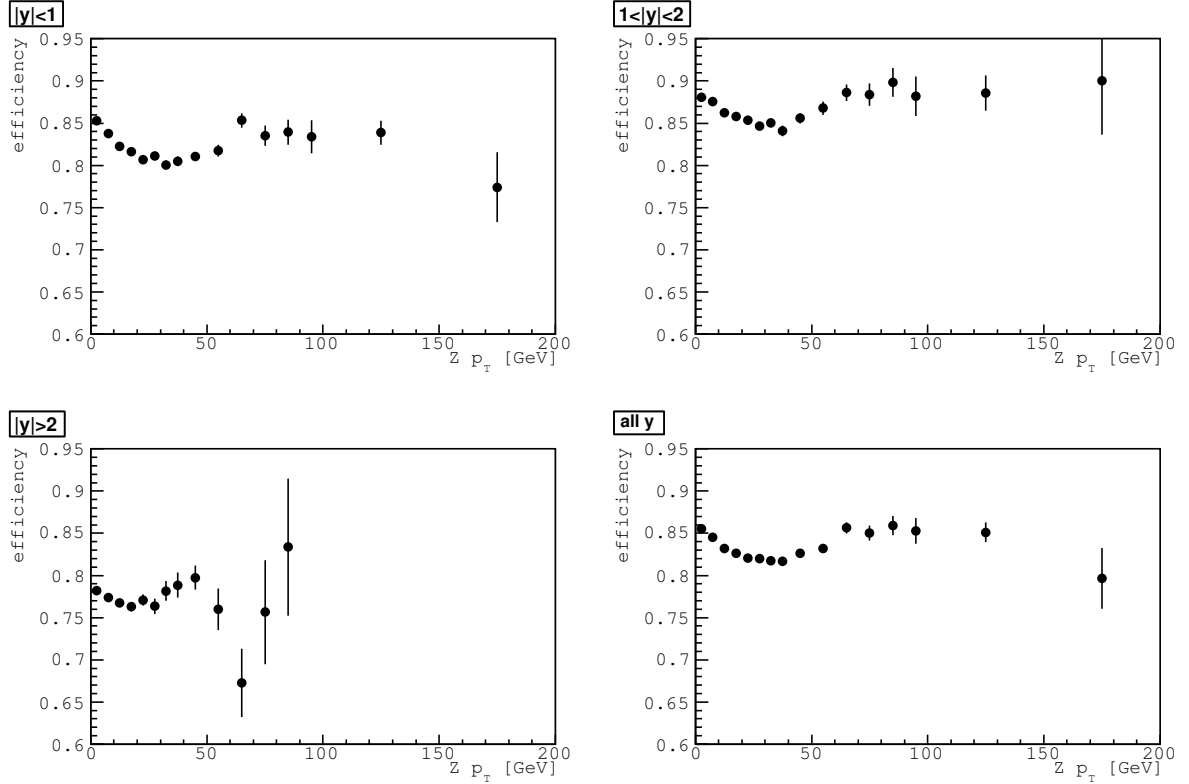


Figure 7.3: Efficiency as function of Z boson p_T for different Z rapidity bins

7.3 Dependence of the geometric and kinematic acceptance on the boson p_T

Acceptance cuts include kinematic and geometric cuts. We use the parameterized Monte Carlo detector simulation to study the dependence of the acceptance on boson p_T . $Z/\gamma^* \rightarrow e^+e^-$ events are generated using ResBos and PHOTOS. The *acceptance as a function of Z p_T* is defined as the ratio of the number of smeared events that pass kinematic and geometric requirements to total number of smeared events, and is presented in Fig.7.6. The pattern of the curve can be understood by breaking it down to two different plots: acceptance of the geometric cuts and acceptance of the kinematic cuts. The reason that the acceptance of the kinematic cuts first decreases and then increases is as follows: when the Z p_T is low, the two electrons tend to be back-to-back and have similar p_T . As the Z p_T increases, the electron along the Z p_T direction will carry more energy and the other one will carry less. The lower energy electron may fail the electron p_T cut. When the Z p_T is larger than about 45 GeV/c, both electrons will more

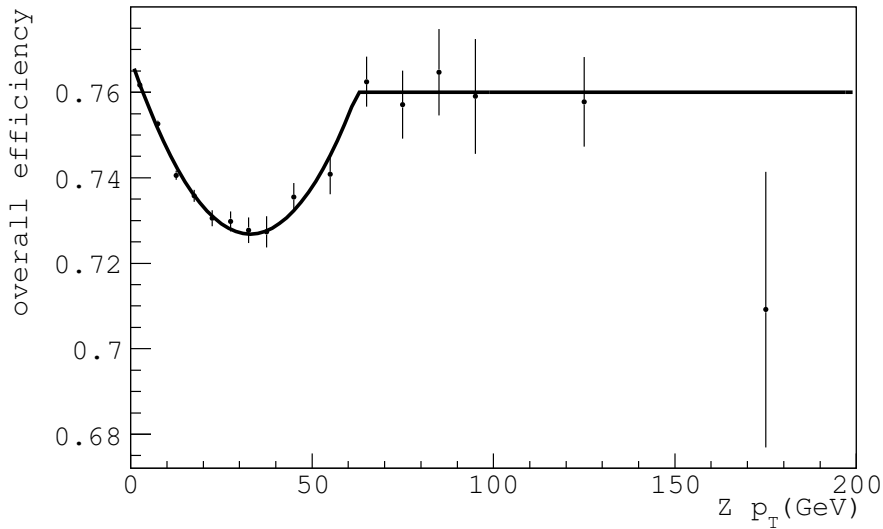


Figure 7.4: Overall efficiency as a function of Z boson p_T

and more be pointing towards the same direction (the direction of the parent Z). The asymmetry between the two electrons then goes away, resulting an increase of efficiency at high $Z p_T$. The reason the geometric acceptance increases at high p_T is that when the $Z p_T$ increases, the Z boson is more and more “central”, which makes it’s daughter electrons more likely to pass the angular geometric cuts.

The uncertainties on the acceptance from the PMCS smearing parameters, such as the energy scale, the energy offset and the energy resolution terms, are determined by varying each parameter by its measured uncertainty. The fractional uncertainty on the acceptance due to the smearing parameters is shown in Fig.7.7.

7.4 p_T dependent Efficiency \times Acceptance

Finally the Efficiency \times Acceptance as a function of Z boson p_T is plotted in Fig.7.8. This dependence will be applied in the unfolding program to correct the unfolded $Z p_T$ spectrum for the efficiencies and acceptances of our selection criteria.

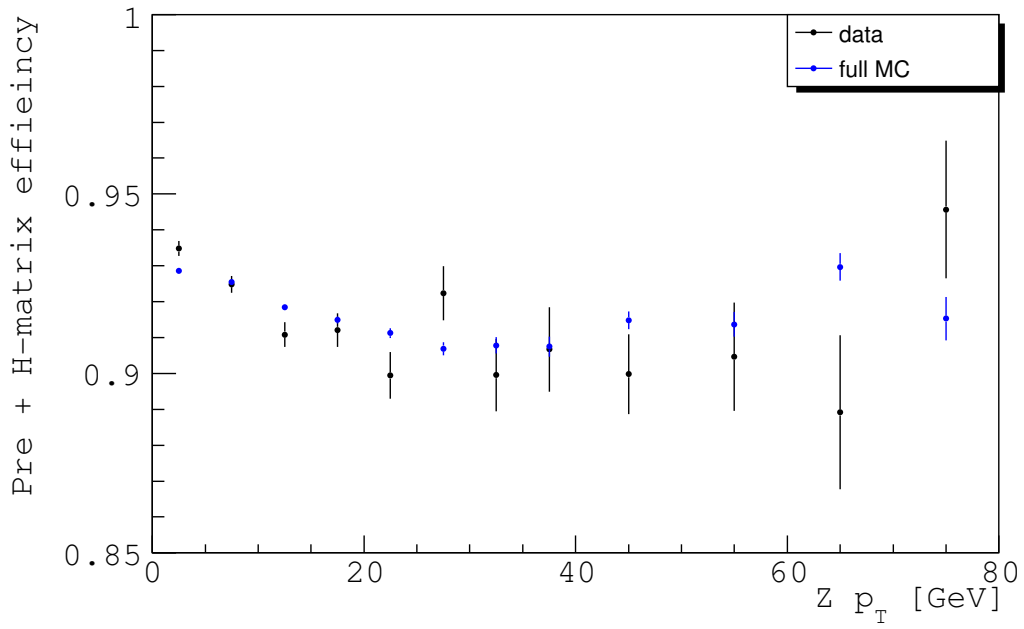


Figure 7.5: Revised efficiency as function of Z boson p_T for data and full Monte Carlo

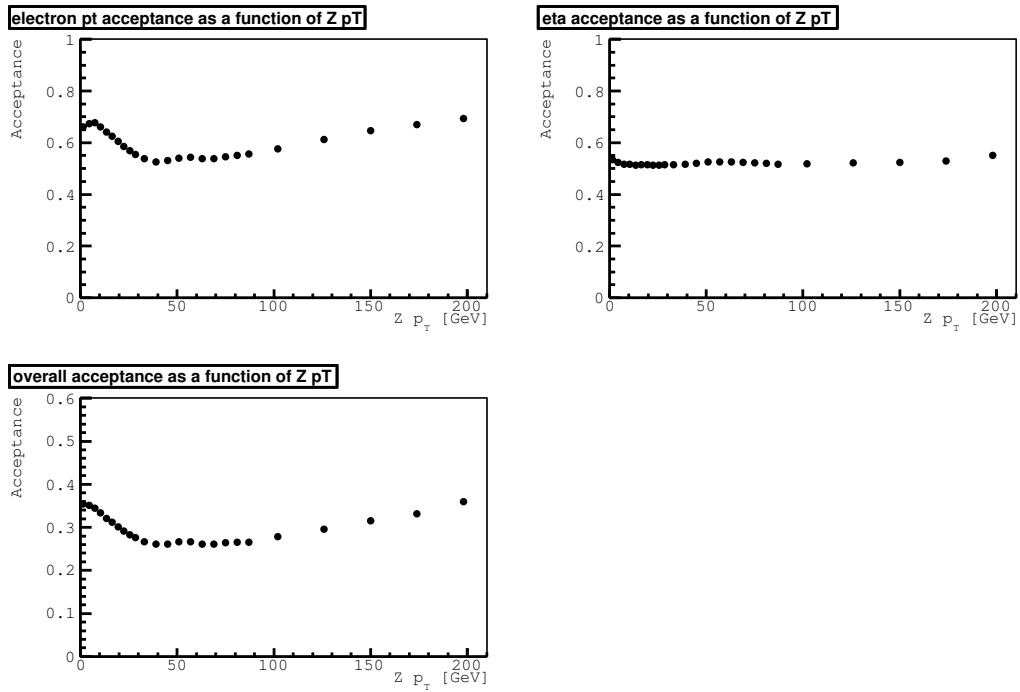


Figure 7.6: Shown here are the acceptances as a function of Z boson p_T

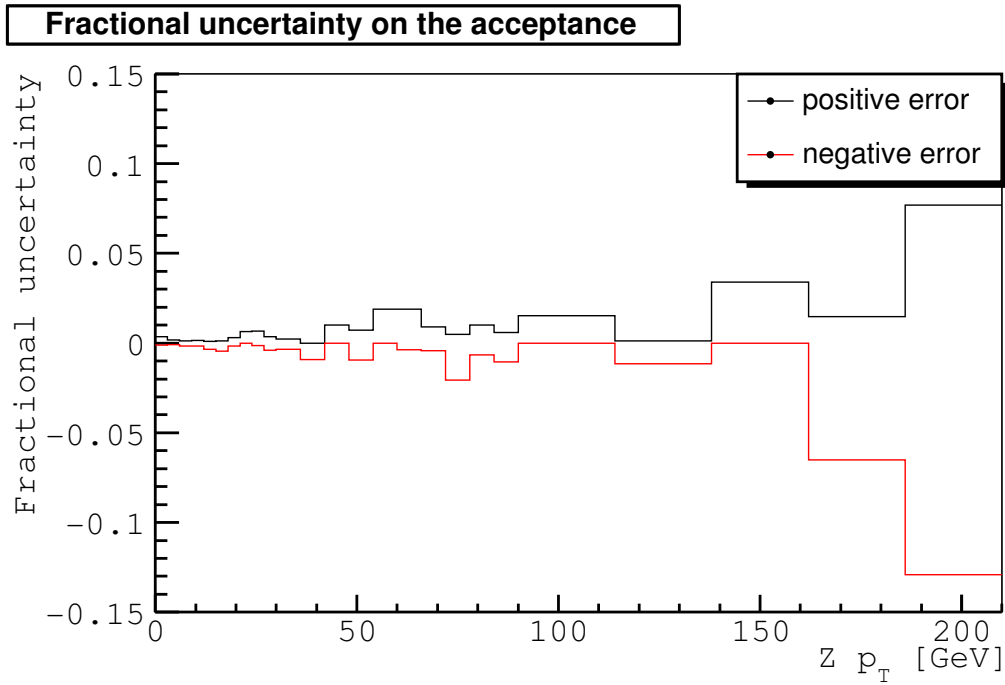


Figure 7.7: Fractional uncertainty on the acceptances due to the smearing parameters as a function of Z boson p_T

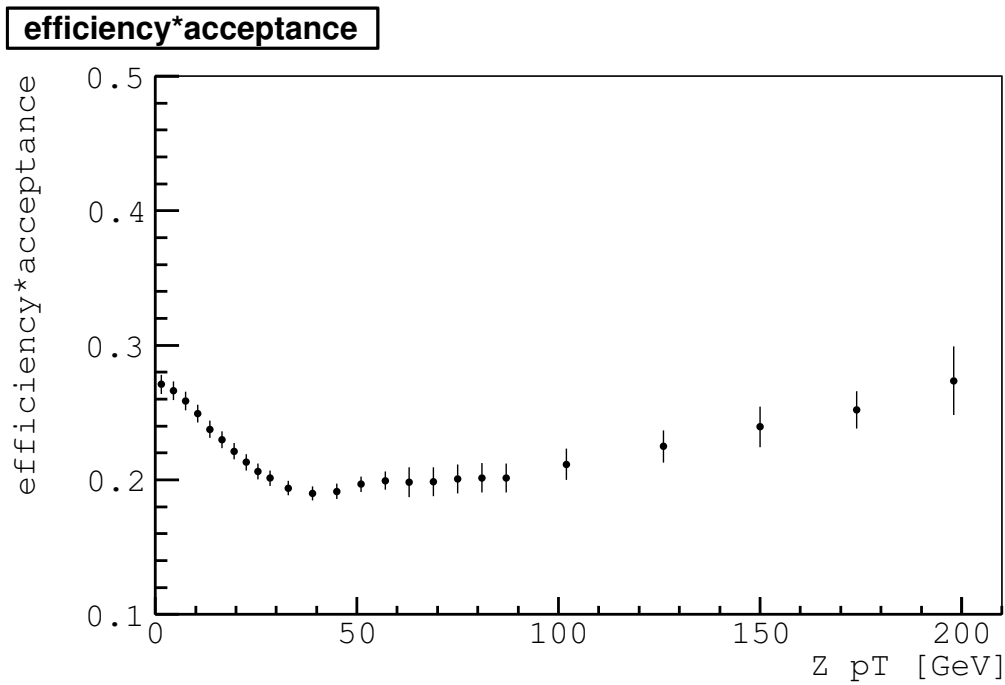


Figure 7.8: Efficiency*acceptance as a function of Z boson p_T

Chapter 8

Results

8.1 Unfolding the Detector Smearing

The measured Z boson p_T spectrum is smeared due to detector resolution. To compare with the theory calculation directly, we use a program called *RUN(Regularized Unfolding)* [58] to unfold this detector effect.

The relation between the distribution $f(x)$ of the true variable x , and the measured distribution $g(y)$ of the vector y of measured quantities is given by the equation:

$$g(\vec{y}) = \int A(\vec{y}, x) f(x) dx + b(\vec{y}) \quad (8.1)$$

where $A(\vec{y}, x)$ denotes the resolution function, including the all the detector effects of limited acceptance, transformation and finite resolution. In general, $A(\vec{y}, x)$ is not known as a function in analytical or empirical form.

8.2 The Program RUN

The algorithm used in RUN works as follows: internal to the program, a weighting function $f_{mult}(x)$ is defined and is represented by a smooth function, parameterized by B-splines:

$$f_{mult}(x) = \sum_k a_k p_k(x) \quad (8.2)$$

Input to the unfold program are ntuples¹ from the data, ntuples from the true Monte Carlo and ntuples from the smeared Monte Carlo. The two Monte Carlo ntuples have a one to one correspondence, i.e., each entry in the smeared Monte Carlo is the result after the detector smearing of an entry in the true Monte Carlo ntuples. In the program, the smeared Monte Carlo is re-

¹a ntuple is a sequence or ordered set or list containing n objects.

weighted using $f_{mult}(x)$ and fit to the data distribution $g(\vec{y})$. The fit result determines $f_{mult}(x)$. The final unfolding result is then given by:

$$f(x) = f_{mult}(x) \cdot f_0(x) \tag{8.3}$$

where $f_0(x)$ is the input true Monte Carlo x distribution.

8.3 Setup of the Unfolding Program

The inputs to the program are:

- ntuples of the measured $Z p_T$ from the data
- ntuples of the $Z p_T$ of all generated Monte Carlo events, including those inside and outside of the detector acceptance.
- ntuples of the $Z p_T$ of the smeared Monte Carlo events, organized so that they have a one-to-one correspondence with the generated events. For the unfolding fit, to ensure only those events inside detector acceptance are used, we apply the p_T dependent Efficiency \times Acceptance.
- ntuples containing the p_T distribution of the QCD background.

There are also several parameters need to be set by the user in RUN:

- XBINS: this defines the binning of your unfolded result. Because at low p_T region, the $Z p_T$ resolution is about 2 GeV/ c , we choose the binning width below 30 GeV/ c to be 2.5 GeV/ c . Our binning below 30 GeV/ c are: 0. 2.5 5. 7.5 10. 12.5 15. 17.5 20. 22.5 25. 27.5 30.
- NRDF: this is the number of degree of freedom, which roughly equals to the number of points.
- KNOTS: this is the number of knots of the spline function. It should be about $2 \times \text{NRDF} + 3$.

The normalization of the result is set as one. So the final result of this measurement is actually the shape of the p_T distribution $\frac{1}{\sigma} \frac{d\sigma}{dp_T}$.

8.4 Test of the Unfolding Program

First we test the robustness of the unsmearing program, RUN. In the test, the “data” is smeared Monte Carlo using $g_2=0.53$ for ResBos; the “data” is required to pass the same event selection requirements as the real data. The “Monte Carlo samples” are events generated using $g_2=0.83$ for ResBos and its corresponding smeared Monte Carlo event sample. The two generator level p_T distributions are quite different, as shown in Fig. 8.1. One would expect the output of the program to be consistent with the $g_2=0.53$ generator Monte Carlo distribution, since the unfolded result from a good unfolding program should not depend on the input Monte Carlo. Fig. 8.2 shows that the unfolded Z p_T spectrum is consistent with our expectation, with a $\chi^2/\text{ndf}=35/11$ between the unfolded spectra and the generator spectra with $g_2=0.53$ vs. $\chi^2/\text{ndf}=6972/11$ between the unfold spectra and the generator spectra with $g_2=0.83$, clearly favoring the former.

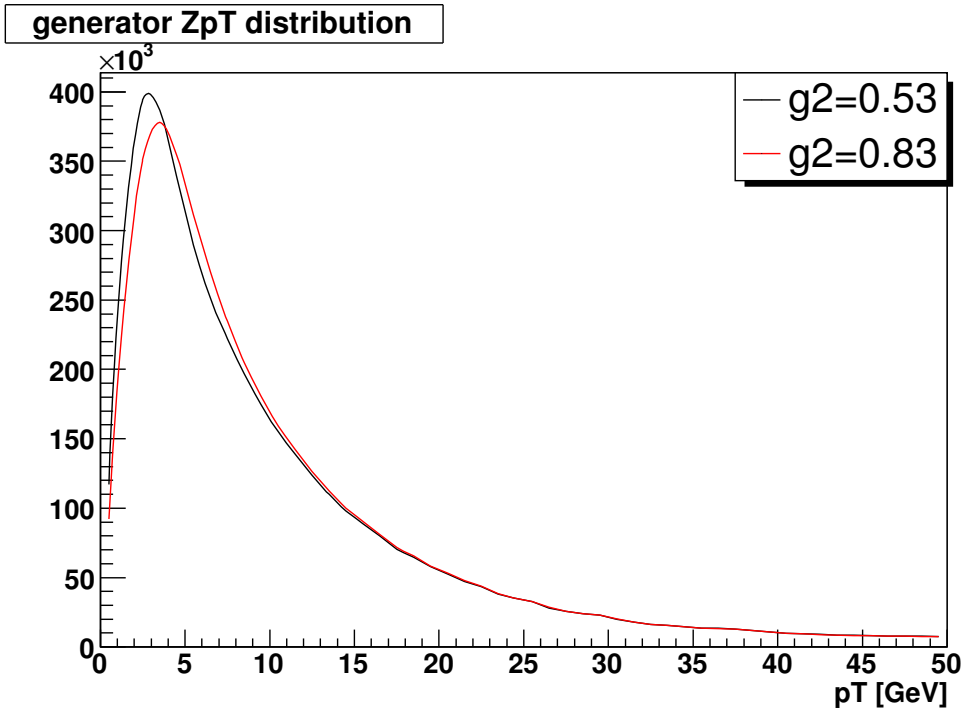


Figure 8.1: Comparison between the generated Z boson p_T spectrum for different values of g_2 for ResBos.

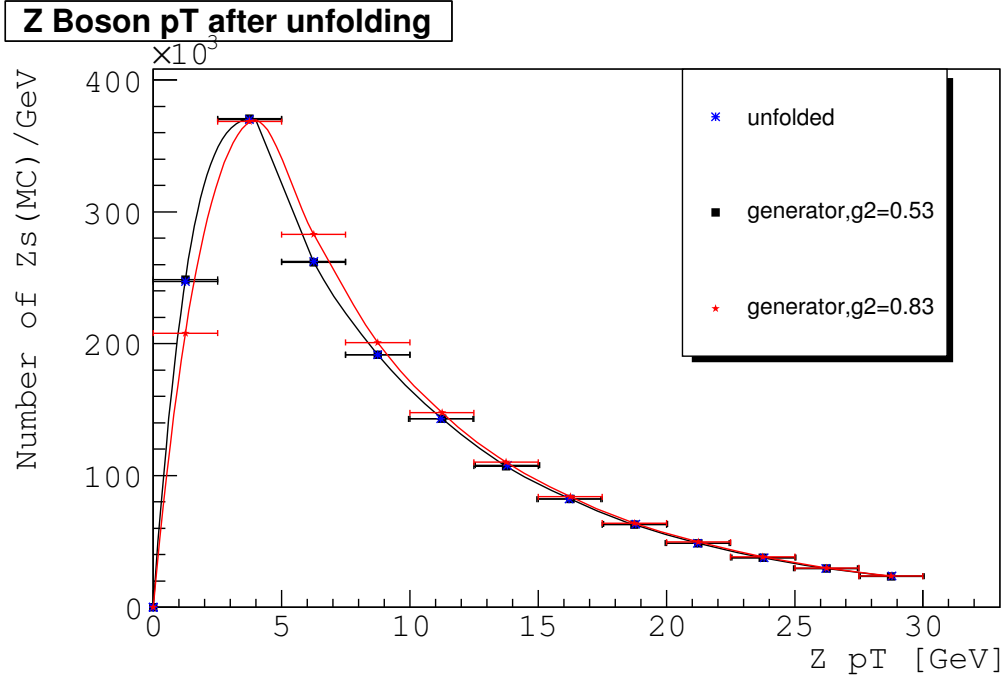


Figure 8.2: Comparison between the unfolded and generated Z boson p_T for the test.

8.5 Unfolded Result

Using the measured data as input, the unfolded Z p_T spectrum $\frac{1}{\sigma} \frac{d\sigma}{dp_T}$ is shown in Fig. 8.3 . The errors shown in this plot are statistical errors only.

8.6 Systematic Uncertainties

Systematic uncertainties on the unfolded Z p_T spectrum arise from the following sources:

- energy scale and offset applied to the electron energy
- energy resolution terms. The uncertainty on the sampling term is parameterized by a “fudge-factor” parameter S , which describes the difference between the Monte Carlo and the data. The noise term N is considered fixed with no uncertainty. Actually at the energy level of Z boson, the noise term contribution is very small. And the last one is the uncertainty of the constant term C .

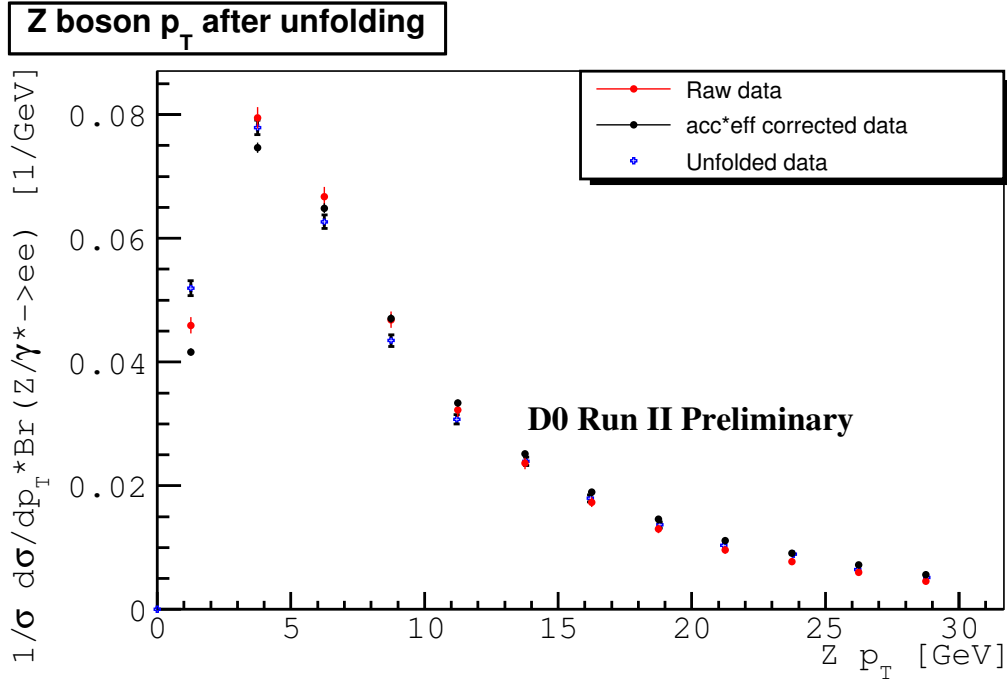


Figure 8.3: Cross section normalized unfolded Z boson p_T distribution. The error shown in this plot is statistical error only.

- parton distribution functions.
- unfolding method
- Z p_T dependence of the efficiency obtained from full Monte Carlo
- Z p_T dependence of the acceptance
- background level and shape

8.6.1 Uncertainties from the smearing parameters during unfolding

When we unfold the measured Z p_T spectrum, if the smearing information contained in the true-smearing Monte Carlo pairs is not correct, the unfolded result will be biased. The systematic uncertainty associated with this unfolding process is estimated as follows:

Energy Scales and Energy Offsets

For the energy scale parameters, energy offset parameters, the uncertainties on the unfolded Z p_T spectrum are estimated by varying each parameter by its uncertainty and noting the effect of the resulted Z p_T spectrum. The uncertainties due to the energy scales and energy offsets are presented in Fig. 8.4 and 8.5.

Energy Resolution Sampling Terms

For the energy resolution sampling terms, their contributions to the unfolded spectrum are estimated using the following methods: First of all, I introduce a fudge parameter S' that multiplies the sampling contributions at all η s and all energies. The process then begins with CC sampling term: First I set $S'(CC)$ to be 1, and tune constant term C to $Z/\gamma^* \rightarrow e^+e^-$ CC-CC data using the Binned-Log-likelihood method. This is actually the default model we used in our parameterized Monte Carlo. Then I fix C at a small value (0 or 0.01 %) and tune $S'(CC)$ to $Z/\gamma^* \rightarrow e^+e^-$ data using the Binned-Log-likelihood method. Finally, the uncertainty (one-sided) on the unfolded Z p_T spectrum from the sampling term will be the difference between the unfolded Z p_T spectrum using the default model (where S' is fixed as 1) and the modified model S' (where S' is free and tuned). Once the CC sampling term uncertainty on the final result is estimated, we then proceed with the sampling terms in positive and negative EC regions using CC-EC $Z/\gamma^* \rightarrow e^+e^-$ data. The uncertainties due to the sampling terms are presented in Fig. 8.7.

Energy Resolution Constant Terms

The constant terms(CC,+EC,-EC) are tuned to $Z/\gamma^* \rightarrow e^+e^-$ data using the Binned-Log-likelihood method by fixing all the other parameters. There is a statistical error on the fitted value for each constant term. The uncertainties on the unfolded Z p_T spectrum due to these constant terms are estimated by varying each of them by its uncertainty and noting the effect of the unfolded Z p_T spectrum. The uncertainties due to the constant terms are presented in Fig. 8.6.

The uncertainty due to all the smearing parameters are shown in Fig. 8.8 , with asymmetric uncertainties.

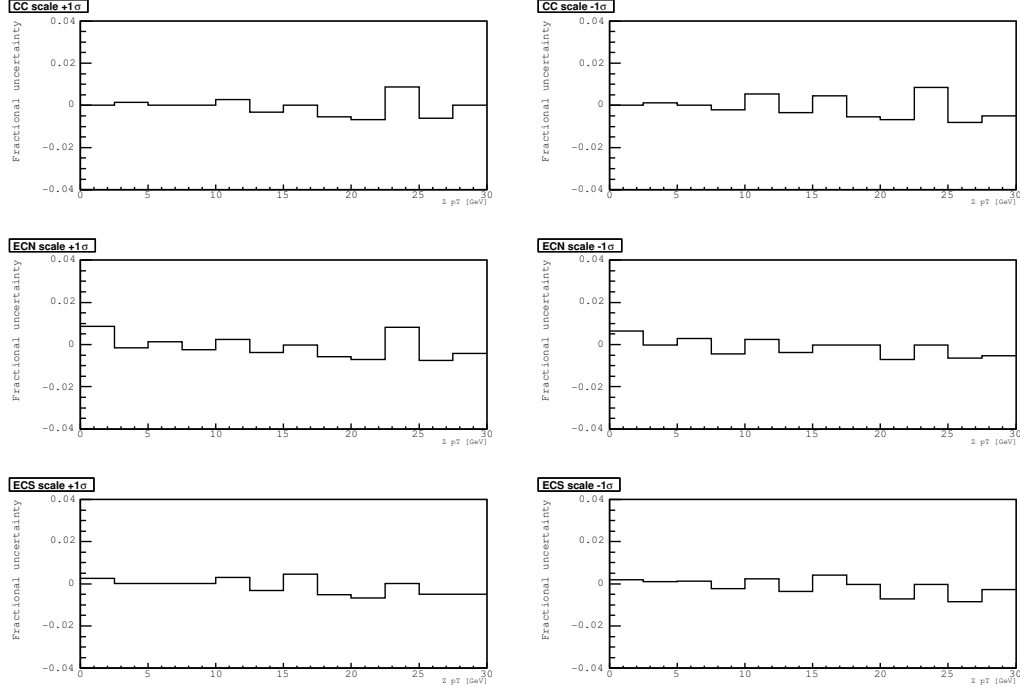


Figure 8.4: Fractional systematic uncertainty on Z boson p_T distribution due to the energy scales.

8.6.2 Uncertainties from the 40 PDFs

We are using ResBos and PHOTOS with the CTEQ6.1m PDFs[59]. The CTEQ6.1m PDFs are defined by twenty orthogonal parameters, which are shifted separately to their positive and negative 1σ limits, providing a set of 40 PDFs for error determination. We generate 10.8 million events for each of the error PDFs and 21.6m events for the base PDF. The difference relative to the base PDF is determined by:

$$(\delta X_{\pm}) = \sqrt{\sum_{k=1}^{20} [X(a_k^{\pm}) - X(a_0)]^2} \quad (8.4)$$

where k is over the 20 PDF parameters and \pm indicates whether the PDF shift up or down results in a positive or negative change in the unfolded Z p_T spectrum. The overall fractional uncertainty due to the 40 PDFs is presented in Fig. 8.9.

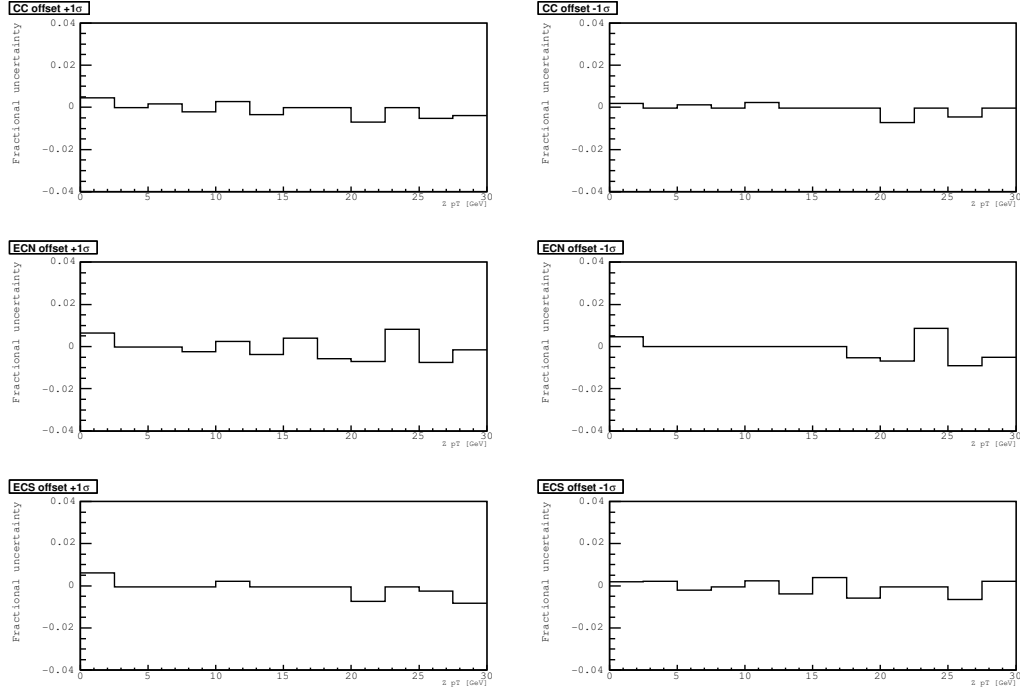


Figure 8.5: Fractional systematic uncertainty on Z boson p_T distribution due to the energy offsets.

8.6.3 Uncertainties from the unfolding program

As is stated previously, there are uncertainties associated with the unfolding program RUN. One uncertainty is from the Monte Carlo input to the program. We estimate this uncertainty using Monte Carlo. Instead of feeding in the data ntuple, we use ResBos to generate Z boson using default $g_2(=0.68)$ and treat the smeared Monte Carlo as “data”. As to the “Monte Carlo”, we change the g_2 value by positive $5\sigma(g_2=0.83)$ and negative $5\sigma(g_2 = 0.53)$, and use ResBos to generate Z bosons to feed to RUN as the “MC” samples. We note the differences between the unfolded results and the generator spectrum with the default g_2 as the systematic uncertainty. We generated 10.8 million events and the uncertainty due to the unfolding program is presented in Fig. 8.10. Here we use asymmetric errors: in each bin, if both differences are positive(negative), the bigger one is used; if one is positive, the other negative, the two errors will be set as the positive (negative) errors for this bin.

Another uncertainty is from the RUN parameters. Among them, “KNOTS” is the number of

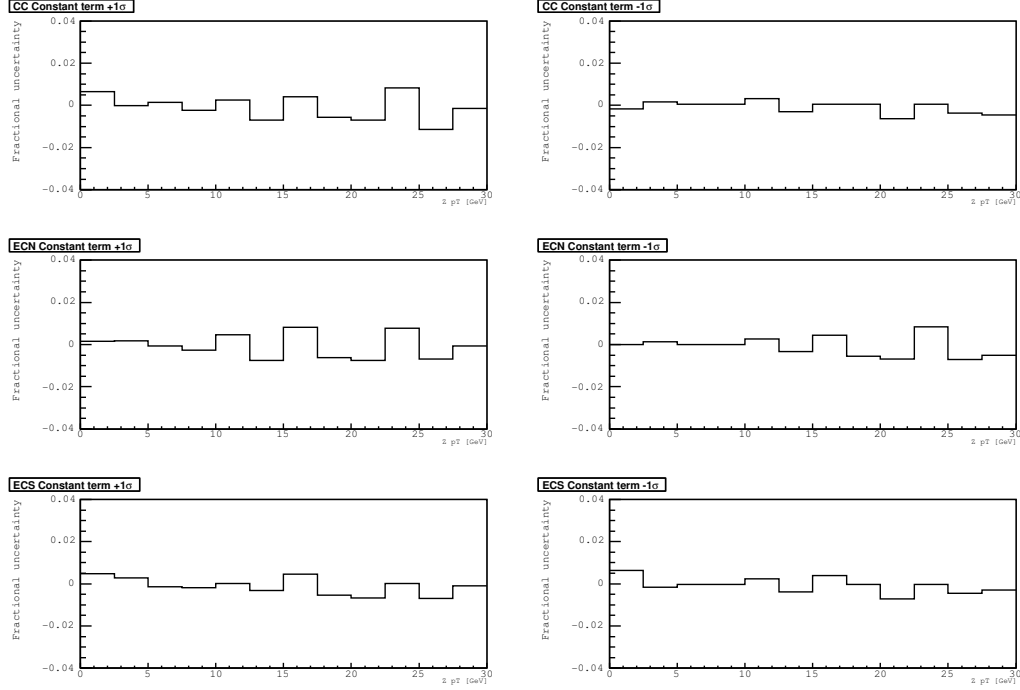


Figure 8.6: Fractional systematic uncertainty on unfolded Z boson p_T distribution due to the constant terms.

spline functions used to characterize the unfolding result, and is most sensitive to the unfolding results[60]. We assign an uncertainty on this parameter by changing the default value(27) up and down by 2, and noting the difference between the unfolded spectrum and the default spectrum, as is presented in Fig. 8.11. We assign a 0.5% error due to the “KNOTS” parameter.

8.6.4 Uncertainties from the Efficiency \times Acceptance p_T dependence

The systematic uncertainty on the Z p_T dependence of the efficiency is due to the discrepancy between data and full Monte Carlo, and is assigned as 2% for Z $p_T < 60$ GeV/ c and 4% Z $p_T > 60$ GeV/ c . The systematic uncertainty on the Z p_T dependence of the acceptance is from the smearing parameters, including the energy scale, energy offset and energy resolution terms. We study it by changing each of the parameters by its uncertainty and noting the difference with the default setting. The fractional uncertainty due to all the smearing parameters was shown in section 7.3.

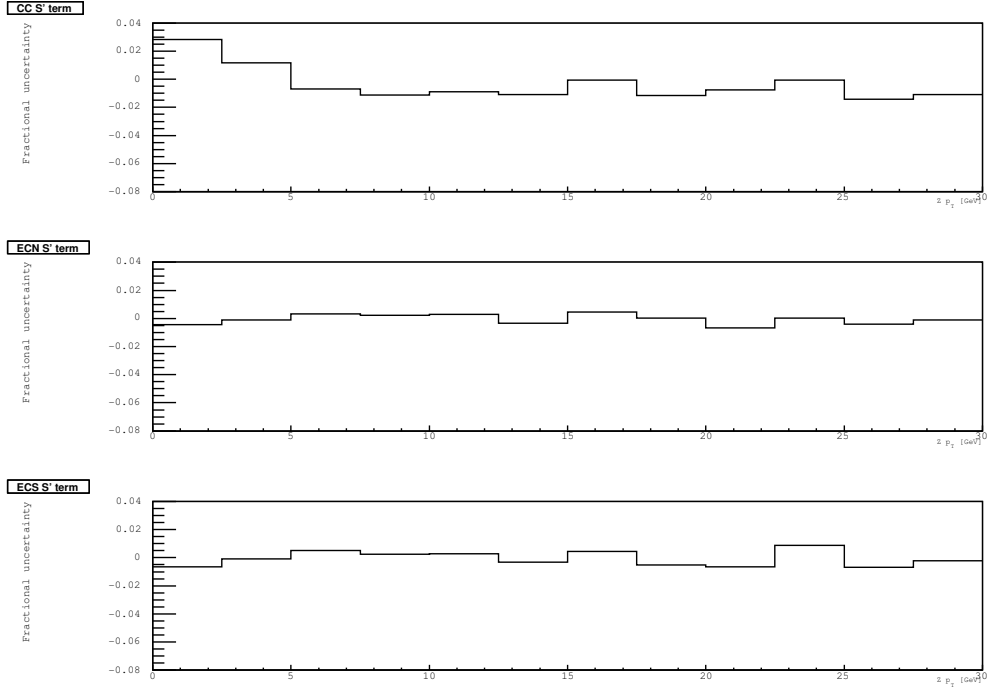


Figure 8.7: Fractional systematic uncertainty on Z boson p_T distribution due to the sampling terms.

8.6.5 Uncertainties from the QCD background

The systematic uncertainty coming from the background fraction is estimated by changing the background fraction by its uncertainty and noting the difference in the unfolded results. The fractional uncertainty due to the background fraction is presented in Fig. 8.12. The uncertainty coming from the background p_T shape is estimated by taking the difference between the case using the average shape and the cases using each of the two QCD background shapes.

Finally, all the systematic uncertainties are plotted in Fig. 8.13.

8.7 Z p_T Distribution For Low p_T Region

The final $\frac{1}{\sigma} \frac{d\sigma}{dp_T}$ distribution, with both statistical and systematic uncertainties, is shown in Fig. 8.14 for $p_T(Z) < 30$ GeV/ c . The differential cross section $\frac{1}{\sigma} \frac{d\sigma}{dp_T}$ is given in Table 8.9. The error correlation matrix is given in Table 8.9.

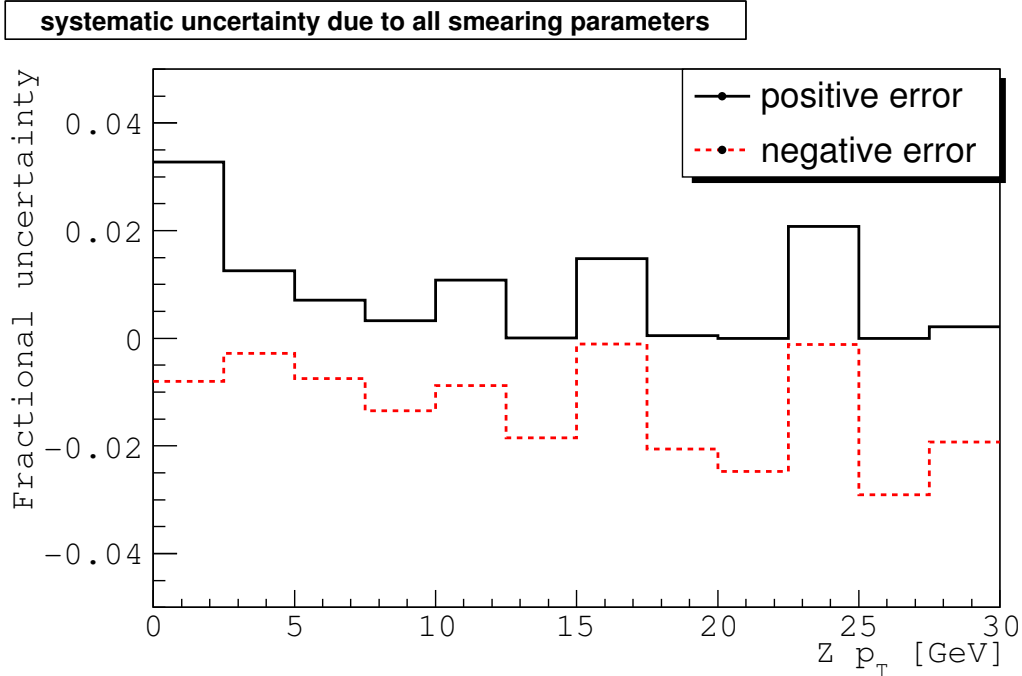


Figure 8.8: Fractional systematic uncertainty on Z boson p_T distribution due to all the smearing parameters.

8.8 Tuning of ResBos g_2 parameter

We also tuned the g_2 parameter in the Ladinsky-Yuan parameterization using a minimum χ^2 fit. We generate ResBos samples with different values of g_2 , and compare the generator Z p_T spectrum with the unfolded result from the data. The χ^2 values as function of g_2 are fit to a quadratic polynomial. The result for the best-fit g_2 value is 0.70 ± 0.05 , with $\chi^2/ndf=11.6/11$. This is presented in Fig. 8.15

8.9 Z p_T Distribution For All p_T Regions

We also perform a measurement of high p_T spectrum as a test of perturbative QCD. The highest Z p_T found in our data sample is 251.2 GeV/ c . Fig. 8.16 shows the detector XY view of the event. The final binning of our result is: 0. 2.5 5. 7.5 10. 12.5 15. 17.5 20. 22.5 25. 27.5 30. 40. 50. 60. 70. 80. 90. 100. 140. 180. 220. 260.

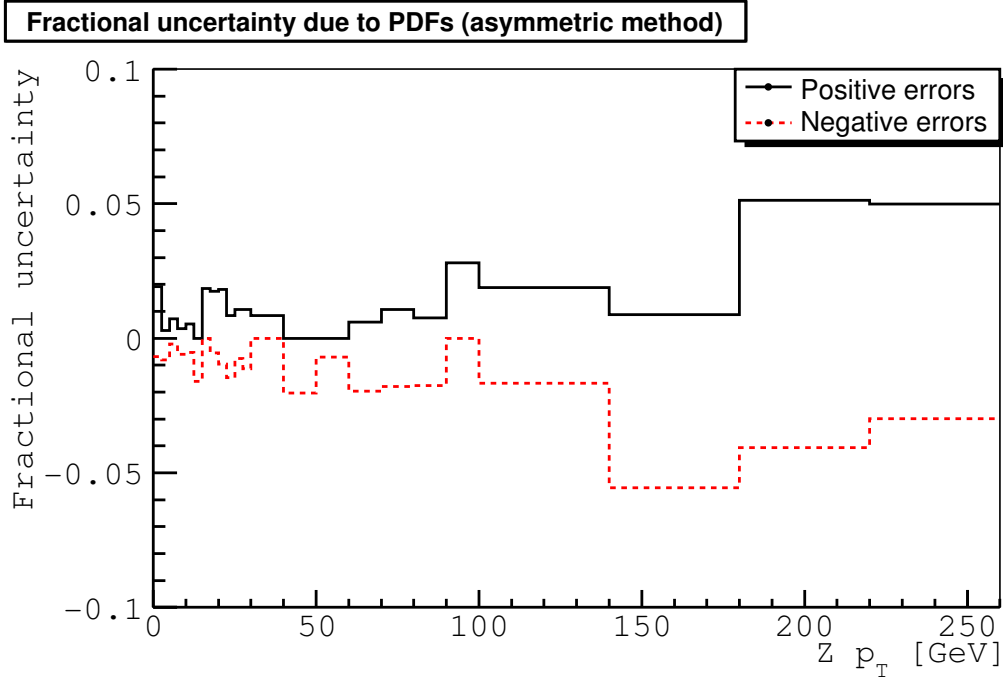


Figure 8.9: Fractional systematic uncertainty on Z boson p_T distribution due to the CTEQ6.1m PDFs.

The final result with both systematic errors and statistical errors is presented in Fig. 8.17. In the same plot, we compare our result with ResBos, which uses a NLO perturbative QCD calculation at high p_T . We also compare our unfolded result with a NNLO calculation from [61] and found very good agreement at high p_T .

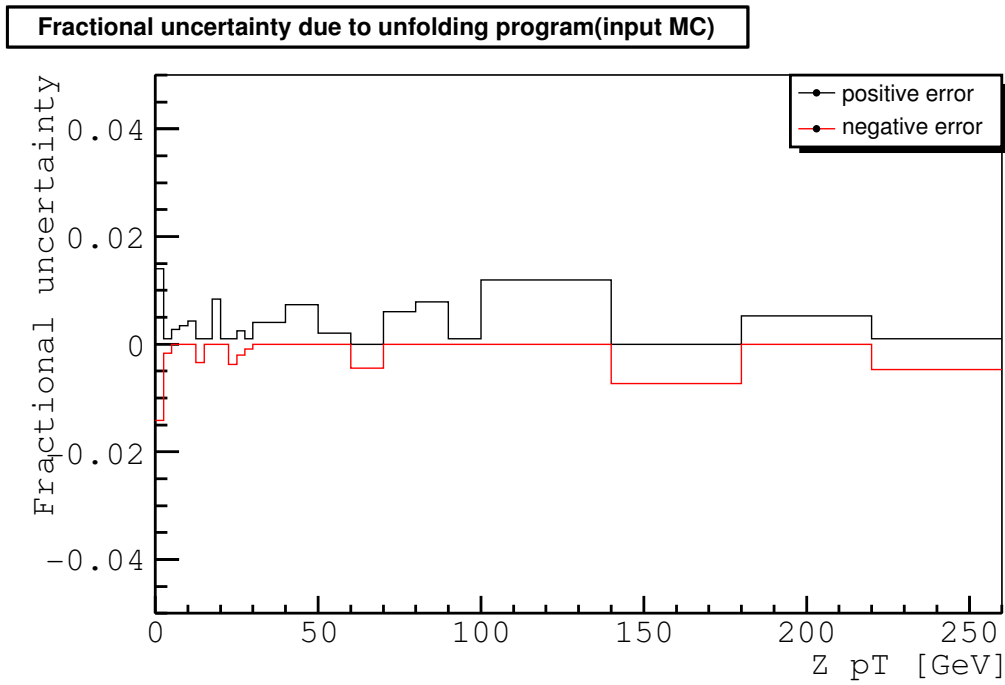


Figure 8.10: Fractional systematic uncertainty on Z boson p_T distribution due to the input MC of the unfold program.

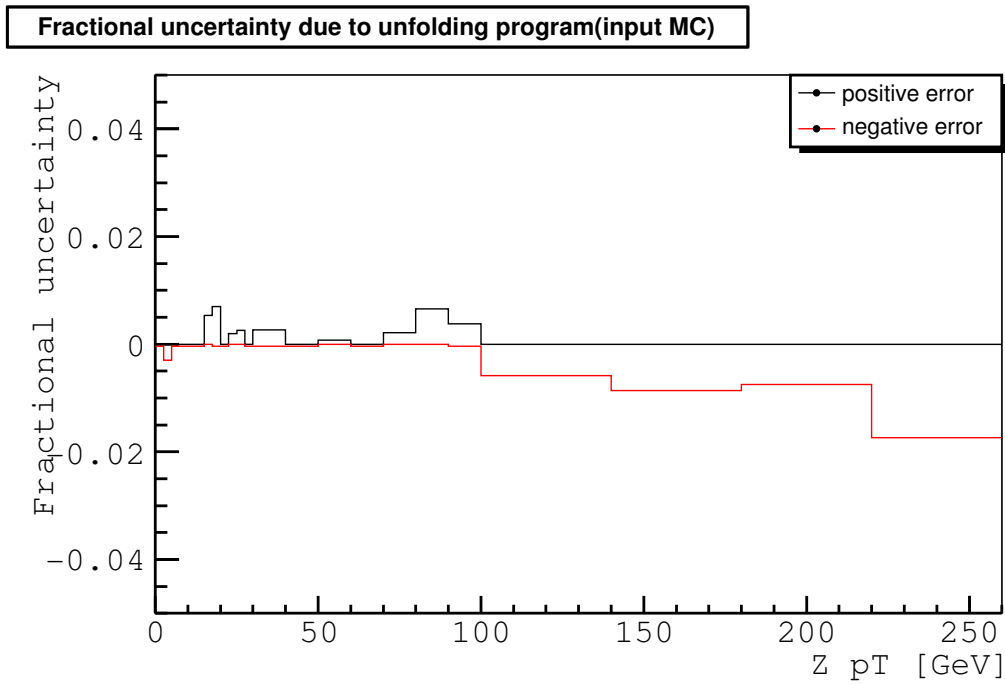


Figure 8.11: Fractional systematic uncertainty on Z boson p_T distribution due to the parameter “KNOTS” of the unfold program.

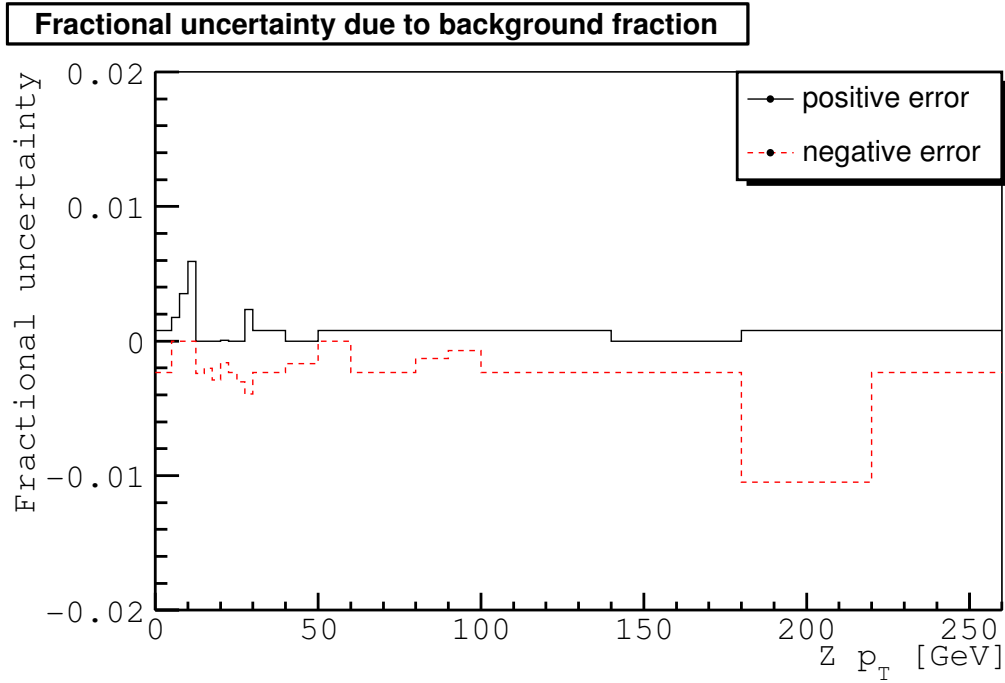


Figure 8.12: Fractional systematic uncertainty on Z boson p_T distribution due to the QCD background.

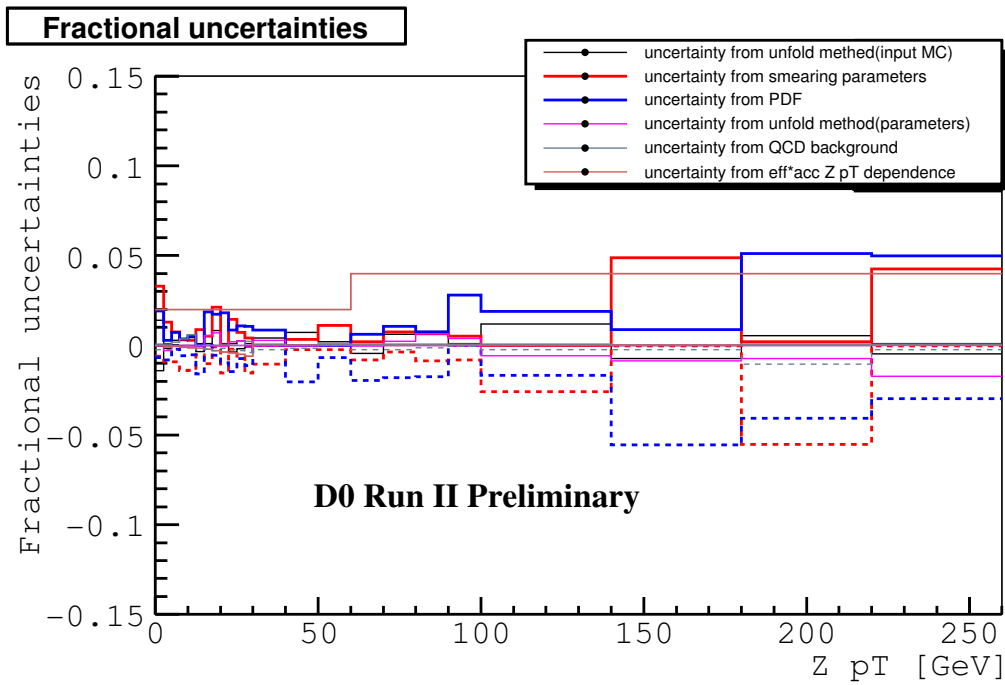


Figure 8.13: Fractional systematic uncertainty on Z boson p_T distribution due to different sources.

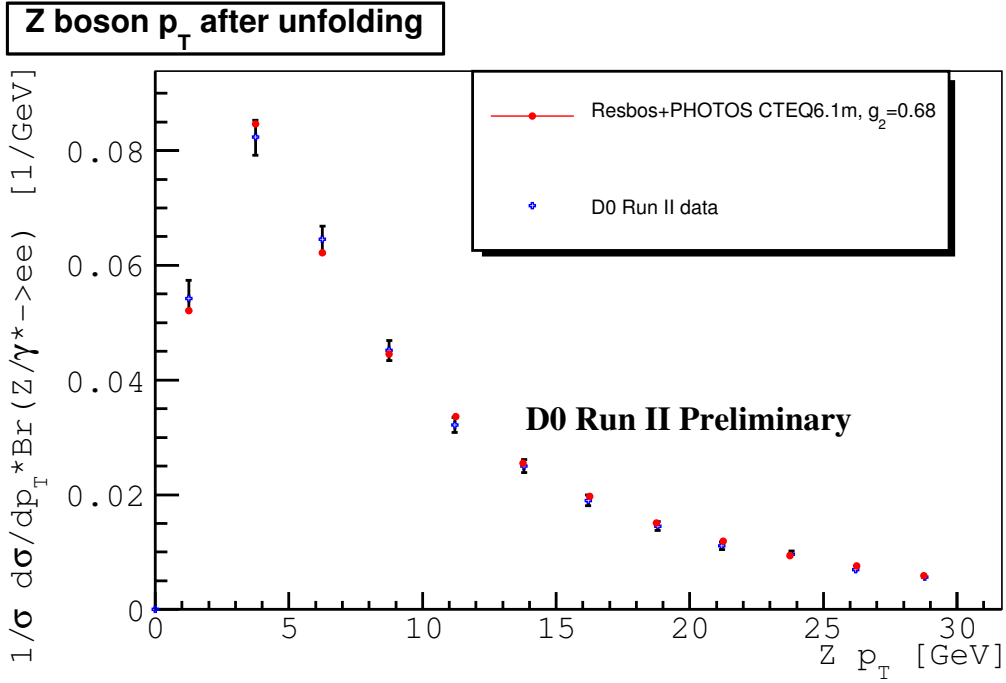


Figure 8.14: Unfolded Z boson p_T distribution. The error contains both statistical and systematic uncertainties.

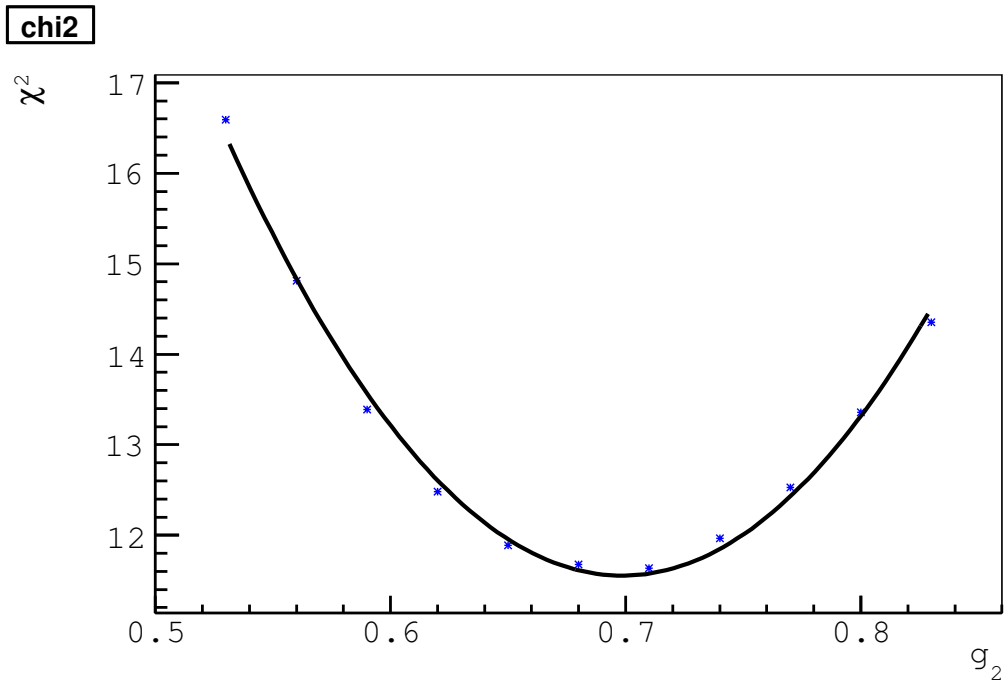


Figure 8.15: Tuning of ResBos g_2 parameter using unfolded $Z p_T$ spectrum.

Run 210993 Evt 55015375

ET scale: 168 GeV

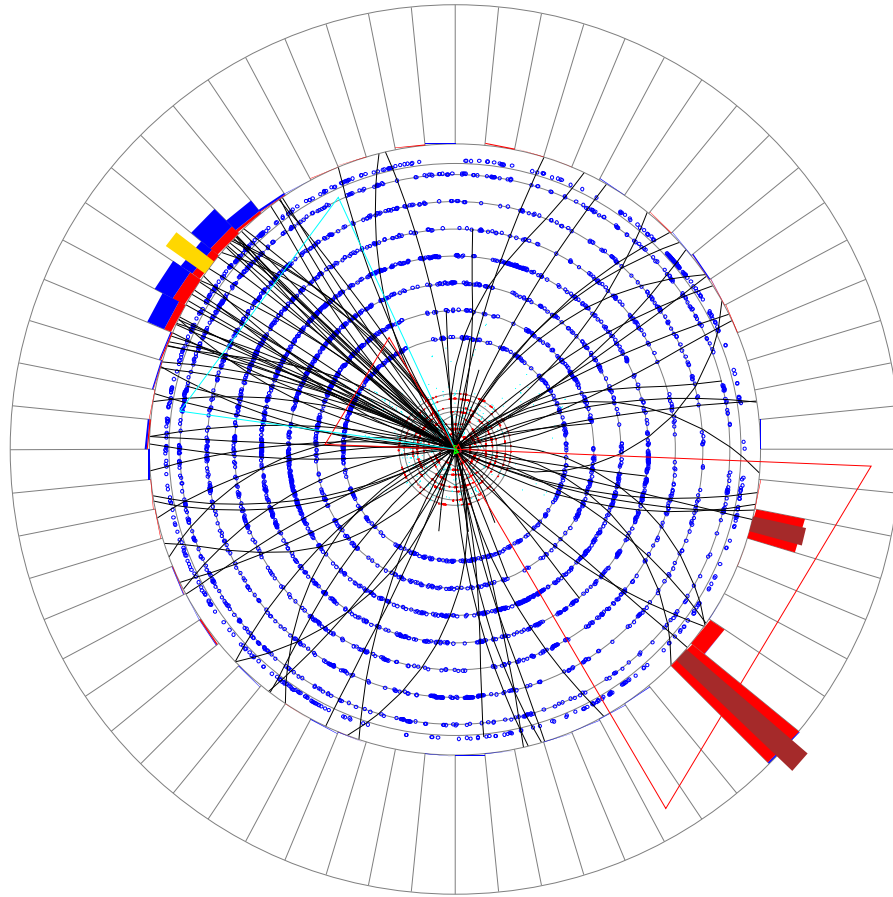


Figure 8.16: Event display for highest $Z p_T$ event. This is the XY view.

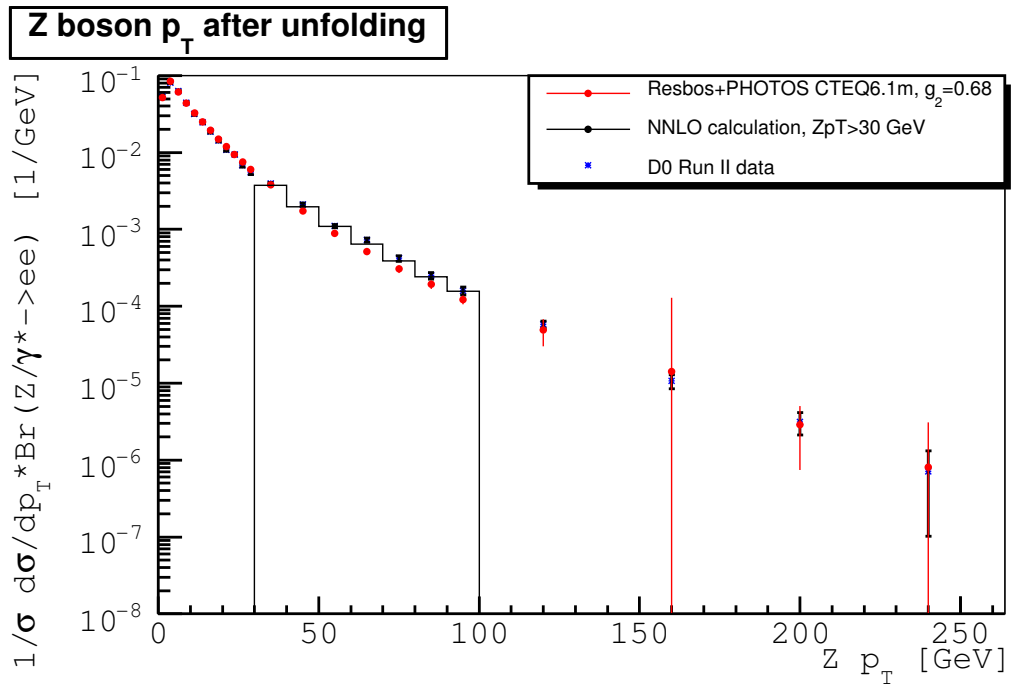


Figure 8.17: Unfolded Z boson p_T distribution. The error contains both statistical and systematic uncertainties.

bin	p_T range[GeV/c]	$\frac{1}{\sigma} \frac{d\sigma}{dp_T}$ [1/GeV/c]	positive δ ($\frac{1}{\sigma} \frac{d\sigma}{dp_T}$) [1/GeV/c]	negative δ ($\frac{1}{\sigma} \frac{d\sigma}{dp_T}$) [1/GeV/c]
1	0-2.5	0.0532	0.0020	0.0030
2	2.5-5.	0.0808	0.0023	0.0023
3	5.0-7.5	0.0633	0.0018	0.0018
4	7.5-10.0	0.0443	0.0014	0.0012
5	10.0-12.5	0.0315	0.0011	0.0010
6	12.5-15.0	0.0246	0.0009	0.0009
7	15.0-17.5	0.0186	0.0007	0.0008
8	17.5-20.0	0.0142	0.0006	0.0007
9	20.0-22.5	0.0109	0.0005	0.0005
10	22.5-25.0	0.0094	0.0004	0.0005
11	25.0-27.5	0.0069	0.0004	0.0004
12	27.5-30.0	0.0055	0.0003	0.0003
13	30.0-40.0	0.0039	0.0001	0.0001
14	40.0-50.0	0.0021	0.0001	0.0001
15	50.0-60.0	0.00110	0.00006	0.00006
16	60.0-70.0	0.00073	0.00005	0.00004
17	70.0-80.0	0.00042	0.00004	0.00004
18	80.0-90.0	0.00025	0.00002	0.00002
19	90.0 -100.0	0.00016	0.00002	0.00002
20	100.0-140.0	0.00006	0.00001	0.00001
21	140.0-180.0	0.000011	0.000002	0.000002
22	180.0-220.0	0.000003	0.000001	0.000001
23	220.0-260.0	0.0000007	0.0000006	0.0000006

Table 8.1: Normalized differential cross section $\frac{1}{\sigma} \frac{d\sigma}{dp_T}$.

bin	1	2	3	4	5	6	7	8	9	10	11	12
1	1	-0.38	0.08	-0.01	0	0	0	0	0	0	0	0
2	-0.38	1	-0.47	0.15	-0.05	0.02	-0.01	0	0	0	0	0
3	0.08	-0.47	1	-0.43	0.12	-0.04	0.01	0	0	0	0	0
4	-0.01	0.15	-0.43	1	-0.40	0.09	-0.01	-0.01	0.01	0	0	0
5	0	-0.05	0.12	-0.40	1	-0.36	0.04	0.03	-0.02	0.01	-0.01	0
6	0	0.02	-0.04	0.09	-0.36	1	-0.33	-0.01	0.06	-0.04	0.02	0
7	0	-0.01	0.01	-0.01	0.04	-0.33	1	-0.28	-0.07	0.10	-0.05	0.01
8	0	0	0	-0.01	0.03	-0.01	-0.28	1	-0.23	-0.15	0.13	-0.05
9	0	0	0	0.01	-0.02	0.06	-0.07	-0.23	1	-0.14	-0.21	0.15
10	0	0	0	0	0.01	-0.04	0.10	-0.15	-0.14	1	-0.12	-0.28
11	0	0	0	0	-0.01	0.02	-0.05	0.13	-0.21	-0.12	1	-0.03
12	0	0	0	0	0	0	0.01	-0.05	0.15	-0.28	-0.03	1

Table 8.2: Error correlation matrix

Chapter 9

Result of Z bosons with rapidity greater than 2.0

As mentioned in the introduction, based on p_T distributions from deep inelastic scattering of electrons on heavy targets, theorists have proposed a modification of the resummation calculation that affects boson produced from partons with small x values. At Tevatron energies, Z bosons with rapidity $|y| > 2.0$ come from quarks in the same x range as those probed by the SIDIS experiments. In this section, I compare the p_T spectrum for Z bosons at large rapidity to the theoretical calculation with and without the small- x modification.

In this analysis, 5412 $Z/\gamma^* \rightarrow e^+e^-$ events have $y > 2$, including 5143 ECEC events and 269 CCEC events. The raw p_T spectrum after the event selection is presented in Fig. 9.1.

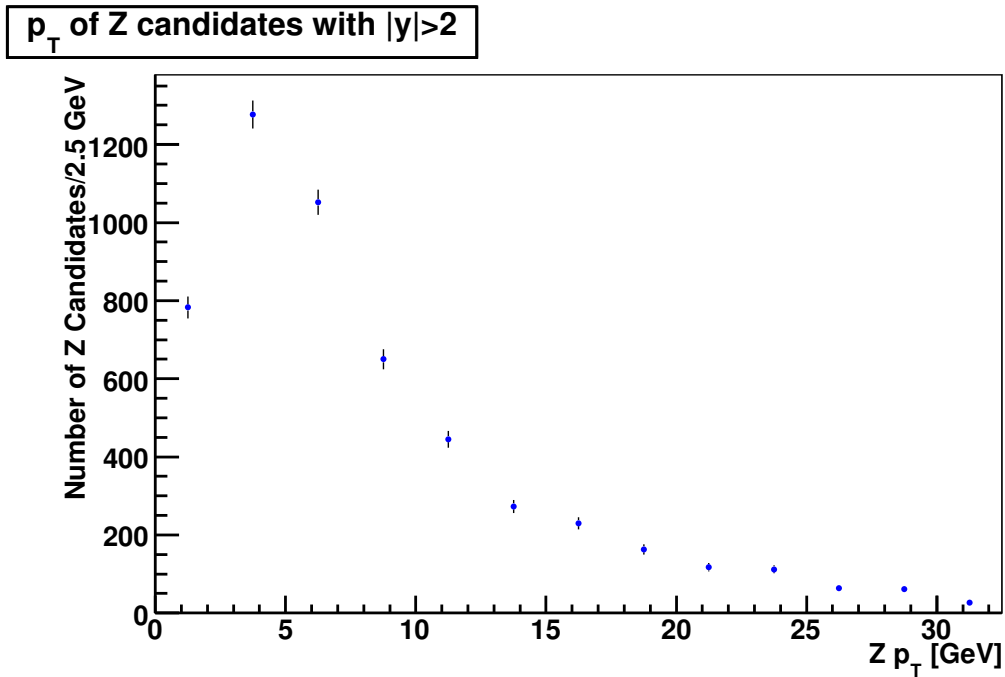


Figure 9.1: p_T distribution for Z candidates with $|y| > 2$.

The background fraction is determined using the same method used in Chapter 6 to be

$4.0 \pm 0.1\%$. The best result of the minimum χ^2 fit is presented in Fig. 9.2.

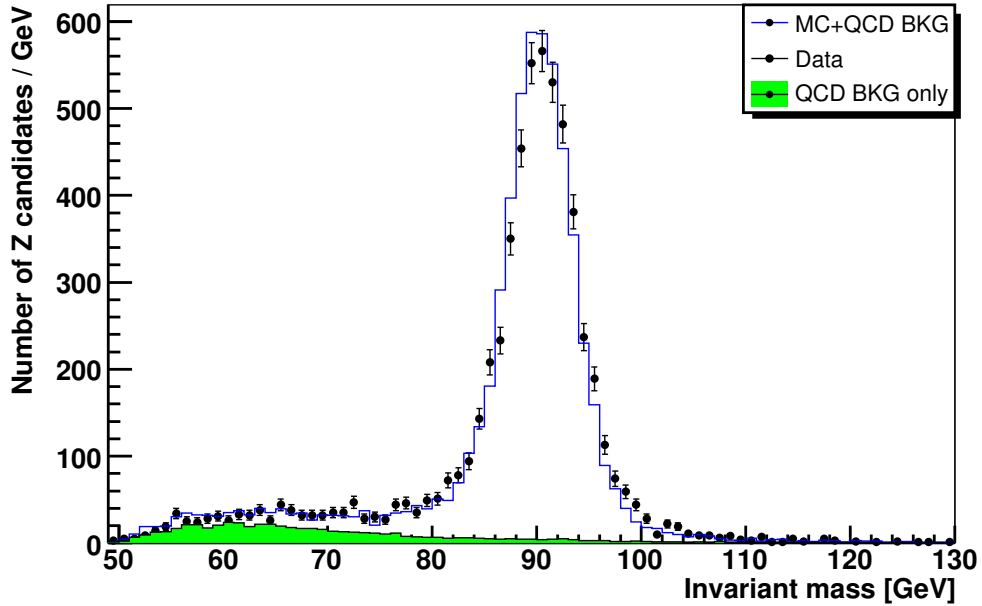


Figure 9.2: Invariant mass distribution for Z candidates with $|y| > 2$.

The $Z p_T$ dependence of the efficiency is determined from full Monte Carlo $Z/\gamma^* \rightarrow e^+e^-$ events containing Z s with $y > 2$ and is presented in Fig. 9.3. The dependence of the acceptance on $Z p_T$ is also determined using PMCS for Z s with $|y| > 2$, and is presented in Fig. 9.4. The $\text{efficiency} \times \text{acceptance}(Z p_T)$ is presented in Fig. 9.5.

The unfolded result for Z 's with rapidity greater than 2.0 is shown in Fig. 9.6 with statistical errors only.

The systematic uncertainties are estimated using the same methods that were used for the all y result. Including the systematic uncertainty, the final result for $|y| > 2$ is presented in Fig. 9.7, as well as the ResBos distributions with and without the small- x correction, with χ^2/ndf to be 31.9/12 and 11.1/12, respectively. Thus, in our analysis we do not observe the small- x broadening effect predicted by [4]

Finally, we overlay the all y and $|y| > 2$ $Z p_T$ spectrum together, in Fig. 9.8.

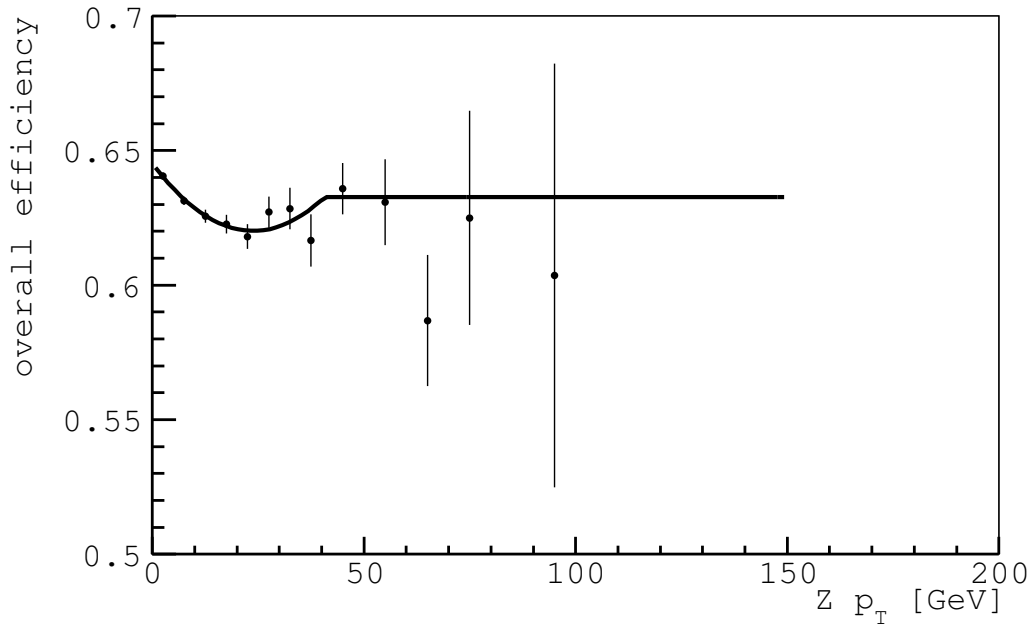


Figure 9.3: Efficiency($Z p_T$) distribution for Z candidates with $|y| > 2$.

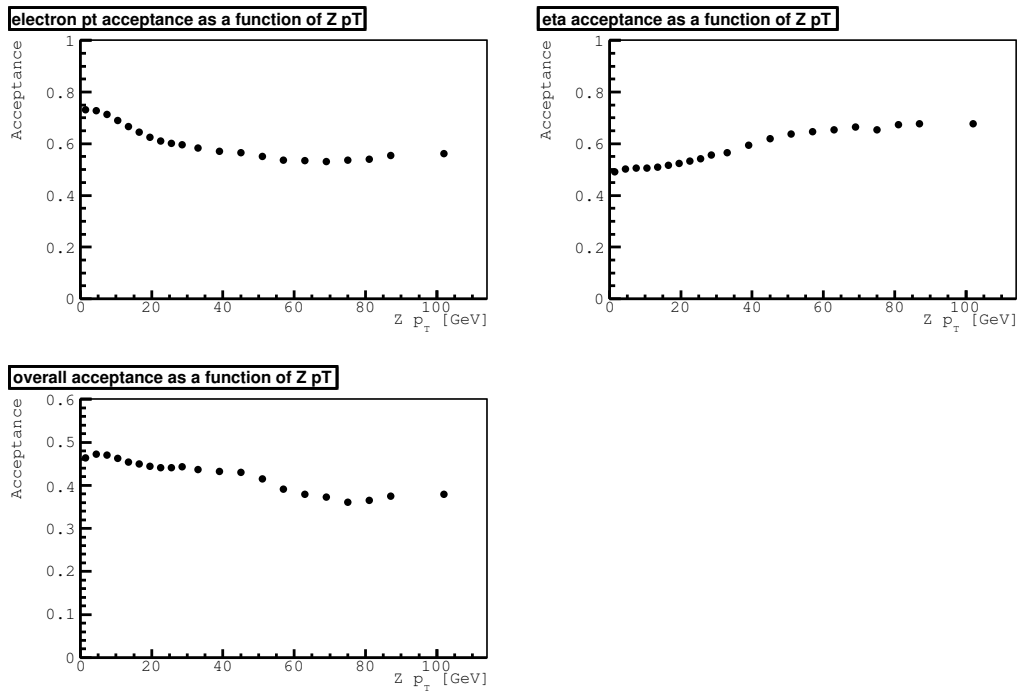


Figure 9.4: Acceptance($Z p_T$) distribution for Z candidates with $|y| > 2$.

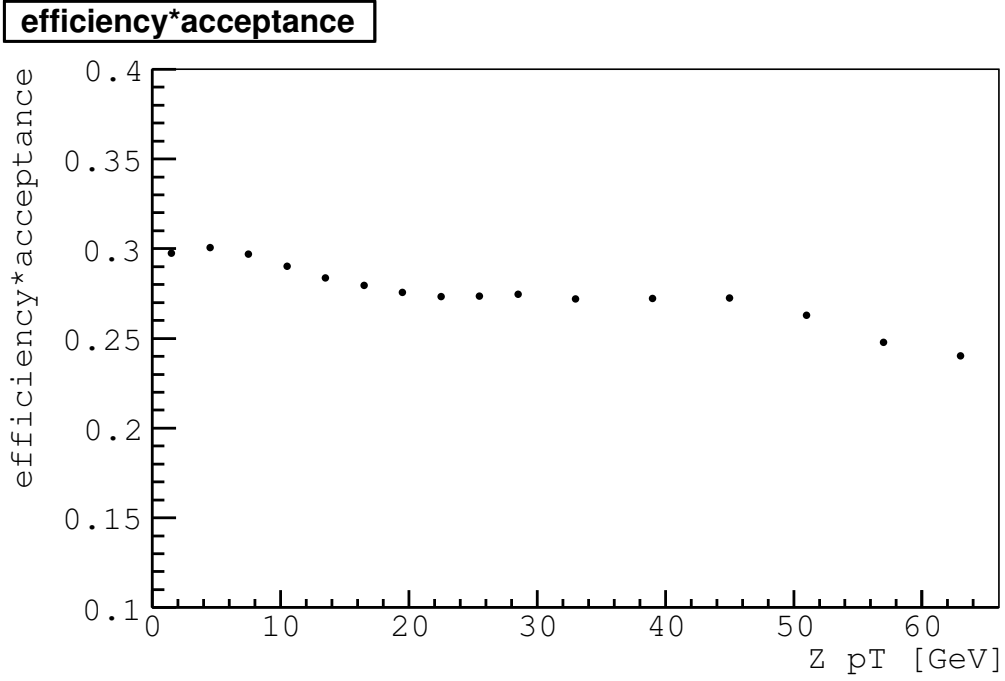


Figure 9.5: Efficiency*Acceptance($Z p_T$) distribution for Z candidates with $|y| > 2$.

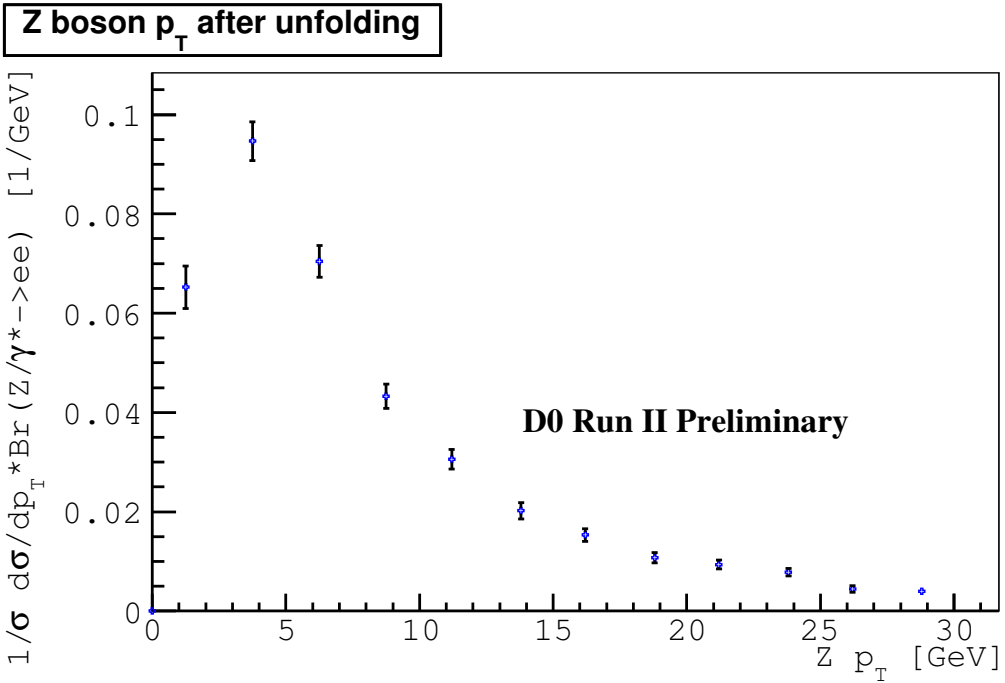


Figure 9.6: Unfolded $Z p_T$ distribution for Z candidates with $|y| > 2$. The errors are statistical errors only.

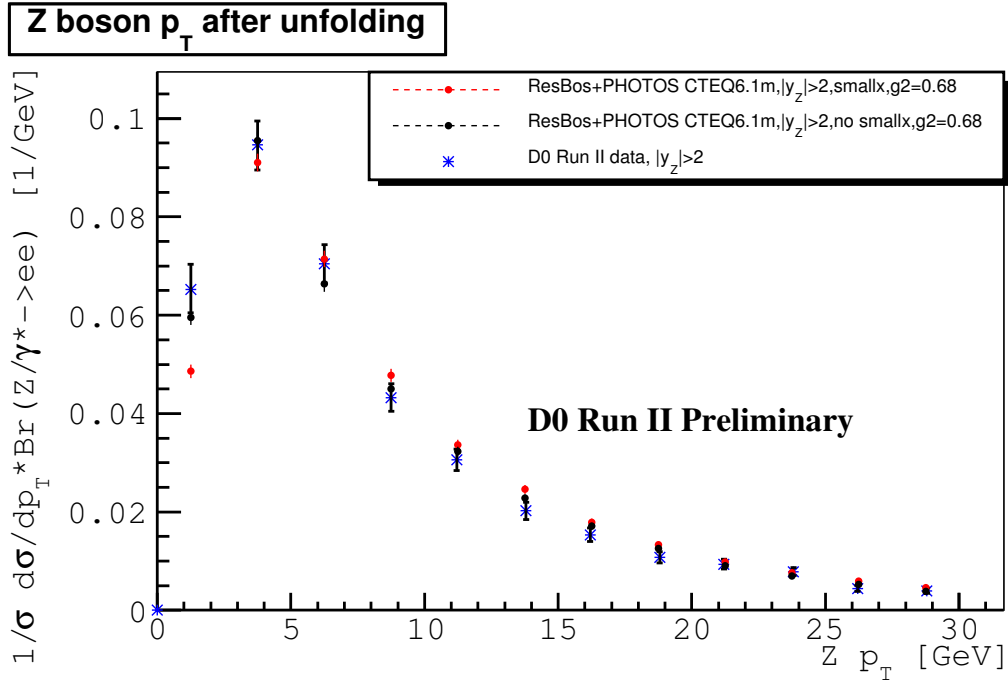


Figure 9.7: Unfolded $Z p_T$ distribution for Z candidates with $|y| > 2$.

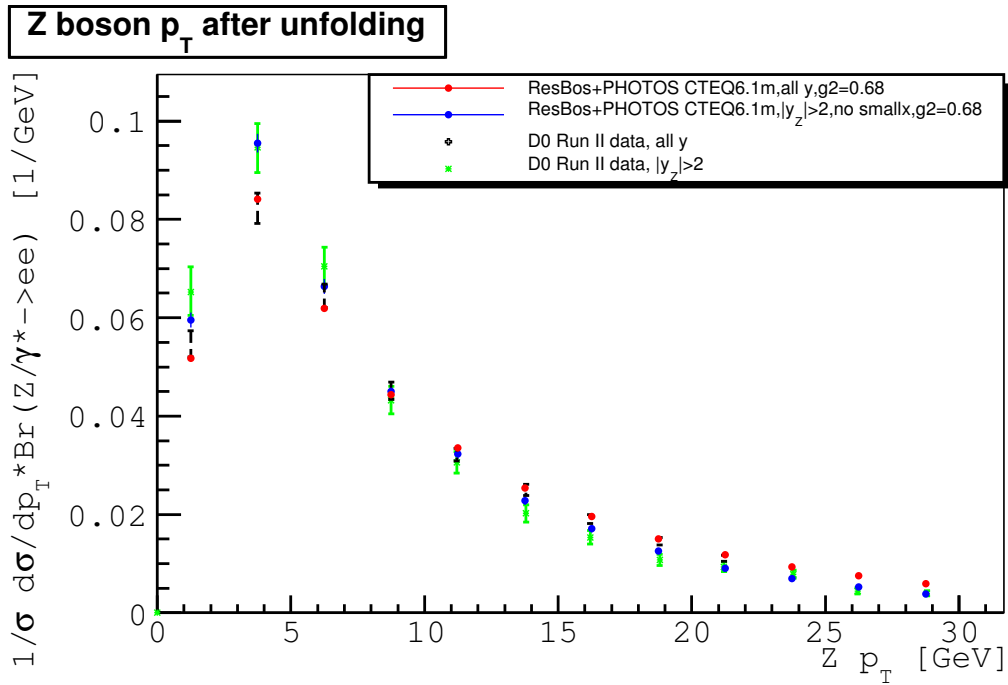


Figure 9.8: Comparison of unfolded $Z p_T$ distributions for Z candidates with $|y| > 2$ and all y .

Chapter 10

Closure tests

10.1 Full Monte Carlo Test For All y Region

To verify the efficacy of the unfolding process I used, I did a closure test using full Monte Carlo samples. The idea is to treat the reconstructed full Monte Carlo events as “data”, and check that the unfolded spectrum is the same as the PYTHIA generator spectrum.

I used the same selections to select good events. I measured the efficiencies and tuned the smearing parameters using the full Monte Carlo events, then put them into PMCS. The “Monte Carlo” inputs to the unfold program are the generator level(ResBos+PHOTOS) and its PMCS smeared $Z p_T$ ntuples. To correct for the effect of selection on the observed $Z p_T$, I measure the acceptance ($Z p_T$) using PMCS (shown in Fig. 10.1). The efficiency($Z p_T$) was presented previously in Fig. 7.4. The efficiency \times acceptance($Z p_T$) is presented in Fig. 10.2.

I also compare the invariant mass distributions from full Monte Carlo and PMCS, shown in Fig. 10.3 and 10.4.

Finally, the unfolded spectrum is compared with the PYTHIA generator $Z p_T$ spectrum of the full MC, presented in Fig. 10.5. The $Z p_T$ distribution from ResBos, which is used as the input to the unfold program, is also plotted in the same figure. The χ^2 test of the unfolded spectrum and the PYTHIA spectrum is $\chi^2/\text{ndf}=13.0/12$: it is a good agreement. In Fig. 10.6, I plotted the difference between the unfolded result and PYTHIA. The χ^2 test of the histogram with zero is $\chi^2/\text{ndf}=19.0/12$.

10.2 Full Monte Carlo Test For Z s with $y > 2$

We also did the full Monte Carlo closure test for Z s with $|y| > 2$. The efficiency($Z p_T$) and acceptance($Z p_T$) for these events are plotted in Fig. 10.7 and Fig. 10.8. The

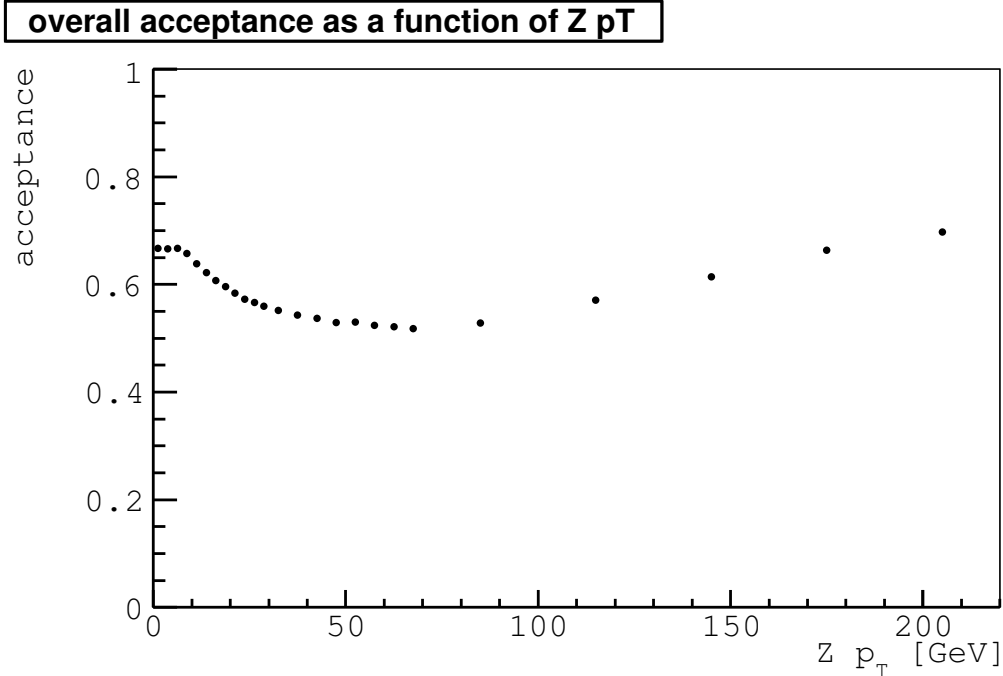


Figure 10.1: Acceptance $Z p_T$ dependence for the full Monte Carlo $Z/\gamma^* \rightarrow e^+e^-$ sample

Efficiency \times Acceptance($Z p_T$) is presented in Fig. 10.9. The comparison between unfolded result and the PYTHIA generator is in Fig. 10.10, the χ^2 test between the two histograms is $\chi^2/\text{ndf}=10.0/12$.

10.3 Test For Z s with $0.5 < y < 2$

There have been many analysis done using the central EM calorimeter at DØ Run II. But few of them used the endcap calorimeters. To test the small- x broadening effect at high Z rapidity predicted by theorists, in this analysis we used the endcap EM calorimeters. We need to make sure that we have a good knowledge of the endcap calorimeter energy smearing. We design a test by looking at $0.5 < |y_Z| < 2$ events. For these selected Z events, we look at CC-CC and CC-EC events. We unfold both of them and expect the unfolded spectra to be the same because there is no smearing effect left after unfolding and they have the same Z rapidity range.

Fig. 10.11 shows the efficiency($Z p_T$) for CC-CC and CC-EC events with Z rapidity between 0.5

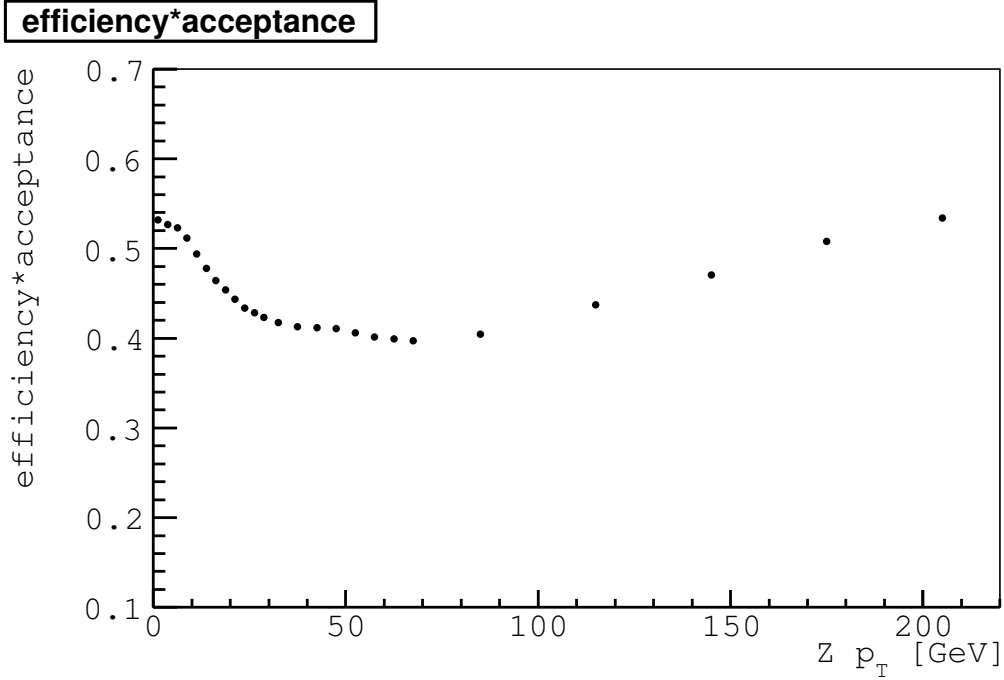


Figure 10.2: Efficiency*Acceptance $Z p_T$ dependence for the full Monte Carlo $Z/\gamma^* \rightarrow e^+e^-$ sample

and 2. Fig. 10.12 shows the acceptance($Z p_T$) for CC-CC and CC-EC same events.

Efficiency \times Acceptance($Z p_T$) for them are presented in Fig. 10.13.

Fig. 10.14 shows the raw $Z p_T$ distribution for CC-CC and CC-EC; their shapes are different due to different detector smearing and the χ^2 test between them is $\chi^2/\text{ndf}=26/12$. Fig. 10.15 shows the unfolded CC-CC and CC-EC $Z p_T$ distribution. With a $\chi^2/\text{ndf}=11/12$, they are in good agreement with each other, which is consistent with our expectation.

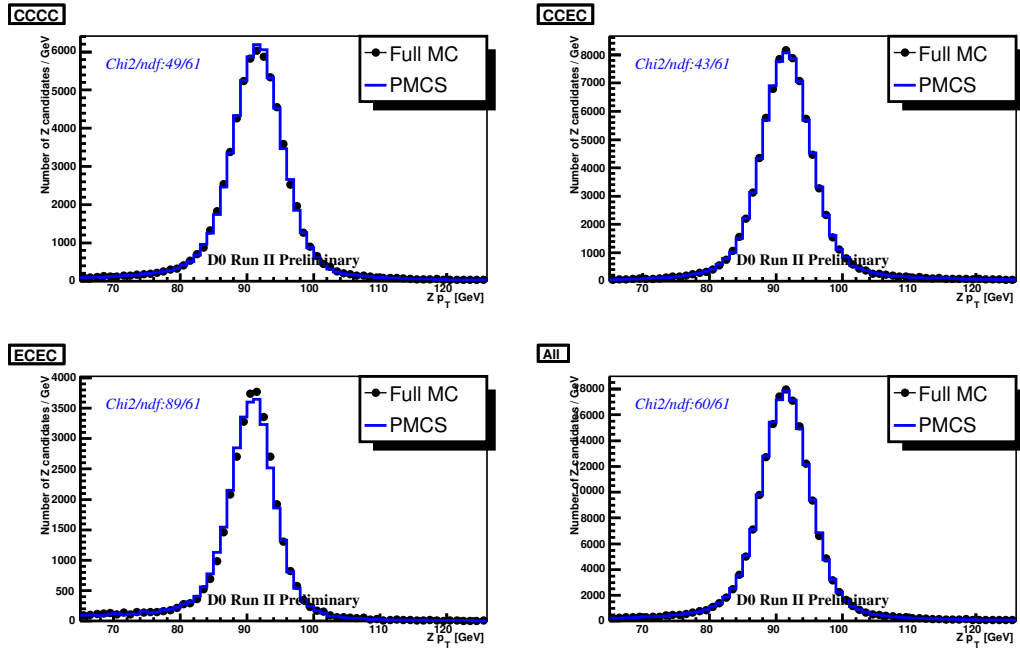


Figure 10.3: Comparison of invariant mass distribution for the full Monte Carlo $Z/\gamma^* \rightarrow e^+e^-$ sample, linear scale

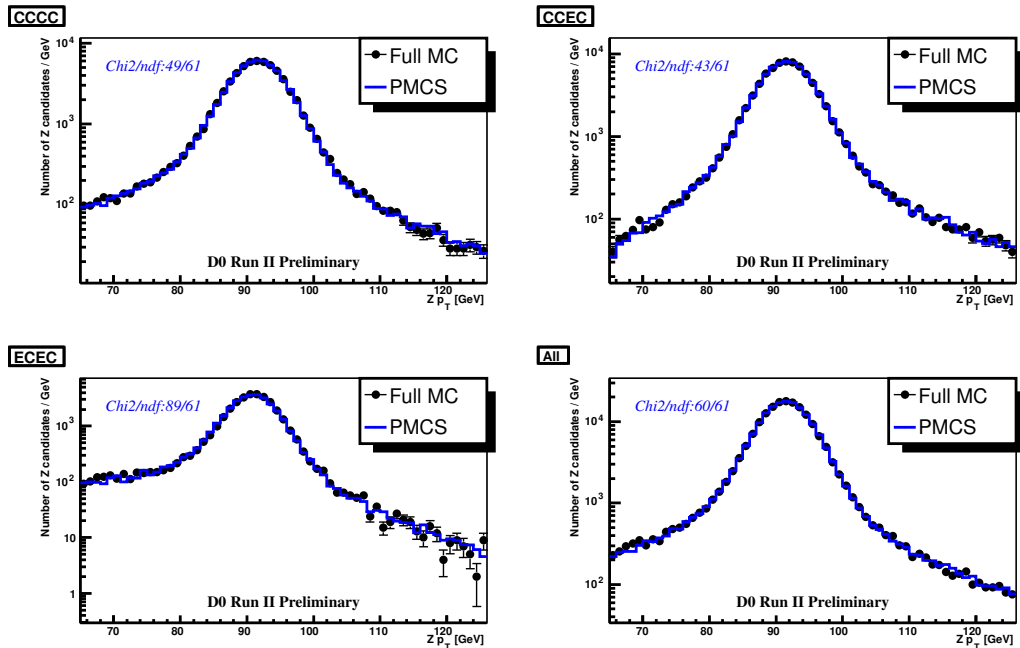


Figure 10.4: Comparison of invariant mass distribution for the full Monte Carlo $Z/\gamma^* \rightarrow e^+e^-$ sample, log scale

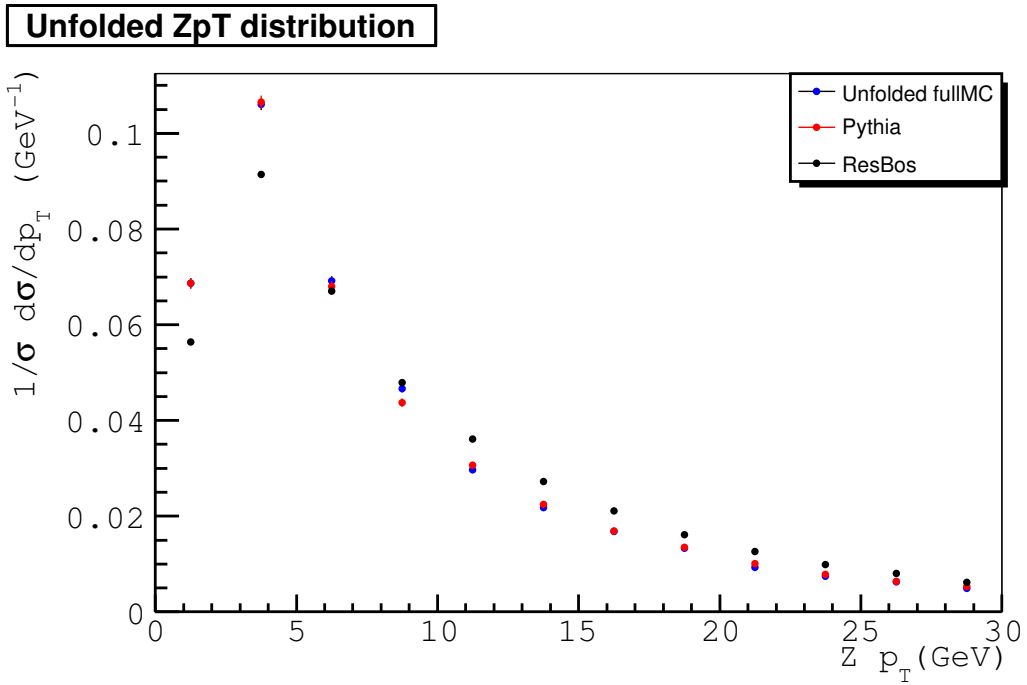


Figure 10.5: Comparison of the $Z \, p_T$ distributions for the unfold data and the PYTHIA generator in the full Monte Carlo closure test

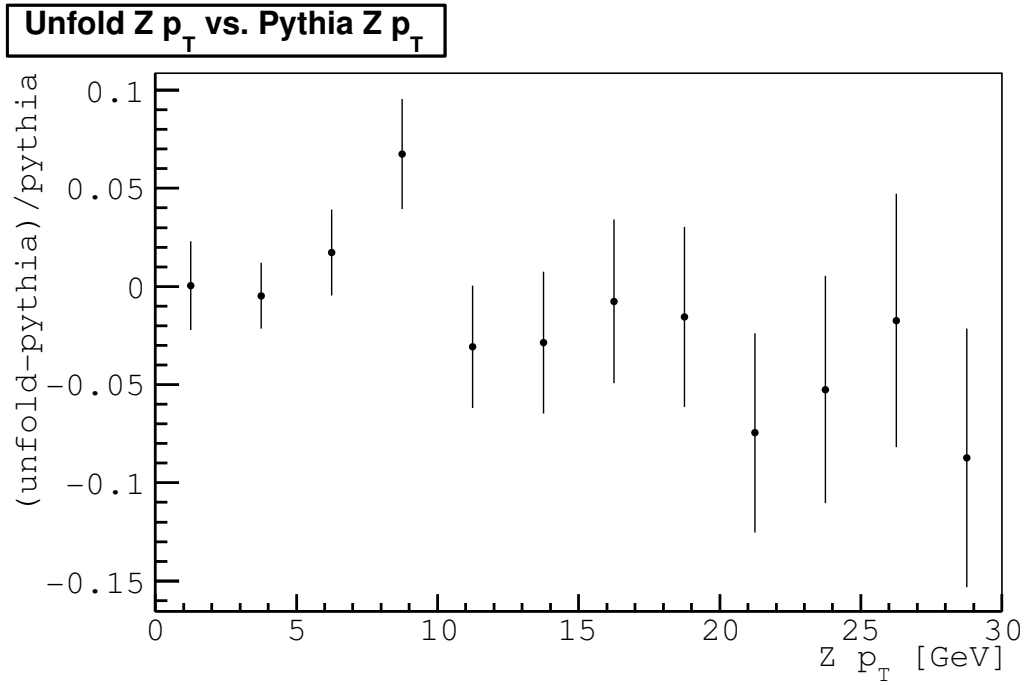


Figure 10.6: Difference between the $Z p_T$ distributions for the unfold data and the PYTHIA generator in the full Monte Carlo closure test

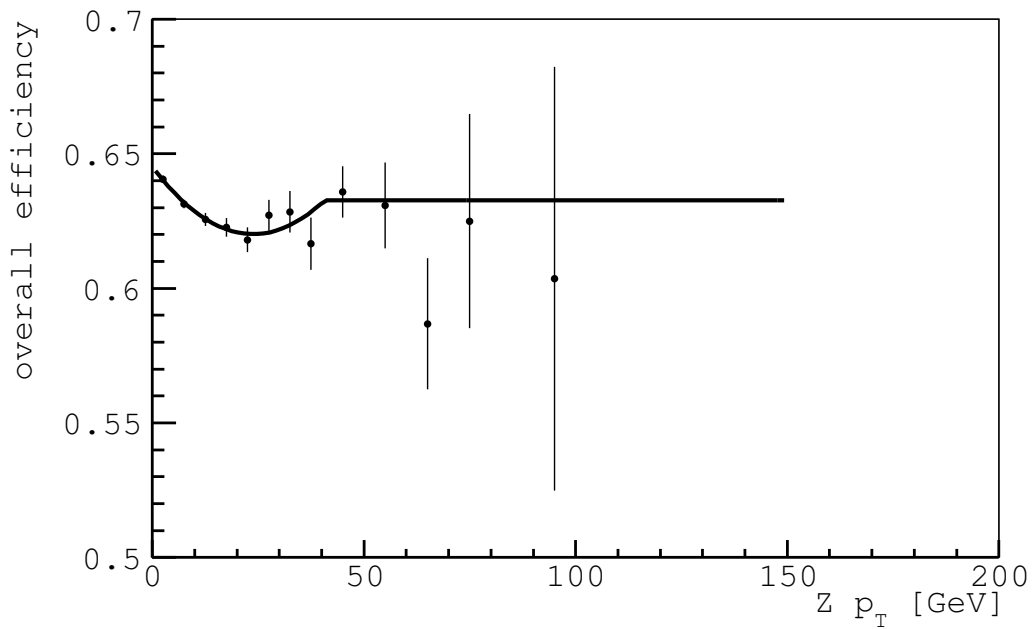


Figure 10.7: Efficiency $Z p_T$ dependence for the full Monte Carlo $Z/\gamma^* \rightarrow e^+e^- |y| > 2$ sample.

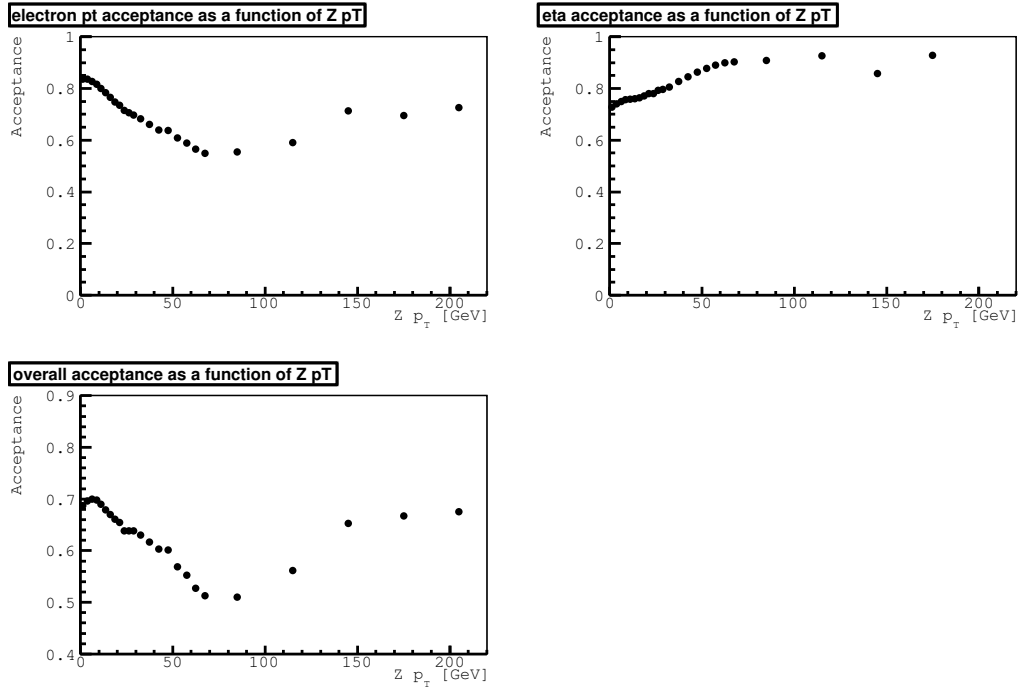


Figure 10.8: Acceptance $Z p_T$ dependence for the full Monte Carlo $Z/\gamma^* \rightarrow e^+e^- |y| > 2$ sample.

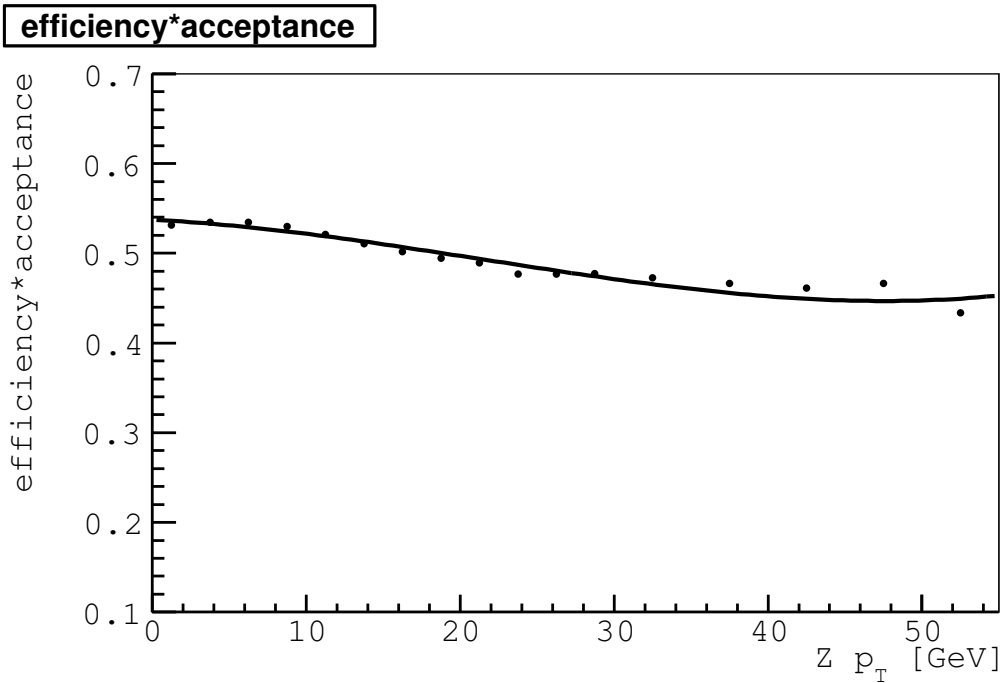


Figure 10.9: Efficiency \times Acceptance $Z p_T$ dependence for the full Monte Carlo $Z/\gamma^* \rightarrow e^+e^- |y| > 2$ sample.

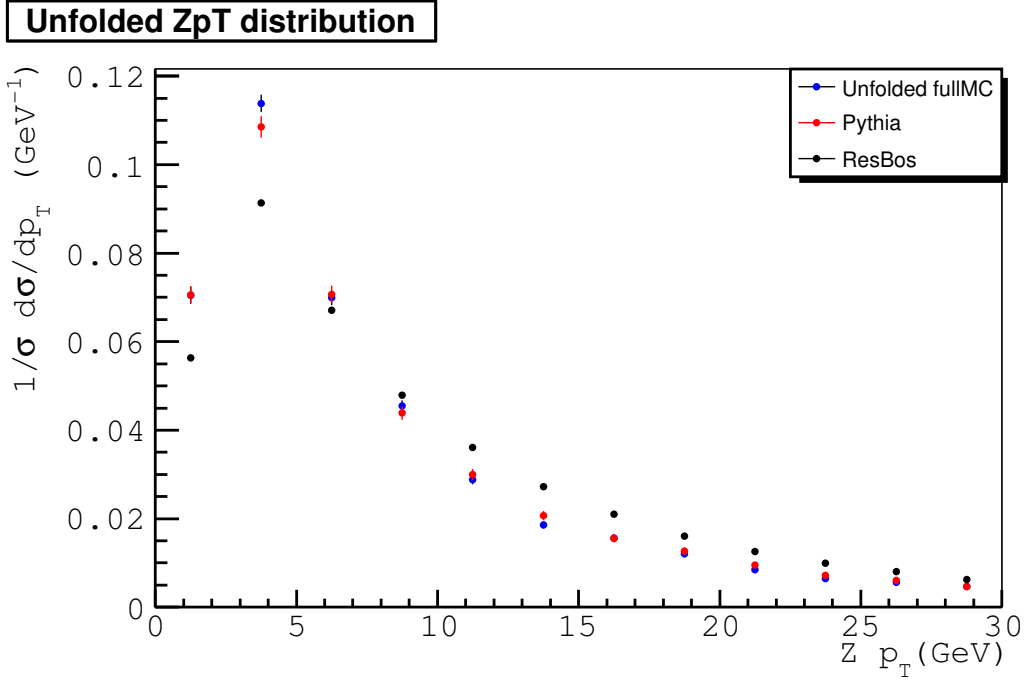


Figure 10.10: Comparison of the $Z p_T$ distributions for the unfold data and the PYTHIA generator in the full Monte Carlo $|y| > 2$ closure test.

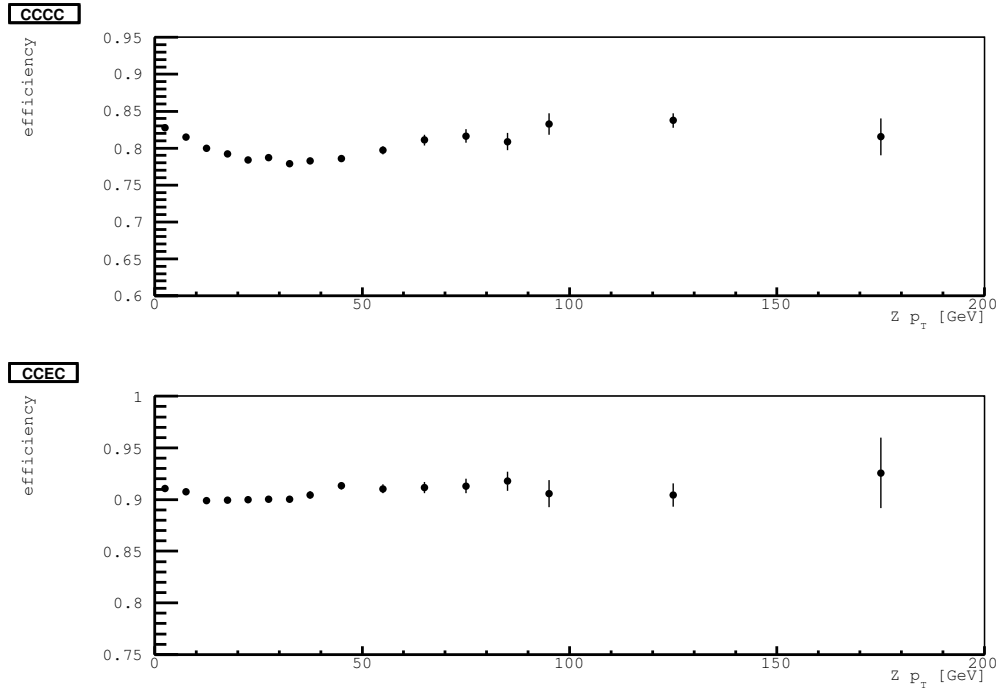


Figure 10.11: Efficiency $Z p_T$ dependence for the $Z/\gamma^* \rightarrow e^+e^-$ $0.5 < |y| < 2$ sample.

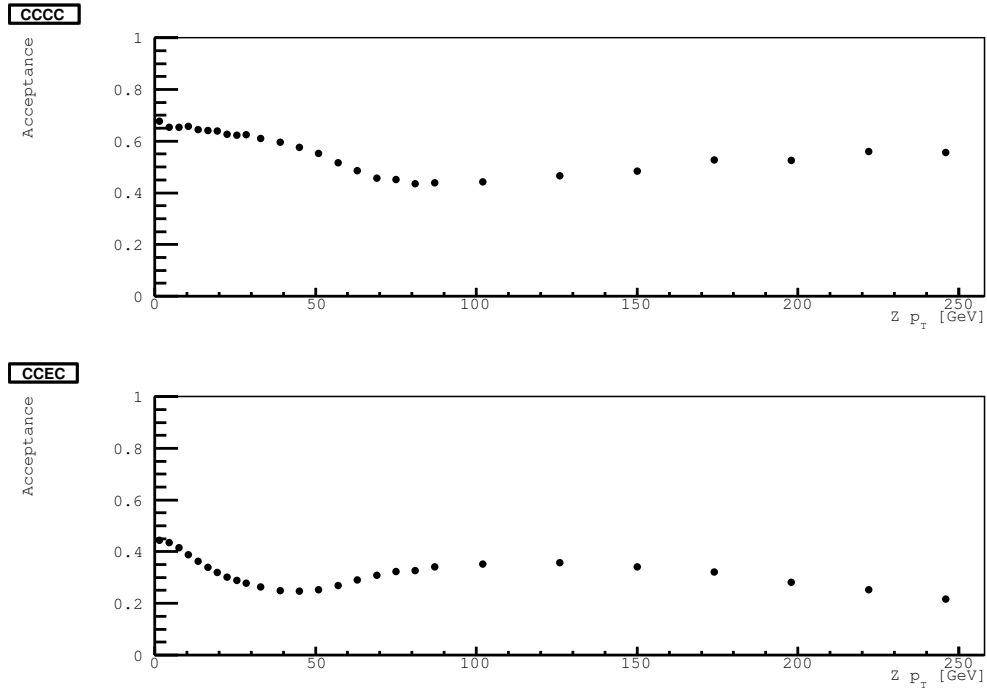


Figure 10.12: Acceptance $Z p_T$ dependence for the $Z/\gamma^* \rightarrow e^+e^-$ $0.5 < |y| < 2$ sample.

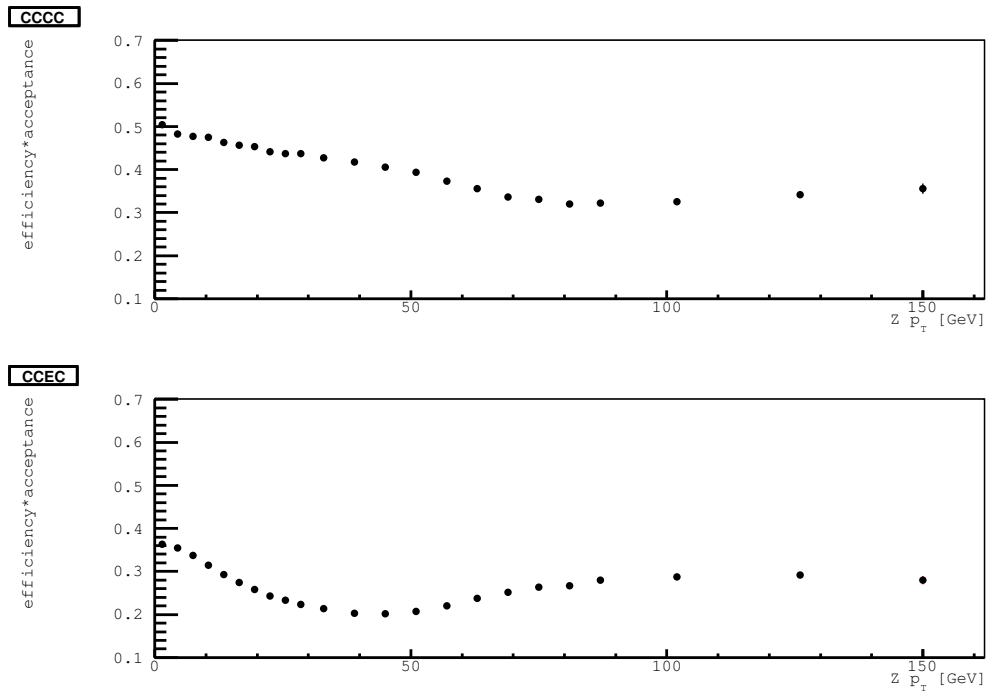


Figure 10.13: Efficiency \times Acceptance $Z p_T$ dependence for the $Z/\gamma^* \rightarrow e^+e^-$ $0.5 < |y| < 2$ sample.

measured ZpT distribution

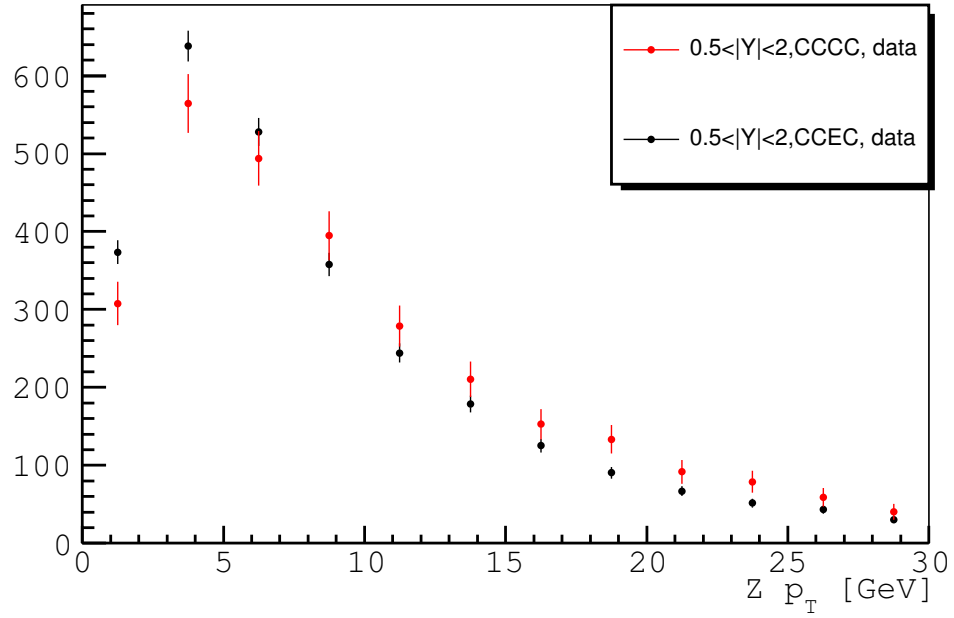


Figure 10.14: Raw $Z p_T$ distribution for CC-CC, CC-EC $0.5 < |y| < 2$ sample.

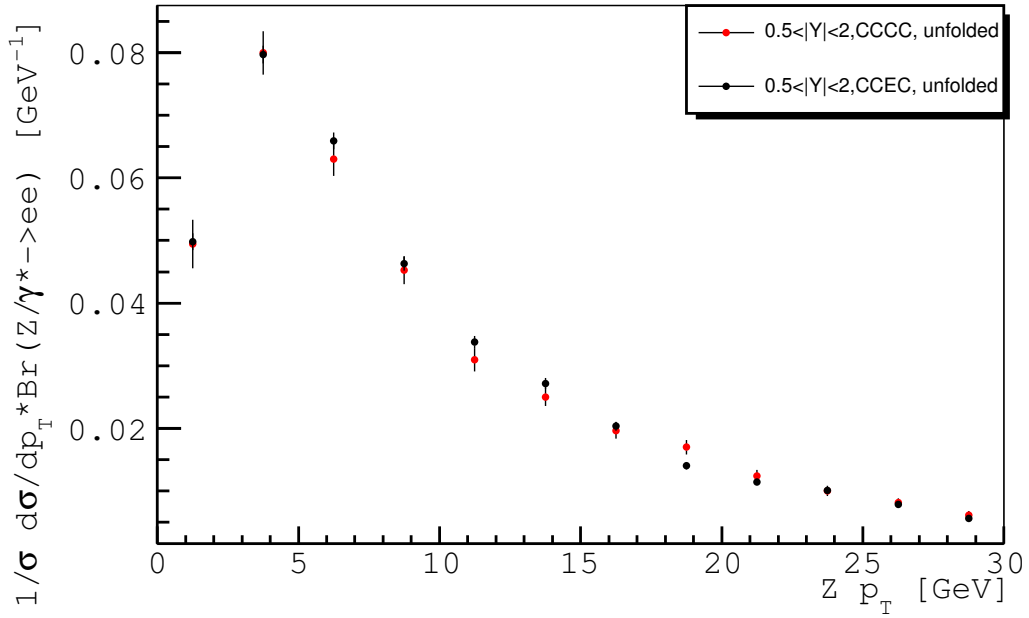


Figure 10.15: Unfolded $Z p_T$ distribution for CC-CC, CC-EC $0.5 < |y| < 2$ sample.

Chapter 11

Conclusions

A total of 63,656 $Z/\gamma^* \rightarrow e^+e^-$ events are selected from the 976 pb⁻¹ data sample collected between October 2002 and November 2005 at the DØ detector. With these events, I measured the differential cross section $\frac{1}{\sigma} \frac{d\sigma}{dq_T}$ for Z events produced in $p\bar{p}$ collisions at a center-of-mass energy of 1.96 TeV at the Tevatron Run II.

I unfolded the detector smearing effect and compared the unfolded spectrum with the theory calculations. At the low p_T region, I compared our result with the CSS resummation calculation and found very good agreements. I also fit the g_2 parameter in the Ladinsky-Yuan parameterization of the Sudakov factor, the fitted g_2 parameter is 0.70 ± 0.05 GeV², with $g_1 = 0.21$ GeV², $g_3 = -0.6$ GeV⁻¹. At the high p_T region, I compared our spectrum with NNLO calculation and found very good agreements.

In this thesis, I also performed a measurement of the differential cross section $\frac{1}{\sigma} \frac{d\sigma}{dq_T}$ for Z events with a rapidity y greater than 2.0. These bosons are produced from a small- x quark and as a recent paper[4] predicted, the p_T spectrum for them should be broader than the traditional CSS resummation. However, our result is in better agreement with the traditional CSS resummation rather than the calculation with the small- x correction implemented.

BIBLIOGRAPHY

- [1] J. Collins, D. Soper, G. Sterman, Nucl. Phys. B250 (1985) 199.
- [2] P. Nadolsky, D.R. Stump, and C.-P. Yuan, Phys. Rev. D **61**, 014003 (2000) [Erratum-ibid. D **64**, 059903 (2001)].
- [3] P.M. Nadolsky, D.R. Stump, and C.-P. Yuan, Phys. Rev. D **64**, 114011 (2001).
- [4] Stefan Berge, Pavel Nadolsky, Fredrick Olness, C.-P. Yuan, Phys. Rev. D **72**, 033015 (2005).
- [5] C. Balazs, C.P. Yuan, Soft gluon effects on lepton pairs at hadron colliders, Phys.Rev.D56:5558-5583,1997
- [6] DØ Collaboration, B. Abbot *et al.*, Phys. Rev. D **61**, 032004 (2000).
- [7] CDF Collaboration, T. Affolder *et al.*, Phys. Rev. Lett. **84**, 845 (2000).
- [8] Wilczek, Frank ; Quantum Field Theory, Review of Modern Physics 71 (1999) S85-S95.
- [9] S.L. Glashow, Nucl. Phys. **B22** 579 (1961); A. Salam and J.C. Ward, Phys. Rev. Lett. **13** 168 (1994); S. Weinberg, Phys. Rev. Lett. **19** 1264 (1967).
- [10] G. Arnison *et al.* (UA1 Collaboration), Phys. Lett. **B122** 102 (1983); M. Banner *et al.* (UA2 Collaboration), Phys. Lett. **B122** 476 (1983).
- [11] A.H. Mueller(editor), Perturbative Quantum Chromodynamics, (Singapore, World Scientific, Advanced Series on Directions in High Energy Physics v5, 1989)
- [12] P.B. Arnold and R.P. Kaufman, Nucl. Phys. B349, 381(1991). J. Collins, D. Soper, G. Sterman, Nucl. Phys. B250 (1985) 199.
- [13] C. Balazs, C.P. Yuan, Soft gluon effects on lepton pairs at hadron colliders, Phys.Rev.D56:5558-5583,1997 G.A. Ladinsky, C.-P. Yuan, Phys. Rev. D50 (1994) 4239.
- [14] F. Landry, R. Brock*, P. M. Nadolsky, and C.-P. Yuan, Fermilab Tevatron run-1 Z boson data and the Collins-Soper-Sterman resummation formalism, Phys. Rev. D 67, 073016 (2003).

- [15] J. Thompson, “Introduction to Colliding Beams at Fermilab”, FERMILAB-TM-1909 (1994); Run II Handbook, <http://www-bd.fnal.gov/runII/>; Accelerator Concepts, V3.0 (2002).
- [16] S. Abachi *et al.* (DØ Collaboration), The Upgraded D0 Detector, Nucl.Instrum.Meth. A565 (2006)
- [17] S. Abachi *et al.* (DØ Collaboration), Nucl. Instr. and Methods, **A338**, 185 (1994).
- [18] S. Abachi *et al.* (DØ Collaboration), Phys. Rev. Lett. **74**, 2632 (1995); F. Abe *et al.* (CDF Collaboration), Phys. Rev. Lett. **74**, 2626 (1995).
- [19] DØ Collaboration, DØ Note **1996**, “The DØ Upgrade: The Detector and Its Physics”; V. Abazov *et al.* (DØ Collaboration), in preparation for submission to Nucl. Instr. and Methods.
- [20] DØ Upgrade Collaboration, “DØ Silicon Tracker Technical Design Report”, <http://www-d0.fnal.gov/trigger/stt/smt/smt.tdr.ps>.
- [21] DØ Collaboration, DØ Note **4164**, “Central Fiber Tracker Technical Design Report”.
- [22] DØ Collaboration, DØ Note **3014**, “Design Report of the Central Preshower Detector for the DØ Upgrade”.
- [23] DØ Collaboration, DØ Note **2894**, “The DØ Upgrade: Forward Preshower, Muon System and Level 2 Trigger”.
- [24] S. Abachi *et al.* (DØ Collaboration), Nucl. Instr. and Methods, **A324**, 53 (1993).
- [25] L. Groer, DØ Note **4240**, “DØ Calorimeter Upgrades for Tevatron Run II”.
- [26] DØ Collaboration, “Calorimeter Electronics”, <http://www-d0.fnal.gov/hardware/cal>.
- [27] R. Zitoun, DØ Note **3997**, “Study of the Non Linearity of the DØ Calorimeter Readout Chain”; J. Kotcher, “Upgrade Plans for the DØ Calorimeter”; J. Kourlas, “Calorimeter Electronics for the DØ Upgrade”.
- [28] Q. Zhu, Ph.D. thesis, New York University, 1994, “Measurement of the W Boson Mass in Proton-Antiproton Collisions at $\sqrt{s} = 1.8$ TeV” (unpublished).

- [29] T.C. Heuring, Ph.D. thesis, State University of New York at Stony Brook, 1993, “Electrons in the DØ Calorimeter: A Study of the Systematic Biases in the Measurement of the W Mass” (unpublished).
- [30] B. Abbott *et al.* (DØ Collaboration), Phys. Rev. Lett. **80** (1998); B. Abbott *et al.* (DØ Collaboration), Phys. Rev. **D58** (1998); B. Abbott *et al.* (DØ Collaboration), Phys. Rev. Lett. **84** (2000); B. Abbott *et al.* (DØ Collaboration), Phys. Rev. **D62** (2000); V. Abazov *et al.* (DØ Collaboration), Phys. Rev. **D66** (2002).
- [31] C. Brown *et al.* (DØ Collaboration), Nucl. Instr. and Methods, **A279** 331 (1989).
- [32] DØ Collaboration, “DØ Run II Level 1 Trigger Framework Technical Design Report”, http://www.pa.msu.edu/hep/d0/ftp/l1/framework/l1fw_tdr_05june98.txt.
- [33] D. Edmunds *et al.*, DØ Note **3402**, “Technical Design Report for the Level 2 Global Processor”.
- [34] DØ Collaboration, DØ Note **3266**, “Description of DØ L3 Trigger Software”.
- [35] M. Adams *et al.*, DØ Note **3651**, “Level 2 Calorimeter Preprocessor Technical Design Report”.
- [36] DØ Integrated Luminosity: <http://www-d0.fnal.gov/runcoor/runplans/runplan.html#plots>;
Tevatron Integrated Luminosity: http://www-d0.fnal.gov/runcoor/RUN/run2_lumi.html.
- [37] http://www-d0.fnal.gov//computing/data_quality/d0_private/
- [38] <http://www-d0.fnal.gov/computing/algorithms/status/index.html>
- [39] D. Adams, Finding Tracks, DØ note 2958.
- [40] http://www-d0.fnal.gov/trigger/stt/doc/svtstat_970307/svtbeam.html.
- [41] D. Chapin *et al.*, DØ Note **4403**, “Measurement of $Z/\gamma^* \rightarrow e^+e^-$ and $W \rightarrow e\nu$ Production Cross Sections with $|\eta| < 2.3$ ”.

- [42] A. Schwartzman and M. Narain, DØ Note 3907, “Primary Vertex Selection”.
- [43] Doug Chapin *et al.*, Measurement of $Z \rightarrow ee$ and $W \rightarrow e\nu$ Production Cross Sections Using One Tight Central Electron, DØ note 4897, 2005
- [44] Application Software Group, “GEANT: Detector Description and Simulation Tool”, CERN Program Library Long Writeup W5013, <http://wwwasd.web.cern.ch/wwwasd/geant/>.
- [45] http://www-d0.fnal.gov/phys_id/emid/d0_private/emid_intro.html
- [46] http://www-d0.fnal.gov/phys_id/emid/d0_private/certification/main_v5_0.html
- [47] <http://www-d0.fnal.gov/computing/MonteCarlo/MonteCarlo.html>
- [48] DØ Collaboration, S. Abachi *et al.*, Nucl. Instrum. Methods, Phys. Res. A 338, 185 (1994).
- [49] C. Balazs and C.P. Yuan, Soft gluon effects on lepton pairs at hadron colliders, Phys.Rev.D56:5558-5583,1997. [hep-ph/9704258]
- [50] Elisabetta Barberio and Zbigniew Was, PHOTOS: A Universal Monte Carlo for QED radiative corrections. Version 2.0 Comput. Phys. Commun 79,291 (1994)
- [51] S. Eno *et al.*, DØ Note **4097**, “Status of the Fast Simulatin PMCS, v01-96-00”
- [52] Junjie Zhu, Determination of Electron Energy Scale and Energy Resolution using P14 zee data, DØ note 4323, 2003
- [53] Jan Stark, Understanding and modelling the CAL energy resolution, DØ Wmass group meeting, Jan 13, 2006
- [54] B. Abbott *et al.* (DØ Collaboration), Phys. Rev. Lett. **80** (1998); B. Abbott *et al.* (DØ Collaboration), Phys. Rev. **D58** (1998); B. Abbott *et al.* (DØ Collaboration), Phys. Rev. Lett. **84** (2000); B. Abbott *et al.* (DØ Collaboration), Phys. Rev. **D62** (2000); V. Abazov *et al.* (DØ Collaboration), Phys. Rev. **D66** (2002).
- [55] John Gardner, Measurement of the W and Z Cross Sections in the Electron Channel and Extraction of the W Total Width from the Ratio, DØ thesis, Fall 2005

- [56] <http://www.thep.lu.se/torbjorn/Pythia.html>
- [57] S. Jadach, Z. Was and J.H. Kuehn, TAUOLA - A library of Monte Carlo programs to simulate decays of polarized τ leptons, *Comp. Phys. Commun.* 64 (1991) 275, (CERN-TH-5856 preprint)
- [58] V. Blobel, The RUN manual, Regularized Unfolding for High-Energy Physics Experiments, program manual, unpublished
- [59] <http://hep.pa.msu.edu/people/wkt/cteq6/cteq6pdf.html>
- [60] The RUN manual, Regularized Unfolding for High-Energy Physics Experiments, <http://www.desy.de/blobel/opalnote.ps>
- [61] Kirill Melnikov, Frank Petriello, Electroweak gauge boson production at hadron colliders through $O(\alpha_s^2)$, hep-ph/0609070